CORA Cork Open Research Archive
Cartlann Taighde Oscailte Chorcaí

Title	The potential role of optical guidance for bone-related biomedical applications in orthopedics and neurosurgery
Authors	Li, Li Yao
Publication date	2024
Original Citation	Li, L. Y. 2024. The potential role of optical guidance for bone-related biomedical applications in orthopedics and neurosurgery. PhD Thesis, University College Cork.
Type of publication	Doctoral thesis
Rights	© 2024, Li Yao Li. - https://creativecommons.org/licenses/by/4.0/
Download date	2026-11-06 12:10:23
Item downloaded from	https://hdl.handle.net/10468/17050



UCC
University College Cork, Ireland
Coláiste na hOllscoile Corcaigh

Ollscoil na hÉireann, Corcaigh

National University of Ireland, Cork



The potential role of optical guidance for bone-related biomedical applications in orthopedics and neurosurgery

Thesis presented by

Li Yao Li, MSc

0000-0001-6567-3140

for the degree of

Doctor of Philosophy in Engineering Science

University College Cork

Tyndall National Institute

Head of School: Dr. Fatima Gunning

Supervisor(s): Professor Stefan Andersson-Engels

Mr. Ray Burke

© Copyright by Li Yao Li 2024

Table of Contents

Table of Contents i
List of Figures v
List of Tables xi
List of Equations xiii
List of Abbreviations xiv
Declaration xviii
Acknowledgments xix
Publications and Presentations xx
Thesis Abstract xxi
Chapter 1 Introduction 1
1.1 Chapter Overview 1
1.2 Bone-related Surgery 2
1.3 Optical Techniques – Diffuse Reflectance Spectroscopy 5
1.4 Optical Techniques – Ultrafast Lasers 7
1.4.1 Subsection Overview 7
1.4.2 Context and Problem Statement 7
1.4.3 Background 8
1.4.4 Orthopedic Surgery – Ablation Parameters 10
1.4.5 Orthopedic Surgery – Thermal Effect 15
1.4.6 Orthopedic Surgery – Surface Morphology 16
1.4.7 Surface Modifications of Bone Implants 17
1.4.8 Discussion and Future Direction 19
1.4.9 Subsection Summary 24
1.5 Thesis Design and Scope 25

1.5.1 Motivation 25

1.5.2 Hypothesis 25

1.5.3 Aims and Objectives 26

1.5.4 Significance 26

1.6 Thesis Outline 27

Chapter 2 Extended-wavelength diffuse reflectance spectroscopy dataset for bone-related biomedical applications 29

2.1 Chapter Overview 29

2.2 Background and Summary 31

2.3 Methods 35

2.3.1 Specimen Preparation and Setup 35

2.3.2 Extended-wavelength Diffuse Reflectance Spectroscopy 36

2.3.3 Data Pre-processing 37

2.4 Data Records 39

2.5 Technical Validation 40

2.6 Code Availability 42

Chapter 3 Frameworks of wavelength Selection in diffuse reflectance spectroscopy for tissue differentiation in orthopedic surgery 43

3.1 Chapter Overview 43

3.2 Introduction 45

3.3 Materials and Methods 48

3.3.1 Specimen Preparation and DRS Data Acquisition 48

3.3.2 Data Preprocessing 50

3.3.3 Classification Models 50

3.3.4 Decision Tree Classifier – One Feature Classification 51

3.3.5 Feature Selection 51

3.3.5.3 Feature selection framework – backward interval partial least 56

3.4 Results 59

3.4.1 Classification Models 60
3.4.2 One Feature Classification Using Decision Tree 60
3.4.3 PCA, LDA, and biPLS Feature Selection Frameworks 61
3.4.4 Ensemble Framework of Feature Selection 63
3.5 Discussion 66
3.6 Conclusions 73
3.7 Code, Data, and Materials Availability 74
Chapter 4 Depth prediction in cranial bones using diffuse reflectance spectroscopy for craniotomy 75
4.1 Chapter Overview 75
4.2 Introduction 77
4.3 Materials and Methods 78
4.3.1 Experimental Setup 78
4.3.2 DRS Feature Selection 79
4.3.3 Monte Carlo simulation 79
4.3.4 Class Imbalance Correction 81
4.3.5 Classification 81
4.3.6 Lookahead Distance Prediction 81
4.4 Results and Discussion 82
4.5 Conclusions 88
Chapter 5 Future research and conclusions 90
5.1 Chapter Overview 90
5.2 Preliminary Study I: Concept design of a miniaturized optical probe for guidance of bone cement removal in orthopedic surgery 91
5.2.1 Background 91
5.2.2 Materials and Methods 92
5.2.3 Results and Discussion 95
5.2.4 Future studies and Conclusion 100

5.3 Preliminary Study II: PIRL-MS to differentiate bone and surrounding tissues... 101
5.3.1 Background 101
5.3.2 Materials and Methods 101
5.3.3 Results and Discussion 103
5.3.4 Future studies and Conclusion 107
5.4 Discussion and Conclusion of the Thesis 108
5.5 Personal and Professional Development – Reflection on the PhD Experience ... 108
References 112

List of Figures

Figure 1.2.1 Radiographs showing post-operative (a) total hip arthroplasty, (b) total knee arthroplasty where the white line indicates the joint line orientation angle and (c) spinal fusion. Images are adapted from references[10–12] under open access with the CC BY license.....3

Figure 1.3.1 Schematics showing a simple steady-state DRS setup with one broadband light source and one spectrometer to measure fat tissues. Adapted from this reference[33] under open access with the CC BY license. 6

Figure 1.4.1 Bone tissues after ultrafast laser ablation under SEM imaging in the visible regime showing (a) laser-induced thermal damages (spherical structures indicated by the white circle) at a higher PRR (515 nm, 1000 kHz, 4000 mm/s, 6.27 W), while (b) shows native bone structures such as Volkmann channels and lacunae at a lower PRR (515 nm, 250 kHz, 4000 mm/s, 6.27 W), as well as the Harversian channels shown in (c) after ablation in the IR regime (1030 nm, 250 kHz, 1000 mm/s, 6.27 W). Adapted from[89]. 16

Figure 1.4.2 Morphology of laser-drilled bone tissues under different environmental cooling conditions. Vertical panels (a–c) correspond to without cooling, gas cooling and water cooling; horizontal panels (subscript: none, 1, 2) correspond to white light, SEM and histology images. Adapted from[87].....17

Figure 1.4.3 SEM image comparison of a pre-anodized titanium-based bone screw without femtosecond laser treatment (left) showing osteoblast growth and adhesion, and the same screw with femtosecond laser treatment (middle) showing cell-free areas, and details at higher magnification (right). Adapted from[130].....19

Figure 2.2.1 EWDRS dataset collection and pre-processing workflow. (a) Modified from the publication[186]. Experimental setup included two commercialized spectrometers and a tungsten-halogen broadband light source. The source-detector separations were 0.63 mm from center to center. The locations of measurements followed a grid layout of approximately 5 mm apart for all specimens. (b) Data pre-processing consisted of background correction, reference calibration, spectral splicing using spline interpolation and median smoothing. 33

Figure 2.2.2 Example *ex vivo* specimens used for EWDRS dataset creation. (a) Ovine specimens included bone marrow, cartilage, cortical bone, trabecular bone (femur), dura, fat, muscle, grey and white matter (brain). Whole brain tissues were extracted from ovine cranial

cavities and sectioned along the coronal plane to expose grey and white matter. (b) Stepwise drilling was performed manually on porcine heads into the cranial cavity from the surface. The step size was pre-defined to be 1 mm but was uncontrolled during drilling due to manual handling. EWDRS measurements were taken at each stop. (c) Adapted from the publication[186]. Bone cement samples were cured and hand-molded into blocks. The black scale bars represent 1 cm. 34

Figure 2.3.1 The averaged EWDRS spectra for all labels in (a) Dataset 1 and (b) Dataset 2 showing the original spectra (left) and the SNV transformed spectra (right). SDs are shown by shaded error bands. Spectral range beyond 1850 nm was trimmed off. 38

Figure 3.3.1 *Ex vivo* ovine tissue samples including (a) muscle mass; (b) femur containing bone marrow, cartilage, cortical bone and trabecular bone; and (c) bone cement sample. The EWDRS system in (d) shows the experimental setup, where the fiber optic probe, connected to a broadband light source and two spectrometers, was in contact with one tissue specimen. White circle: fiber channel to light source; green circles: fiber channels to spectrometers; black circle: not in use. 49

Figure 3.3.2 Overview of a typical feature selection (FS) workflow. 52

Figure 3.3.3 FS framework implementing PCA/Sparse PCA to process the EWDRS dataset. Acronyms: FS for feature selection; PCA for principal component analysis; PC for principal component; EWDRS for extended-wavelength diffuse reflectance spectroscopy. 54

Figure 3.3.4 FS framework implementing LDA to process the EWDRS dataset. Acronyms: FS for feature selection; LDA for linear discriminant analysis; EWDRS for extended-wavelength diffuse reflectance spectroscopy. 55

Figure 3.3.5 biPLS FS framework showing the workflow to process EWDRS dataset. Acronyms: biPLS for backward interval partial least squares; FS for feature selection; EWDRS for extended-wavelength diffuse reflectance spectroscopy; PLS for partial least squares; PLS-VIP for PLS-Variable Importance in Prediction; RMSECV for root mean square error of cross-validation; clf for classification. 57

Figure 3.3.6 Ensemble feature selection (EFS) framework. Optional steps are labelled with asterisks, including training dataset partition, sequential removal of collinear features by

ranking and aggregation of results from all partitions. Acronyms: mRMR for Maximum Relevance – Minimum Redundancy; MI for Mutual Information; Boruta – RF for Boruta – Random Forest; SHAP for SHapley Additive exPlanations; clf for classification.....59

Figure 3.4.1 Balanced accuracy using one feature (wavelength) computed by decision tree classifiers plotted against wavelength features, for (a) bone cement vs. bone marrow, cartilage, cortical bone, trabecular bone, or the rest, respectively; (b) cortical bone vs. bone marrow, cartilage, muscle, trabecular bone, or the rest from top to bottom, respectively. Standard deviations are shown in shaded error bands. Acronyms: boneMarrow for bone marrow; cortBone for cortical bone; traBone for trabecular bone. 61

Fig. 3.4.2 The final 10 selected features from FS frameworks of PCA (top), LDA (middle) and biPLS (bottom) on the EWDRS spectra for *boneCement vs. rest* (left) and *cortBone vs. rest* (right). Standard deviations are shown in shaded error bands. The arrows highlight spectra of different class labels in subfigures for each scenario. Acronyms: boneCement for bone cement; boneMarrow for bone marrow; cortBone for cortical bone; traBone for trabecular bone; PCA for principal component analysis; LDA for linear discriminant analysis; biPLS for backward interval partial least squares.....62

Figure 3.4.3 Savitzky-Golay (SG) smoothed original extended-wavelength DRS (EWDRS) spectra overlaid with the final 10 selected wavelength features as (a, c) spectral band and (b, d) the top least collinear features for *boneCement vs. rest* and *cortBone vs. rest* in the VIS (top), VIS/NIR (middle), and VIS/NIR/SWIR (bottom) spectral ranges, respectively. Standard deviations are shown in shaded error bands. Acronyms: boneCement for bone cement; boneMarrow for bone marrow; cortBone for cortical bone; traBone for trabecular bone.....65

Figure 3.4.4 Balanced accuracy computed by LDA with CV plotted against sequential inclusion of the ranked least collinear wavelength features for *boneCement vs. rest* (top x-axis) and *cortBone vs. rest* (bottom x-axis) in the (a) VIS, (b) VIS/NIR and (c) VIS/NIR/SWIR ranges. The underscored features indicated the two wavelengths approaching the first plateau. Distribution of individual feature contributions on the prediction by SHAP analysis is shown for (d) *boneCement vs. rest* and (e) *cortBone vs. rest.* The 10 features were ranked on the vertical axis in descending order of their contributions to prediction. The horizontal axis illustrates the impact level of individual features of high or low value related to positive or

negative prediction. Acronyms: LDA for linear discriminant analysis; CV for cross-validation; SHAP for SHapley Additive exPlanations. 66

Figure 4.3.1 Experimental workflow. (a) Flowchart of data acquisition, pre-processing and analysis. DRS feature selection frameworks can be found in[200]. (b) Model summary for PLS regression and FNN. 82

Figure 4.4.1 The selected wavelength features for the OvR binary classification on the SNV-transformed DRS dataset between brain and cranial bone implementing (a) calculation of spectral difference showing features that satisfy user-defined criteria, with one additionally identified feature; and (b) feature selection frameworks based on PCA, LDA and ensemble approach. Number of pig heads = 5; number of drilled holes = 11; number of DRS measurements = 102. 83

Figure 4.4.2 Monte Carlo simulations of diffuse reflectance as a function of skull thickness (left) and fluence rate distribution (right) at (a) 450, 700, (b) 1200 and 1400 nm in the four-layered head model with separations shown at the bottom right. 84

Figure 4.4.3 PLS regression showing the predicted compared to the true thickness of the cranial bone ranging from 1 to 5 mm on the ROSE-SMOTE oversampled dataset with (a) all features and (b) selected features.....86

Figure 4.4.4 FNN showing the predicted compared to the true thickness of the cranial bone ranging from 1 to 5 mm on the ROSE-SMOTE oversampled dataset with (a) all features and (b) selected features. Validation loss is shown on the bottom panel. 86

Figure 5.2.1 The optical reamer system for bone cement removal during rTHA. (a) Schematic showing the concept design of the reamer and the optical sensing unit. The miniature camera module (blue square) is positioned in the center of 8 fiberoptic channels arranged equidistantly in a circle (Blue: camera module; green and magenta: DRS acquisition pairs; white: camera illumination (ILL)). (b) 3D printed mock-up reamer. (c) Probe footprint with illumination on. 93

Figure 5.2.2 Bovine femur specimen used in the rTHA simulation experiment showing (a) the original bovine femur cross-sectioned longitudinally, (b) bone cement injection into the

femoral column after removal of bone marrow, (c) cemented femoral canal and (b) inside of the bovine femur once the cement was cured. 95

Figure 5.2.3 Workflow of the rTHA simulation experiment consisting of three different methods generating corresponding data types. 95

Figure 5.2.4 Initial experiment to test the optical probe. (a) Images showing the original RGB channels from the miniature camera. (b) DRS spectral measurements of bone cement, bone marrow and cortical bone samples. Black arrows indicate the spectral features that could be used to differentiate different tissue types and bone cement. 96

Figure 5.2.5 Image features. (a) From left to right, the original image acquired of the bone cement sample using the miniature camera module, edge features detected by Prewitt filter in the horizontal direction and key feature points computed by Oriented FAST and Rotated BRIEF where the circle indicates the size of the important neighborhood, and the bar indicates the orientation of the key point. (b) Image decomposition by PCA using randomized SVD from left to right showing the red, green and blue channels. 97

Figure 5.2.6 RGB images acquired by the miniature camera module showing (a) bone-to-cement boundary, (b) distal cement plug, (c) blood drops on trabecular bone and (d) surface characteristics of bone cement. 98

Figure 5.2.7 Results obtained from the optical probe in the rTHA simulation experiment showing (a) broadband DRS from bone cement, bone marrow, cortical bone and inside of cortical bone for 355-1850 nm highlighting lipid absorption at 1200 nm and water absorption at 1450 nm, and (b) mean voltage signals from narrowband DRS at 1200 and 1450 nm for bone cement, bone marrow and cortical bone. 99

Figure 5.3.1 Schematics of the PIRL-MS collection setup and specimens included for the experiment.....102

Figure 5.3.2 Specimens post PIRL ablation showing (a) muscle, (b) cartilage, (c) cortical bone, (d) trabecular bone and (e) bone cement.....103

Figure 5.3.3 Preliminary mass spectra averaged over the number of measurements for bone cement, cartilage, cortical bone, muscle and trabecular bone. Signal intensities were normalized

by total ion current. Standard deviations were represented by the shaded error bands. Peak annotations were omitted for the sake of clarity. 104

Figure 5.3.4 PCA feature extraction for trabecular bone, cortical bone, cartilage, muscle and bone cement showing the first three PCs. 105

Figure 5.3.5 Confusion matrix for multi-class classification using LDA summed over 100 runs of CV for bone cement, cartilage, cortical bone, muscle and trabecular bone. 106

List of Tables

Table 1.4.1 The conventional lasers commonly used in bone-related procedures, with operation wavelengths and absorption chromophores[46,63,64].....9

Table 1.4.2 Summary of recent studies on the use of ultrafast lasers for orthopedic applications. 13

Table 1.4.3 Summary of ablation thresholds determined for different bone types. N = Number of pulses. 14

Table 2.3.1 Summary of the EWDRS measurements included in Dataset 1 (left) and Dataset 2 (right). 37

Table 3.3.1 The total number of tissue specimens and DRS measurements used in the analysis. 49

Table 3.4.1 Summary of the balanced accuracy scores on the holdout dataset generated by logistic regression (LogReg), linear discriminant analysis (LDA), random forest (RF), k-nearest neighbors (KNN), Gaussian Naïve Bayes (GNB) and support vector machine (SVM), and the average computation time to train one model. 60

Table 3.4.2 Summary of the balanced accuracy scores using the top 1 and 10 wavelength features generated from PCA, LDA, biPLS and EFS frameworks for *boneCement vs. rest* and *cortBone vs. rest*, the averaged computation time for one entire framework (top), and the scores generated by EFS framework on the holdout dataset in the VIS and VIS/NIR ranges (bottom). Accuracy using the top 1 wavelength was not applicable for Ensemble SB. Acronyms: PCA for principal component analysis; LDA for linear discriminant analysis; biPLS for backward interval partial least squares; SB for Spectral Band; LC for Least Collinear. 63

Table 4.3.1 Summary of optical parameters used in the 4-layered head model for MC simulations at 450, 700, 1200 and 1400 nm. 80

Table 4.4.1 OvR binary classification accuracy scores between brain and cranial bone using LDA, RF and KNN classifiers on the ROSE-SMOTE oversampled dataset with all and selected wavelength features. 85

Table 4.4.2 Summary of regression metrics from PLS and FNN for all features and selected features on the ROSE-SMOTE oversampled dataset. Values were rounded up to three decimal places.....87

Table 5.2.1 OvO binary classification among bone cement, bone marrow and cortical bone showing the classification model generating the highest accuracy score. 100

Table 5.2.2 OvR binary classification between bone cement and the rest class labels showing classification accuracy scores from the six models. 100

Table 5.3.1 Summary of the number of PIRL-MS measurements from bone cement, cartilage, cortical bone, muscle and trabecular bone. 103

Table 5.3.2 Classification report summarizing all metrics including precision, recall, F1 score, support, macro and weighted accuracy scores for multi-class classification using LDA for bone cement, cartilage, cortical bone, muscle and trabecular bone. Values are rounded up to two decimal places. 106

List of Equations

$\boldsymbol{Calibrated\ EWDRS\ spectrum} = \frac{\boldsymbol{S_{raw} - S_{bkgd}}}{\boldsymbol{S_{ref} - S_{bkgd}}}$, *(Equation 2.3.1)* 37

$\boldsymbol{SNV\ EWDRS\ spectrum} = \frac{\boldsymbol{(S_{cal} - \overline{S_{cal}})}}{\boldsymbol{SD(S_{cal})}}$, *(Equation 2.3.2)* 38

$\boldsymbol{balanced\ accuracy} = \frac{\boldsymbol{1}}{\boldsymbol{2}}\left(\frac{\boldsymbol{TP}}{\boldsymbol{TP+FN}} + \frac{\boldsymbol{TN}}{\boldsymbol{TN+FP}}\right)$, *(Equation 3.3.1)* 51

List of Abbreviations

biPLS	Backward interval partial least squares
CSF	Cerebrospinal fluid
CT	Computed tomography
CV	Cross validation
DL	Deep Learning
DRS	Diffuse reflectance spectroscopy
EFS	Ensemble feature selection
EWDRS	Extended-wavelength DRS
FNN	Feedforward neural networks
FS	Feature selection
fs	femtosecond
FWHM	Full width at half maximum
g	Anisotropic factor
GM	Grey matter
GNB	Gaussian Naïve Bayes
Hb	Hemoglobin
ILL	Illumination
IR	Infrared
KDD	Knowledge Discovery in Databases

KNN	K-nearest neighbors
LC	Least collinear
LED	Light-emitting diode
LDA	Linear discriminant analysis
LogReg	Logistic regression
MC	Monte Carlo
MCX	Monte Carlo eXtreme
MI	Mutual information
ML	Machine learning
mRMR	Maximum Relevance – Minimum Redundancy
$\boldsymbol{m/z}$	Mass-to-charge ratio
n	Refractive index
NA	Numerical aperture
NIR	Near infrared
OCT	Optical coherence tomography
OR	Operating room
OvO	One-vs-One
OvR	One-vs-Rest
PCA	Principal component analysis
PC	Principal component
PIRL-MS	Picosecond infrared laser mass spectrometry

PLS	Partial least squares
PLS-VIP	PLS-Variable Importance in Prediction
PRR	Pulse repetition rate
ps	Picosecond
pTHA	Primary total hip arthroplasty
$\boldsymbol{r^2}$	Coefficient of determination
RF	Random Forest
RMSE	Root mean squared error regression loss
RMSECV	Root mean square error of cross-validation
ROSE	Random Over-Sampling Examples
rTHA	Revision total hip arthroplasty
SA	Simulated annealing
SB	Spectral band
SD	Standard deviation
SEM	Scanning electron microscopy
SG	Savitzky-Golay
SHAP	SHapley Additive exPlanations
SMOTE	Synthetic Minority Over-sampling Technique
SNV	Standard normal variate
SVD	Singular value decomposition
SVM	Support vector machine

SWIR	Short-wave infrared
THA	Total hip arthroplasty
TJA	Total joint arthroplasty
TKA	Total knee arthroplasty
UVA	Ultraviolet A
VIS	Visible
WM	White matter
$\boldsymbol{\mu_a}$	Absorption coefficient
$\boldsymbol{\mu_s'}$	Reduced scattering coefficient
$\boldsymbol{\mu CT}$	X-ray computed microtomography

Declaration

This is to certify that the work I am submitting is my own and has not been submitted for another degree, either at University College Cork or elsewhere. All external references and sources are clearly acknowledged and identified within the contents. I have read and understood the regulations of University College Cork concerning plagiarism and intellectual property.

Signed:  Date: March 1, 2024

Li Yao (Celina) Li

Acknowledgments

I would like to express my sincere gratitude to my supervisor Professor Stefan Andersson-Engels and my co-supervisor Mr. Ray Burke for their continuous support, invaluable guidance, insightful feedback and encouragement throughout the entire course of my PhD journey. Their dedication, expertise and mentorship have been instrumental and precious in shaping and constructing this thesis.

I would like to extend my heartfelt appreciation to Science Foundation Ireland (SFI) for their generous financial assistance under Grant Numbers SFI/15/RP/2828, SFI/22/RP-2TF/10293. The funding has supported me through the past four years and enabled me to fully dedicate myself to completing this research with the necessary resources for conducting experiments, analyzing data and participating in scientific conferences.

I would also like to thank all my colleagues and peers at Biophotonics@Tyndall, IPIC, Tyndall National Institute, Cork, Ireland for their unconditional support, constructive discussions and collective enthusiasm for science. Special thanks to:

- Dr. Carl J. Fisher for continuous support and guidance with insightful inputs to experiments.
- Dr. Katarzyna Komolibus for stimulating discussions and assisting with experiments.
- Dr. Huihui Lu for scientific and mental support with constant encouragement.
- Dr. Konstantin Grygoryev, Dr. Simon Toft Sørensen and Dr. Walter Messina for engineering support and collaborations.

A very special thanks to:

- Dr. Andrea Visentin from Insight Centre for Data Analytics at UCC for all the guidance and mentorship. I would not be able to complete this thesis without his dedication.

I am deeply thankful to my family and friends for their unconditional love, encouragement and support, which has always been a constant source of strength to sustain me through the journey. Lastly, I would like to acknowledge all academic, technical support and administrative staff at Tyndall National Institute and University College Cork for their assistance. A big Thank You to everyone who has assisted me in any different capacities.

Publications and Presentations

Peer-reviewed Publications

1. **Li CL**, Fisher CJ, Komolibus K, et al. Extended-wavelength diffuse reflectance spectroscopy dataset of animal tissues for bone-related biomedical applications. *Sci Data*. 2024;11(1):136. DOI: https://doi.org/10.1038/s41597-024-02972-3.

2. **Li CL**, Fisher CJ, Komolibus K, et al. Frameworks of wavelength selection in diffuse reflectance spectroscopy for tissue differentiation in orthopedic surgery. *J Biomed Opt*. 2023;28(12). DOI: https://doi.org/10.1117/1.JBO.28.12.121207.

3. **Li CL**, Fisher CJ, Burke R, Andersson-Engels S. Orthopedics-Related Applications of Ultrafast Laser and Its Recent Advances. *Applied Sciences*. 2022;12(8):3957. DOI: https://doi.org/10.3390/app12083957.

4. (In progress) **Li CL**, Fisher CJ, Komolibus K, et al. Depth prediction in cranial bones using diffuse reflectance spectroscopy for craniotomy. *Biomed Opt Express*. 2024.

Conference Presentations

- (Oral Presentation) Li CL, Fisher CJ, Komolibus K, et al. Design and concept of a miniaturized optical probe for guidance of bone cement removal in orthopedic surgery. *European Conferences on Biomedical Optics.* 29 June 2023.

- Li CL, Fisher CJ, Komolibus K, Grygoryev K, Burke R, Andersson-Engels S. Wavelength selection using diffuse reflectance spectra and machine learning algorithms for tissue differentiation in orthopedic surgery. In: *Biophotonics Congress: Biomedical Optics 2022 (Translational, Microscopy, OCT, OTS, BRAIN)*; 2022:TS4B.6. DOI: https://doi.org/10.1364/translational.2022.ts4b.6.

- (Oral Presentation) Celina L. Li et al., “Wavelength selection using diffuse reflectance spectra in machine learning for tissue differentiation in orthopaedic surgery” *Photonics Ireland Conference* (15 June 2021).

Thesis Abstract

Optical sensing technology was explored as a means of intraoperative guidance for bone-related procedures in orthopedics and neurosurgery. Specifically, the feasibility of diffuse reflectance spectroscopy (DRS), a non-invasive and real-time optical technique that measures diffusely reflected light off samples of interest, was investigated in the thesis to differentiate biological tissue types and inform tissue boundaries as an intraoperative safety measure for revision total hip arthroplasty. Feature selection (FS) frameworks based on DRS measurements were developed utilizing machine learning techniques to determine wavelength features of optimal discriminative power for bone-related surgical procedures. Four FS frameworks, incorporating principal component analysis (PCA), linear discriminant analysis (LDA), backward interval partial least squares and an ensemble approach (biPLS), were designed with high adaptability to facilitate modifications and applications to other clinical scenarios. A feature subset of 10 wavelengths was generated from each FS framework yielding promising balanced accuracy scores for the one-vs-rest binary classification task. For cortical bone versus the rest class labels, PCA, LDA, biPLS and ensemble -based FS framework computed balanced accuracy scores of 94.8 ± 3.47%, 98.2 ± 2.02%, 95.8 ± 3.04% and 95.8 ± 3.16, respectively. For bone cement versus the rest, 100% balanced accuracy scores were generated from all FS frameworks. Subsequently, an in-house designed optical probe integrating DRS sensing was engineered and examined in *ex vivo* experiments. The most discriminative DRS wavelengths, selected by the FS frameworks including 1200 and 1450 nm, were incorporated as the illumination light sources. Furthermore, the performance of DRS to predict drilling depths in cranial bones was evaluated for craniotomy. Two models including partial least squares (PLS) regression and feedforward neural networks (FNN) were examined for prediction of skull thickness ranging from 1 to 5 mm away from the brain, yielding a root mean squared error regression loss of 0.08 and 0.06 mm from PLS, and 0.2 and 0.1 mm from FNN by using all

versus selected features as model inputs, respectively. The predicted depths served as a safety protocol to indicate lookahead distances. On the other hand, the potential of ultrafast lasers in bone-related surgical applications was reviewed and explored from multiple perspectives. The advantages offered by ultrafast lasers over conventional laser systems (continuous wave or long-pulse lasers) included superior precision and minimized collateral thermal damage to surrounding tissues. However, clinical translation of ultrafast lasers to surgical applications had been constrained by limitations in pulse average power and material removal rate. In contrast, the use in implant surface texturing had advanced substantially, effectively enhancing bioactivation and osteointegration within bone matrices. At the end, ambient mass spectrometry, which employed a picosecond laser system for plume generation, was additionally assessed for tissue differentiation in a preliminary study. The classification model employed PCA for dimensionality reduction and LDA for multi-class classification. By using the reduced mass spectra dataset, bone cement was distinguished from biological tissue types with 100% in different classification metrics (precision, recall, F1 score). The highest misclassification rate occurred between trabecular and cortical bone with 18 instances where trabecular bone was classified as cortical bone. Overall, the research presented in the thesis has demonstrated promising results to advance basic science and consequently set the foundation for translational study of integrating optical sensing into surgical tools in bone-related procedures with valuable insights. *This work was supported by Science Foundation Ireland (SFI), Grant No. SFI/15/RP/2828 and Grant No. SFI/22/RP-2TF/10293.*

Chapter 1
Introduction

1.1 Chapter Overview

This chapter provides a brief literature review focusing primarily on the recent research advances to inform the context of the thesis research. It begins with describing the background information on bone-related surgery in orthopedics and neurosurgery with relevant clinical challenges. Clinical needs to which optical sensing can offer advantages are highlighted. Following this, a concise introduction of the optical techniques discussed in the subsequent chapters is provided, which include diffuse optical tomography and ultrafast lasers. Potential applications of these two optical methods in bone-related surgery are reviewed. The thesis design and scope are described thereafter, explaining the research motivation, hypothesis, objectives and significance. Thesis outline is presented at the end, illustrating the key points covered in each chapter.

1.2 Bone-related Surgery

Bone-related surgery including orthopedic and neurosurgical specialties constitutes one of the most frequently performed surgical procedures in developed countries predominantly due to the aging population[1]. In orthopedics, several common procedures to treat conditions of degenerative nature are total joint arthroplasty (TJA), spinal fusion, total or partial shoulder arthroplasty, lumbar decompression and kyphoplasty or vertebroplasty, where TJA and spinal fusion are the top costly surgeries in the United States (US)[2]. Specifically, TJA includes mainly total arthroplasty of the knee (TKA) and the hip (THA), of which both have been regarded as highly successful procedures used to restore join function, relieve joint pain and thus improve quality of life for patients in the late stage of degenerative osteoarthritis[3,4] (Fig. 1.2.1a,b). The most common surgical approaches for primary TKA and THA are the standard medial parapatellar arthrotomy and posterior dissection, respectively. TJA complications involve periprosthetic fracture, aseptic loosening and infection, leading to inferior surgical outcomes and patient dissatisfaction. Spinal fusion, a surgery that fuses one or more vertebrae in the spine, is performed the most commonly for lumbar degenerative disc disease and cervical disc replacement in the US, consisting of 13.8% and 12.2% in 2008[5] (Fig. 1.2.1c). Surgical approach direction can be posterior, anterior or lateral of the spine. Innovative trends in surgical methods, implants and grafting materials have been developed to widen the range of indications for spinal fusion. Furthermore, neurosurgery is the surgical specialty concerned with disorders of the nervous system, which encompasses the brain, sometimes the spinal cord depending on the individual definition, and the peripheral nervous system. One of the neurosurgical procedures involving bone-related operation is brain surgery, where craniotomy is routinely required to temporarily remove part of the cranium and expose the brain for intracranial access[6]. Some typical indications and diagnoses that can be treated via craniotomy include brain tumors, vascular malformations, subdural and intracranial hematomas. During the procedure, burr holes are created by a surgical cranial drill to remove bone flaps off the skull. Some subtypes of craniotomy include trephine, flap, keyhole and stereotactic craniotomy; some typical flaps include bicoronal, frontal, temporal and pterional flaps[7,8]. Complications directly related to craniotomy involve cranial perforator plunging into the brain causing cerebral contusion, lacerations and injuries of the dura mater, dural venous sinus and cortical draining veins[9].



Figure 1.2.1 Radiographs showing post-operative (a) total hip arthroplasty, (b) total knee arthroplasty where the white line indicates the joint line orientation angle and (c) spinal fusion. Images are adapted from references[10–12] under open access with the CC BY license.

To improve post-operative outcomes, minimally invasive and percutaneous surgical techniques have been developed for most orthopedic procedures such as in the spine and the hip to improve patient recovery as well as to accelerate hospital discharge[13,14]. For instance, the direct anterior approach was implemented as a minimally invasive method in THA, leading to higher quality of life in the post-operative setting with reduced pain and improved hip function for patients[15,16]. In addition, outpatient shoulder arthroplasty strategy has demonstrated faster hospital release and safety with a cost reduction of 40% and higher patient satisfaction[17]. Along with these lines, adjunctive imaging techniques are usually essential in minimally invasive orthopedic surgeries to assist with pre-operative planning and intraoperative guidance. Such imaging modalities including intraoperative computed tomography (CT)[18], endoscopy[19], fluoroscopy[20], ultrasound[21], navigation[22] and robotics[23] are employed with the aim to provide spatial information of the surgical tool in a 2D or 3D space so that accidental breaching or plunging into critical tissues can be largely prevented. To illustrate, intraoperative ultrasound has been utilized via keyhole laparoscopy in lumbar decompression to repair pathologies around disc and bone that are causing neurological compression[24]. Augmented reality technology combined with real-time navigation guidance using intraoperative CT has also demonstrated utility in pedicle screw placement with improved accuracy rates as compared to

the freehand method, especially in the evaluation of critical spatial orientations[25]. Total navigation using portable intraoperative CT with integrated 3D navigation technology has shown promising results in spine surgery for safer, more accurate and more efficient workflows with negligible to minimal radiation exposure[26]. For primary uncemented THA, computer-assisted navigation with pelvic registration has yielded more accurate component alignments, thus reducing operating time by approximately 23%[27].

There are various unmet clinical needs relating to surgical guidance in the field of orthopedics and neurosurgeries, which can be broadly summarized as needing more accurate volumetric localization information of surgical tools with real-time feedback of boundary conditions in the intraoperative setting to prevent accidental damage of critical tissues in proximity. Optical techniques, especially spectroscopy and imaging, can possibly offer benefits based on the light-tissue interaction to reveal decisive information, therefore refining the workflow of bone-related surgeries. Although there has been considerable research effort devoted to the advancement of the field, the potential of optical sensing remains to be fully investigated. For example, some surgical use-cases can be identified in THA, where an optical sensor could be embedded in the tip of the surgical drill bit to inform tissue boundaries; clavicle fracture fixation, where optical detection could serve as a safety measure to terminate drilling prior to breaching; lumbar decompression, where optical sensing can provide discriminative information of encountered tissues including bone, dura and cerebrospinal fluid to prevent dural lacerations. Optical techniques that could offer potential for integration with existing surgical tools include diffuse reflectance spectroscopy, optical coherence tomography (OCT), fluorescence or autofluorescence spectroscopy and Raman spectroscopy, since these techniques are sensitive to changes in tissue compositions. Ultrafast lasers could also provide benefits in both sensing and surgical ablation simultaneously. Multi-modal platforms combining optical methods with artificial intelligence enhanced navigation, robotics and intraoperative imaging techniques has the opportunity to transform the current surgical paradigms and approaches enabling safer and more efficient procedures for both surgeons and patients. Engineering challenges exist in miniaturizing the optical sensing unit so that it can function properly in a noisy environment filled with blood, fluids and bone dust created by the high-speed drill.

The subsequent section of the introduction chapter focuses on the description of two optical techniques, namely diffuse reflectance spectroscopy and ultrafast laser. Diffuse reflectance

spectroscopy was the main technique investigated in this thesis, while ultrafast laser was reviewed in the field of orthopedics and explored in preliminary studies.

This section is partially based on the perspective paper[28]:

Fisher C, Harty J, Yee A, Li CL, Komolibus K, Grygoryev K, Lu H, Burke R, Wilson BC, et al. Perspective on the integration of optical sensing into orthopedic surgical devices. *J Biomed Opt*. 2022;27(01):010601. DOI: https://doi.org/10.1117/1.JBO.27.1.010601.

1.3 Optical Techniques – Diffuse Reflectance Spectroscopy

In this section, the fundamentals of diffuse reflectance spectroscopy (DRS) are briefly outlined, accompanied by descriptions of recent studies, as this optical technique has been extensively researched and reviewed in literature. DRS is an optical analytical technique that quantitatively measures diffusely backscattered light of the incident light by the sample of interest over a range of wavelengths after multiple scattering and absorption events[29,30]. This technique has been well researched in many studies of the medical fields ranging from cancer diagnostics to quantification of molecular constituents, because DRS can provide a non-invasive, convenient and cost-effective way to characterize various types of bulk samples based on the optical properties including absorption and (reduced) scattering coefficients. In the medical field, the resulted DRS spectral measurements consist of signal intensities of diffusely reflected light as a function of wavelengths, which contains information on tissue morphology and physiology. More detailed descriptions of tissue optics explaining light-tissue interactions can be found in the references[31,32].

DRS measurements can be acquired by steady-state, time-domain and frequency-domain setups. Fig. 1.3.1 shows a simple schematic diagram illustrating a DRS instrument used to collect steady-state DRS spectra of fat tissues[33], where one broadband light source was employed as the illumination for direct measurements of light reflectance as a function of wavelengths. In the time-domain (time-of-flight) method, the flight time needed for the photons from a short light pulse to propagate to the detector is firstly estimated using modelling such as Monte Carlo simulation or time-dependent diffusion theory and then fitted to experimental measurements[34], which also encodes depth information from the time-resolved nature. In the spatial frequency domain, tissue optical properties could be extracted from the amplitude

changes and phase shifts of the photon density wave created by sinusoidally modulated light at different frequencies[35,36].

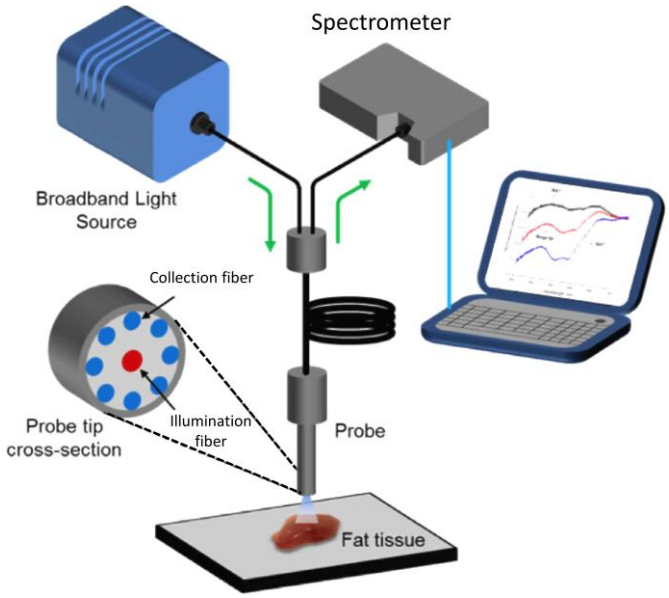


Figure 1.3.1 Schematics showing a simple steady-state DRS setup with one broadband light source and one spectrometer to measure fat tissues. Adapted from this reference[33] under open access with the CC BY license.

In the pre-clinical and clinical settings, DRS measurements can reflect structural changes at the cellular and molecular levels in diseased tissues and thus offer valuable information for diagnostics purposes. For instance, DRS has been widely investigated in cancer detection. In recent studies, S. Nazarian et al. examined the use of a hand-held DRS probe to differentiate *ex vivo* healthy and tumorous tissue specimens for colorectal cancer with the aid of a convolutional neural network, and were able to achieve high diagnostic accuracy with real-time tracking and visual feedback display[37]. A similar *ex vivo* study was conducted by F. Geldof et al. to evaluate the performance of DRS in soft tissue sarcoma with the aim of margin detection, which demonstrated a classification accuracy of 93%, sensitivity of 94% and specificity of 93% enabling real-time guidance in the clinic[38]. DRS was also combined with OCT and high-frequency ultrasound as a multi-modal platform by Y. Surkov et al. to successfully classify different clinical subtypes of basal cell carcinoma and benign neoplasms[39]. Furthermore, DRS has been used for assessment of tissue oxygenation in diabetic foot ulcers to determine the perfusion level and evaluate the healing process[40,41]. In liver diseases apart from cancer, the use of DRS to stage liver fibrosis and cirrhosis has been evaluated, demonstrating promising results in evaluating fat accumulation in the liver as a precursor[42].

Measurements of transcutaneous bilirubin concentrations could also be achieved with DRS, providing insights to detecting and managing liver conditions[43,44].

1.4 Optical Techniques – Ultrafast Lasers

1.4.1 Subsection Overview

This subsection is adapted from our previously published review paper, which reviews the current clinical usage as well as the technical advancements of ultrafast lasers in bone-related biomedical applications. As the use of ultrafast lasers has considerable potential in bone-related applications, the primary objective of the subsection is to offer comprehensive background information of the technology and thus establish the foundational context for the rest of the thesis.

The potential of ultrafast lasers (pico- to femtosecond) in orthopedics-related procedures has been studied extensively for clinical adoption. As compared to conventional laser systems with continuous wave or longer wave pulse, ultrafast lasers provide advantages such as higher precision and minimal collateral thermal damages. Translation to surgical applications in the clinic has been restrained by limitations of material removal rate and pulse average power, whereas the use in surface texturing of implants has become further developed to effectively improve bioactivation and osteointegration within bone matrices. With recent advances, we review the advantages and limitations of ultrafast lasers, specifically in orthopedic bone ablation as well as bone implant laser texturing, and consider the difficulties encountered within the scope of orthopedic surgical applications to which ultrafast lasers could provide a benefit. We conclude by proposing our perspectives on applications where ultrafast lasers could be advantageous, specifically due to the non-thermal nature of ablation and control of cutting.

This subsection is based on the review paper[45]:

Li CL, Fisher CJ, Burke R, Andersson-Engels S. Orthopedics-Related Applications of Ultrafast Laser and Its Recent Advances. *Applied Sciences*. 2022;12(8):3957. DOI: https://doi.org/10.3390/app12083957.

1.4.2 Context and Problem Statement

Lasers have been applied in many fields of medicine to treat diseases since invented. Today, there is a rapidly growing interest in the use of lasers in orthopedic procedures such as osteotomy[46–48],

oral[49–51] and spine[52,53] surgeries, as well as in cellular biology[54] and material micromachining[55]. Ultrafast laser, namely pulse widths of nominally a few picoseconds (ps) or shorter, has notably attracted considerable attention due to its unique property of optical nonlinearities. A wide range of applications has since been adapted in biophotonics such as multiphoton microscopy, cataract surgery and cell molecular manipulations[56]. In dentistry, the use of ultrafast lasers has proven promising for developing surgical procedures with higher precision and improved outcomes[57–60]. Even though a tremendous amount of research has gone into the field, a search of "ultrafast laser", "orthopedics" and "bone" yielded no review articles at the time of writing, specifically examining orthopedic applications using ultrafast lasers. We therefore surveyed the literature and considered the following questions: (1) With recent advances, is ultrafast laser technology matured enough for clinical dissemination for use in orthopedic surgeries and what are some still existing barriers? (2) What is the current status in orthopedic bone repair and implants? (3) What are some potential future studies and perspectives for ultrafast lasers in the field of orthopedics? The aim of this review is to provide an overview of recent advances in orthopedics-related applications using ultrafast lasers with the primary focus on bone ablation and implant processing, in an effort to critically evaluate new progress and provide some insights in the field. This paper begins with a brief background description of ultrafast lasers followed by recent studies in orthopedic surgery and bone implant processing, and lastly, perspectives on future directions.

1.4.3 Background

Laser ablation of bone tissue has gradually been introduced and accepted clinically as complementary techniques due to its higher precision and non-contact nature, though mechanical methods such as the use of drills, burrs, saws and milling cutters remain the gold standard for bone cutting procedures[61,62]. In particular, compared to laser ablation, mechanical instruments during bone cutting generate substantial thermal damage, bone fragmentation, amorphous formation and a mineral-rich carbon layer as well as biomechanical stress to adjacent structures; yet surgical protocols are well-established for these tools with acceptable clinical outcomes[46]. Among the many types of clinical laser systems, several common ones found within the field of orthopedics are Er:YAG, Nd:YAG, Argon and CO_2 lasers, which machine bone structures by the means of vaporization and melt expulsion[46,63,64] (Table 1.4.1). These conventional clinical laser systems, which have been developed often as continuous-wave or with longer wave pulse (in the μs and sub-μs range), depend primarily on the linear absorption of light by the target chromophore(s); thus, the penetration depth is significantly

affected by the absorption coefficient of water in an inverse relationship[46]. Due to the strong wavelength-dependent nature, non-deterministic ablation can be generated in highly heterogenous tissue structures leading to unnecessary injuries. Collateral damage surrounding the laser focal volume can also be induced by excessive heat release, thus greatly hampering bone healing and regeneration[46,61,62,65].

Table 1.4.1 The conventional lasers commonly used in bone-related procedures, with operation wavelengths and absorption chromophores[46,63,64].

Laser	Wavelength (nm)	Absorption Chromophore	Typical Laser Power (W)
Er:YAG	2940	Water	100–2250[66]
Nd:YAG	1064	Pigment, proteins	43–86[67]
Argon	514	Pigment, hemoglobin	1.5–3[68]
CO_2	10,600	Water	5–40[69]

The potential and efficiency of ultrafast pulsed laser (pulse ranging approximately from 100 fs to 10 ps) for ablating biological hard tissues have been extensively studied to overcome the thermal and thermo-mechanical drawbacks of the conventional laser systems. In particular, an ultrafast laser source is capable of producing extremely high peak radiation intensities ($>10^{11}$ W/cm^2), leading to the initial generation of free electrons through a multiphoton absorption mechanism and band-gap (Zener) tunnelling. A high density of excited electrons is therefore created locally in a small focal volume due to nonlinear absorption, triggering avalanche ionization that supports plasma formation. Ablation of tissue is then generated by the rapidly expanding high-density plasma, forming smoother cavity walls with negligible thermal damage. This process is known as plasma-mediated ablation or laser-induced breakdown. A free electron formed during the multiphoton absorption and avalanche ionization processes can be promoted from the ground state to the valence band by the energy of two, three, four, five and six photons for wavelengths longer than 191, 383, 574, 766 and 958 nm, respectively. Wavelength dependence of the process thus indicates decreased tissue damage threshold along with decreasing wavelength[70]. Thermal damage can remain highly confined in the focal volume during optical breakdown not only because the location of plasma formation can be controlled by precise energy deposition using focused laser radiation but also because ultrafast laser pulses are a few orders of magnitude shorter than thermal diffusion time (heat transfer ranging in the order of picoseconds to nanoseconds from absorbing proteins to tissue water)[71–73]. A standard

state-of-the-art ultrafast laser system normally uses a Ti:sapphire oscillator in the near-infrared region or infrared region (NIR/IR) for tissue ablation, where the pulse width and repetition rate can vary depending on the application. Interested readers can find more details on ultrafast laser interactions and mechanisms with biological hard tissues from literature reviews[65,74–79]. Advantages of using ultrafast laser over longer wave pulse laser have also been recognized, specifically including absence of melting, carbonization or microcracks; negligible collateral damage; selective ablation with increased precision; and the potential for delivering minimal invasive procedures[80]. The inherent limitations of ultrafast laser tissue ablation lie in the penetration depth and precision, primarily because of nonlinear self-focusing, plasma defocusing and normal group velocity dispersion phenomena, which can be mitigated by maximizing focusing numerical aperture (NA), employing pulse durations shorter than 10 ps and using repetition rates higher than the kHz regime[65,78].

1.4.4 Orthopedic Surgery – Ablation Parameters

Early research of ultrafast laser ablation of bone tissues was predominantly focused on modification and microsurgery of teeth, ear[81] and spine, with very few publications in orthopedic surgery of the peripheral extremities (long bones of arm and leg). Despite all the advantages, the main issue that limits its clinical translation and acceptance, namely the low ablation removal rate, has remained the same even to date[80,82–84]. For instance, two studies published in 2007 discussed the use of ultrafast laser for bone ablation. Wieger et al. conducted a comparison study of laser osteotomy on bovine bone tissues using a femtosecond (fs) Yb:glass laser (pulse duration = 330 fs; λ = 1040 nm; pulse repetition rate (PRR) = 1 kHz; max. average pulse energy = 130 μJ) and a conventional Er, Cr:YSGG laser system (pulse duration = 53 μs; λ = 2780 nm; PRR = 20 Hz; max. average pulse energy = 300 mJ)[80]. The ablation rate of the femtosecond laser (~4×10^{-4} mm^3/s) was found to be approximately 400-fold slower than the Erbium laser (~0.15 mm^3/s) given a power density of ~1000 W/cm^2, but could be further optimized by increasing the PRR while maintaining the favorable cut surface morphology. The ablation thresholds were calculated to be 0.82, 0.78 and 0.54 J/cm^2 for spongiosa bone, compacta bone and cartilage, respectively, with an average of 72.4 laser pulses overlapped. Moreover, an ultrafast laser system consisting of a diode-pumped Yb:glass laser seed source and a Yb:KYW thin disk laser head (pulse duration = 900 fs; λ = 1030 nm; PRR = 45 KHz; max. average pulse energy = 100 μJ) was used by Liu et al. to achieve a maximum ablation rate of 0.15 mm^3/s in porcine femora at the given power output, which was acceptable

clinically for knee arthroplasty[83]. Additionally, in precision surgery such as stapedotomy, ultrafast laser has also been proven ideal by offering minimal thermal and acoustic damage[81,85].

Encouragingly, in the past decade, several studies have discovered more novel practices using ultrafast lasers and attempted to tackle the obstacles in the clinic. Notably, Subramanian et al. have developed a lightweight, miniaturized surgical ultrafast laser probe that offers clinically acceptable ablation speed in orthopedic surgery, enabling the potential of robotic integration[86]. Another group also established an optical real-time monitoring of ultrafast laser bone drilling utilizing plasma emission spectroscopy, which allowed for differentiation between bone and bone marrow[87]. The feasibility of drilling large-sized, deep holes on cortical bones has also been demonstrated[87,88]. Furthermore, the fastest ablation rate on cortical bone tissues to date is 0.99 mm^3/s in the literature, which was performed on fresh *ex vivo* sheepshank bone under a cooling condition by Zhang et al. in 2020[87], followed by 0.66 mm^3/s on dried ex vivo defrost and dried porcine femurs under a non-cooling condition reported by Gemini et al. in 2021, using industrially available femtosecond laser sources[89], in comparison to mechanical tools that enable drilling and cutting speeds of up to 5 mm/s[28]. The upscaling of ablation rate is fundamentally constrained by the average powers combined with considerations of repetition rate optimization as well as thermal effect on the tissue[84,90]. The phenomenon arises from the fact that, at the given laser average power and wavelength, an increase in single pulse energy resulting from a decrease in PRR improves the ablation rate until the saturation point where laser energy begins to spread outside the penetration volume[91]. Gemini et al. also compared bone ablation efficiency in different wavelength regimes (IR—1030 nm, visible—515 nm, UV—343 nm), average powers (IR—6.27 W, visible—6.27 W, UV—3.9 W), PRRs (250, 500, 1000 kHz) and scanning speeds (1000, 2500, 400 mm/s) with the conclusion that visible regime, the lowest PRR and the highest scanning speed provided the best ablation rate without thermal tissue disturbance because bone chromophores responded differently to the three wavelength regimes[89]. Moreover, the ablation rate is sometimes affected by bone debris accumulation depending on the amount generated, and thus can be further upscaled by immediate debris removal after each pulse using a cooling system[87,92]. It was demonstrated that compressed air flow and water flow could reduce bone debris by 64% and 76%, respectively; however, significant laser energy loss was observed under water cooling conditions leading to the slowest ablation rate[87]. It has also been noted that sample conditions, specifically *ex vivo* vs. *in vivo*, dried vs. fresh and storage conditions, as well as bone surface processing such as sanding, polishing or unaltered can have a significant influence on the ablation performance[93–

[95]; thus, it is crucial to simulate a real clinical situation for accurate and consistent assessments. Table 1.4.2 summarizes the ablation rates from ultrafast laser bone ablation studies of different bone samples using different laser parameters.

Characterization of the ablation threshold and the incubation effect likewise plays a major part in optimizing ablation performance on a particular bone type. Ablation threshold, which represents the minimal laser fluence needed to initiate material removal from a surface[84,94], can be measured by exposing the surface to ultrafast laser pulses of decreasing energy or beam radius until no material removal occurs[84,96] or using the D^2-technique calculation based on the correlation between the diameters of ablated craters and different pulse energy levels[93,94,96–100]. Bone ablation is usually optimized when the pulse energy is sufficiently higher than the threshold to ensure pulse-to-pulse consistency, but not exceeding a limit that could induce collateral thermal damage[101]. The balance between ablation rate and fluence therefore needs to be well characterized for the bone tissue, otherwise negating the most unique advantage of minimizing thermal effects[102–104]. On the other hand, incubation effect refers to the phenomenon where a reducing ablation fluence threshold is accompanied by an increasing number of incident laser pulses in a power law relationship[105], and is typically caused by sufficient energy deposit from the few initial pulses for subsequent pulses permitting lower than single-pulse ablation threshold[86,94,100,106,107]. An incubation coefficient value of 1 indicates no incubation effect. Incubation effect is the most profound at lower pulse numbers where ablation threshold is rapidly reduced as the pulse numbers increase until a saturation point[94,108], and has been shown to modify tissue structures significantly enough, especially at higher PRR, to create beam distortion, shadowing and substantial light scattering due to debris shielding, thus leading to considerable thermal disturbance and decrease in ablation rate[89,103]. With that being said, a recent study by Ashforth et al. concluded that there was none to very little incubation effect found for two types of cortical bones (bovine and ovine) by showing the same incubation coefficient (1.02 ± 0.05)[93]. The possible reason, as the authors explained, could be due to the already high level of microscopic inhomogeneity of native bone tissues; the newly introduced structure defects from laser ablation were consequently negligible. For clinical translation, such behaviors are indeed beneficial in the way that the efficiency of ultrafast laser ablation can remain consistent while drilling into different bone structures. Table 1.4.3 outlines the ablation threshold for different tissue types using different laser parameters.

Table 1.4.2 Summary of recent studies on the use of ultrafast lasers for orthopedic applications.

Author/Year	Bone Type	Ablation Rate (mm^3/s)	Laser System Parameters	Potential Application
Subramanian et al., 2021[86]	Bovine rib (fresh)	$>1.7 \times 10^{-2}$	A CaF_2 objective; Er-doped fiber; 1552 nm, 600 fs, 303 kHz	A miniaturized surgical probe for robotic microsurgery such as spine
Gemini et al., 2021[89]	Porcine femurs (defrost and dried)	0.66	A Tangerine industrial femtosecond laser, Amplitude Laser; 517nm, 350 fs, 250 kHz	Clinical automated high-resolution orthopedic surgery
Ashforth et al., 2020[93]	Bovine and ovine cortical bone (fresh)	0.90 μm/pulse *	A Ti:Sapphire femtosecond pulsed laser; 800 nm, 140 fs, 1 kHz	Handheld or robotic high-precision orthopedic surgery procedures
Zhang et al., 2020[87]	Sheepshank bone (fresh)	0.99	A Yb:KGW femtosecond laser; 1030 nm, 230 fs, 200 kHz	Large-size hole drilling with real-time monitoring
Aljekhedab et al., 2019[92]	Bovine cortical bone (fresh)	0.60×10^{-3}	A Ti:Sapphire femtosecond laser; 800 nm, 210 fs, 1kHz	High-precision bone cutting surgery
Tulea et al., 2015[96]	Cow femur cortical bone (fresh, dried or fixed)	0.19	A Nd:YVO_4 picosecond laser; 532 nm, 25 ps, 20 kHz	Bone surgery
Plötz et al., 2014[90]	Porcine rib (fresh)	8.7×10^{-2}	A Nd:YVO_4 laser; 1064 nm, 8 ps, 500 kHz	Dental surgery
Su et al., 2014[109]	Bovine femoral condyle (fresh)	0.80×10^{-4}	A Ti:Sapphire femtosecond laser combined with an optical parametric amplifier; 1700 nm, pulse duration N.R., 5 kHz	Microfracture surgery for articular cartilage injury in the knee

* Reported as depth removal per pulse.

Table 1.4.3 Summary of ablation thresholds determined for different bone types. N = Number of pulses.

Author/Year	Bone Type	Ablation Threshold (J/cm^2)	Pulse Duration (fs)	Wavelength (nm)
Subramanian et al., 2021[86]	Bovine cortical bone (fresh; unaltered)	1.38 ± 0.18 (N = 25.83 *; multi-pulse threshold)	600	1552
Ashforth et al., 2020[93]	Bovine and ovine cortical bone (fresh; unaltered)	0.92 (bovine) 0.97 (ovine) (N = 1000)	140	800
Plötz et al., 2014[90]	Porcine cortical bone (fresh; unaltered)	1.5 (N = Not Reported)	8×10^3	1064
Cangueiro et al., 2012[100]	Bovine cortical bone (fresh; polished)	0.32 ± 0.04 (N = 100)	500	1030
Nicolodelli et al., 2012[103]	Bovine cortical bone (fresh; polished)	0.23 (N = 1000)	70	801
Emigh et al., 2012[94]	Porcine cortical bone (fresh; unaltered)	1.75 ± 0.55 (N = 1000)	170	800
Lim et al., 2009[106]	Bovine cortical bone (fresh; polished)	1.22 ± 0.29 (strong) 0.79 ± 0.18 (gentle) (N = 1000)	150	775
Girard et al., 2007[84]	Porcine cortical bone (fresh; polished)	0.69 ± 0.08 (N = 1000)	200	775

* Estimated averaged N value predicted by simulation.

1.4.5 Orthopedic Surgery – Thermal Effect

As discussed before, ultrafast laser ablation is overall characterized by minimal thermal damage and limited heat diffusion outside of the focal volume, because the dominant mechanism, namely multiphoton absorption of light and avalanche ionization or hydrodynamic plasma expansion[110], is not thermally mediated with only little heat deposition, making it an auspicious technique in the clinic[65,111–113]. Still early studies demonstrated some carbonization, cracking and melting[100,103,109], which could be mitigated by employing cooling systems[87,114]. Nevertheless, recent studies have shown more optimized performance[79,115,116]. In particular, Ashforth et al. reported no observations of a heat-affected zone at the maximum laser fluence and pulse numbers by assessing any forms of carbonization, discoloration and microcracking around the craters using light microscopy[93]. Canteli et al. evaluated thermal effects on fresh bovine femur using a nanosecond laser source (20 ns, 355 nm, 2–100 kHz) as compared to a picosecond laser source (12 ps, 1064 nm, 100–600 kHz), and found that the picosecond laser, although not as ideal as femtosecond lasers, resulted in significantly reduced heating compared to the nanosecond laser[115]. The study by Gemini et al. provided optimization strategies and described the observation of increasing thermal accumulation while decreasing scanning speed and increasing PRR individually in the IR and visible wavelength regimes[89]. When both the scanning speed and PRR were increased, not only thermal loads increased but expanding plasma plume was also produced, leading to reduced ablation efficiency and precision. However, the observation did not apply to the UV regime, where collagen and hemoglobin are the main absorbers. No specific behavior was detected with changing parameters; the thermal load was comparatively high enough at the lowest PRR to generate laser-induced bone calcination. In Fig. 1.4.1, laser-irradiated damages such as the typical thermal-induced particle-like roughness and micro-cracks can be seen under SEM images at a higher PRR (Fig. 1.4.1a), whereas native bone structures containing blood vessels and osteocytes were preserved at a lower PRR (Fig. 1.4.1b,c)[89]. The interrelationship between scanning speed, PRR and wavelength choice therefore requires thorough investigation for an optimized laser ablation performance without collateral thermal damage on bone tissues. Similarly, Gill et al. studied temperature distributions of dried bovine bone irradiated also by a Tangerine laser (Amplitude, 320 fs, 1030 nm) using different PRRs[116]. It was found that carbonization occurred at high enough PRRs where thermal dissipation was exceeded by accumulation causing irreversible tissue damage, and therefore the importance of rigorous laser parameter selection was again emphasized in order to minimize thermal effects while maximizing ablation rates. Furthermore,

the pattern of scanning path can also influence heat accumulation and thus reduce the ablation rate. Circular scanning motion was found to generate significant thermal damage (charring) as compared to scanning in line paths because of poor heat dissipation[87]. Additionally, with large-size and deep holes, ultrafast laser can still produce slight charring around the edge.

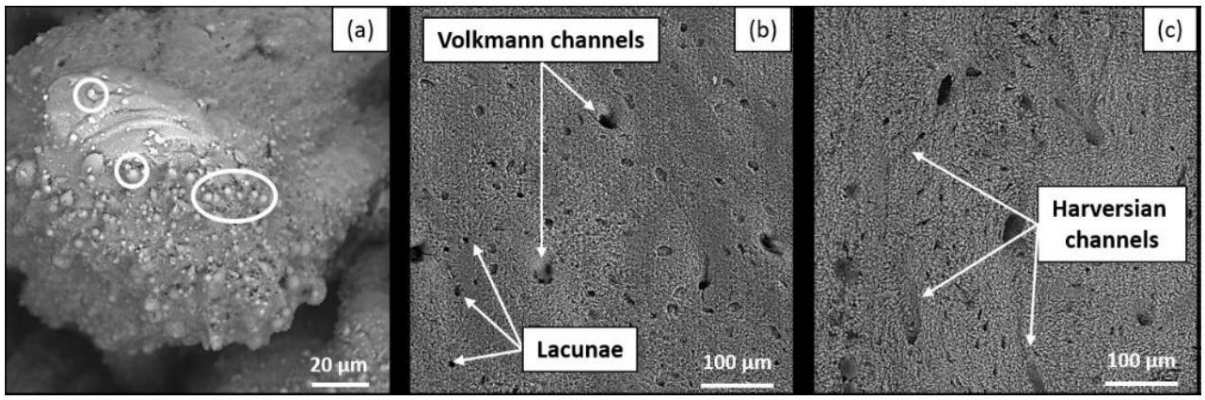


Figure 1.4.1 Bone tissues after ultrafast laser ablation under SEM imaging in the visible regime showing (a) laser-induced thermal damages (spherical structures indicated by the white circle) at a higher PRR (515 nm, 1000 kHz, 4000 mm/s, 6.27 W), while (b) shows native bone structures such as Volkmann channels and lacunae at a lower PRR (515 nm, 250 kHz, 4000 mm/s, 6.27 W), as well as the Harversian channels shown in (c) after ablation in the IR regime (1030 nm, 250 kHz, 1000 mm/s, 6.27 W). Adapted from[89].

1.4.6 Orthopedic Surgery – Surface Morphology

Surface morphology is usually assessed using scanning electron microscopy (SEM), confocal microscopy, X-ray computed microtomography (µCT) and histology to evaluate thermal effects on the tissue[87–89]. By visually examining the condition of craters or holes on bone tissue after laser ablation on the microscopic level, physical features such as charring, roughness and micro-cracks can be identified to determine and compare the degree of laser-induced damage. As previously mentioned, a picosecond or femtosecond pulsed laser system generates little to no thermal effect during bone ablation as compared to longer pulse or mechanical tools[102]. Several authors have described, under SEM or histological observations, that the bottom and side walls of the laser-ablated cavity are smooth and homogeneous with a well-defined geometry[85,92,93,115]. No significant signs of charring, melting or major debris accumulation were found[100,102,106]. Fig. 1.4.2, adapted from[87], shows an image comparison of ultrafast laser ablation under different cooling conditions, namely no cooling (a, a_1, a_2), gas (b, b_1, b_2) or water (c, c_1, c_2) cooling, using white light imaging, SEM and histology, respectively, which

demonstrated great uniformity and precise cutting with, overall, no observation of cracks, especially for cooling-assisted drillings. Some microcracks were, however, observed in the inner wall without cooling, which could potentially delay bone healing[87].

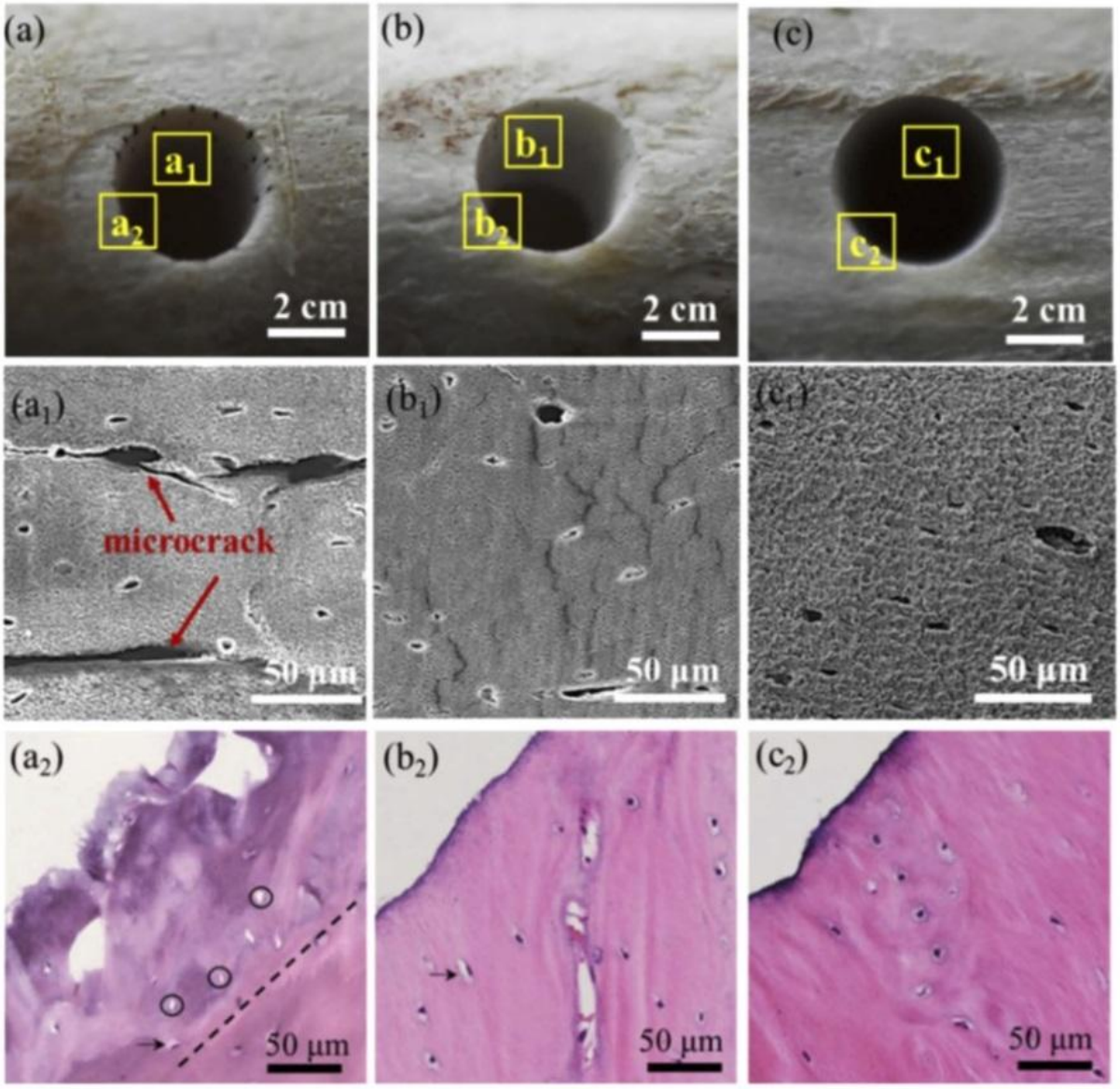


Figure 1.4.2 Morphology of laser-drilled bone tissues under different environmental cooling conditions. Vertical panels (a–c) correspond to without cooling, gas cooling and water cooling; horizontal panels (subscript: none, 1, 2) correspond to white light, SEM and histology images. Adapted from[87].

1.4.7 Surface Modifications of Bone Implants

Another vastly studied area is surface modification of bone implants by ultrafast laser for improved osteogenesis and osteointegration. The major clinical issue present today, despite

well-established implant techniques, is implant loosening owing to inadequate integration, fibrogenesis and infection[117]. Surface modification thus plays an important role in enhancing cell–material interactions, and various properties can be manipulated via ultrafast laser irradiation such as surface topography, roughness and wettability[75,118]. Different nanostructures of identical materials can initiate different cellular responses and behaviors including cellular adhesion, motility, orientation and signaling pathways[119]. These factors, in short, greatly affect the success of bone implant performance, which is essentially dependent on the outcome from the complex interaction between surface characteristics and biological response. The detailed description of bone–implant interface can be found in review articles[120,121]. In general, the goal of surface modification is to enhance the beneficial effects exerted on osteogenic differentiation and osteointegration of the implant[117,122]. Specifically, increasing hydrophilicity and roughness supports improved cell adhesion on an enlarged surface area as well as strong biomechanical anchorage of the implant[123,124]. Some commonly used techniques for surface roughening include grinding, polishing, sputtering and laser texturing[117]. Similar to orthopedic bone ablation, the use of ultrafast pulsed lasers (pico- or femtosecond) for surface modifications of bone implants has become attractive because of the relatively faster processing time, simpler technical requirements and minimal damage to adjacent surfaces[118,125,126]. In terms of the materials for biomedical implants, a particular attention has been paid to titanium and its alloys owing to their great biocompatibility, high resistance to temperature and corrosion as well as exceptional strength-to-weight ratio[127,128]; however, due to bio-inertness of titanium alloys, bioactivation of the material can sometimes be difficult to achieve[129]. Therefore, in this section, we briefly review recent studies on ultrafast laser surface texturing of titanium-based implants for orthopedic applications.

In recent years, femtosecond lasers have been explored extensively for surface modifications of bone implants. For example, Luo et al., investigated the ability of femtosecond lasers texturing to improve bioactivity of three types of titanium surfaces by assessing apatite deposition, a key indicator of enhanced biocompatibility and osteointegration, and found that femtosecond laser texturing could promote apatite precipitation and therefore better clinical outcomes[129]. Muck et al. examined, opposite to increasing cell adhesion, micro- and nanostructures fabricated by femtosecond laser processing to reduce cell adhesion[130]. The authors demonstrated that post-processing by electrochemical anodization following femtosecond laser treatment was able to significantly reduce cell adhesion to titanium-based flat plates and screws while promoting extracellular matrix production for osteoblasts. Fig.

1.4.3 shows the SEM images of differences in osteoblast attachment to the screw and the growth on the surface between femtosecond laser processing with and without anodization. The finding suggested that the technique with its reversal could be applied to bone fixture implants that needed to be removed from the body after a period of time, i.e., less integration with the bone matrix preferred, as well as the ones that remained in the body permanently, i.e., promoted matrix growth[130]. Similar studies assessing cell adhesion and migration also concluded that femtosecond laser processing was able to improve proliferation of human mesenchymal stem cells, thus promoting osteogenesis and osteointegration[131,132]. Moreover, Liu et al. successfully prepared titanium alloy surfaces that enhanced early stage osteointegration with anti-inflammatory properties using femtosecond laser processing and sandblasting[133], again demonstrating the beneficial effects that ultrafast laser treatment could deliver. On the other hand, ultrafast laser surface processing of other biomaterials such as polyether-ether-ketone[134,135] and ceramics[136–138] has also been studied to show a comparable synergistic effect that can encourage osteointegration and osteogenesis.

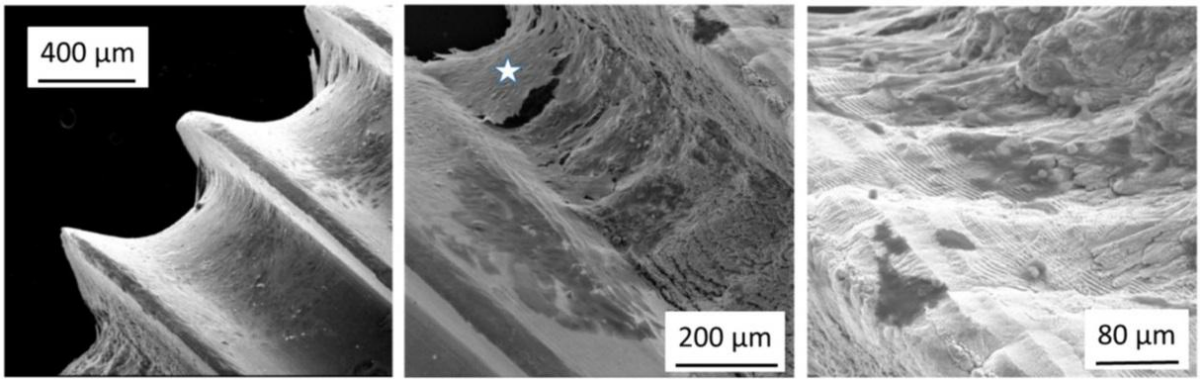


Figure 1.4.3 SEM image comparison of a pre-anodized titanium-based bone screw without femtosecond laser treatment (**left**) showing osteoblast growth and adhesion, and the same screw with femtosecond laser treatment (**middle**) showing cell-free areas, and details at higher magnification (**right**). Adapted from[130].

1.4.8 Discussion and Future Direction

As mentioned, the intrinsic properties of ultrafast lasers provide several benefits in applications involving bone or bony structures. In comparison to conventional CW and longer wave pulse lasers that primarily depend on linear absorption of light, the nonlinear nature of ultrafast laser interaction with biological hard tissues enables unique and promising applications in the field of orthopedic surgery. As such, because of the difference present in interaction mechanisms,

photodamage induced by ultrafast lasers is essentially wavelength-independent (i.e., optical properties of tissues play a minor role) with negligible thermal effects and finely controlled precision. In examining the benefits and potential use of ultrafast lasers during surgery, which can be categorized as pre-operative, intraoperative and post-operative advantages, there will be a focus on pre-operative and intraoperative strategies since post-operative utilizations, namely wound healing and tissue bonding, have been extensively reviewed elsewhere[65,139,140]. In addition to this, we will speak to the technical challenges encountered so far, which preclude ultrafast lasers from widespread clinical adoption. Finally, future research directions that are of potential interest clinically will be discussed.

In terms of pre-surgical applications of ultrafast lasers in orthopedic surgery, the main benefit would be the preparation of implants or materials for integration within bone. For instance, Liu et al.[133] and Muck et al.[130] have demonstrated how ultrafast laser machining increases osteointegration and biocompatibility. Taking these into consideration, it could be envisioned that implants in total hip arthroplasty and total knee arthroplasty would be patterned to increase osteointegration of the implants without necessitating the use of bone cement or other anchors, such as intramedullary nailing or percutaneous screws. Although an uncommon complication, early failure of implants occurs in both knee and hip arthroplasty, either due to failure of bone cement to anchor the implant causing loosening and loss of stability, or contact with surrounding bone when using a cementless implant, leading to a similar outcome[141,142]. Revision surgeries in these cases provide worse outcomes compared to the primary surgery, with higher rates of infection, worse overall prognosis and delayed healing, especially in patients with preexisting comorbidities and poor overall health[143]. Thus, ultrafast laser machining of the implant surface could mitigate failure rates and improve overall outcomes. However, it should be noted that during many of these surgeries, it is not known a priori what implant or which size the surgeon will choose as it is dependent on the size of bored hole in the femur/tibia or the size of the acetabulum.

In these cases of furthering the osteointegrative potential of hip and knee arthroplasty implants, there are two approaches in which femtosecond laser surface modification could be used. In the first use case, all implants have surface preparation performed with ultrafast lasers at the time of manufacturing prior to shipment to various orthopedic centers. If the cost or time of surface preparation is not a feasible option, a second approach would be for the surgeon to identify high-risk patients where implant failure may occur and prepare these devices

accordingly. Furthermore, many medical device manufacturers have explored the use of 3D printing of custom implants based on preoperative imaging where ultrafast laser surface modification in combination with custom 3D-printed joint implants could provide an overall increase in mobility and function following surgery for these high-risk patients. Thus, ultrafast laser surface preparation in conjunction with custom implant manufacturing, where an increase in osteointegration contributes to the overall well-being of the patient, provides a greater impetus for both custom implant manufacturing as well as increases in overall outcome. Future work would examine the use of ultrafast laser patterning on materials outside of the traditional knee arthroplasty and hip arthroplasty components, as 3D-printed joint replacement can use highly porous materials that are prone to heat damage and warping[144]. Additionally, recent studies have demonstrated higher migration rates (implant slides 'upwards' from where it was set) for cementless 3D-printed joint 'stems' in knee and hip arthroplasty[145]. This migration of the implant away from where it is set is an indicator of impending aseptic loosening, which normally necessitates a revision procedure, whereby surface preparation and increased implant anchoring provides a tangible benefit to both patients and operators, since, as discussed, revision surgery is a costly and detrimental procedure.

Secondly, to preparation of implants or materials, a large area of research for the use of ultrafast lasers is cutting of hard surfaces, specifically dentine, enamel and bone. Specifically, it was noted in early studies on dentine ablation that ultrafast laser cutting provided limited thermal deposition with increased cellular survival surrounding the ablation area. This contrasts with the use of electrocautery (EC) or burrs/saws/trephines, where frictional forces during cutting cause a large amount of heat deposition to the surrounding tissues outside of bone, leading to potential cell damage with complications such as nerve damage, bleeding from injured vessels and delayed healing of the cutting surface. In these cases, the non-thermal nature of ultrafast lasers provides an opportunity for use in procedures that are performed adjacent to sensitive tissues. These procedures need a safety margin to protect sensitive tissues; for example, transsphenoidal resection or laminectomy, involving cutting and removal of bone close to the central nervous system, specifically the pituitary gland, cerebrospinal fluid (CSF) and dura in transsphenoidal resection and the CSF/dura and the spine in laminectomy, or close to vessels, such as in brain surgery in the posterior cranial fossa, where venous sinuses and arteries are located. Utilizing ultrafast laser cutting in lieu of mechanical drills in transsphenoidal resection or laminectomy, therefore, would be of benefit in reducing or eliminating thermal deposition in surrounding tissues compared to a high-speed mechanical burr or trephine alone, providing

a greater safety margin in the procedures where critical tissues are nearby. Furthermore, this could be generalized to many approaches in the skull, whereby CNS/dura is invariably adjacent; for example, thermal injury has been demonstrated in retrosigmoid intradural suprameatal approach, with cutting through bone leading to injury of the petrosal sinuses and nerve with possible cerebellar swelling and infarction[146]. Thus, with limited heat generation, ultrafast laser ablation could be adopted for procedures whereby limiting adjacent thermal damage should reduce any unintended consequences from already complex surgeries to begin with.

Despite the readily apparent advantages with ultrafast lasers, there has been limited adoption to date, even in applications where the benefits are obvious. The most pressing challenge surrounding the use of ultrafast laser is the ablation rate compared to conventional laser ablation systems (and their associated drawbacks including carbonization) and mechanical drilling. It has been described in multiple studies that a femtosecond laser system provides an ablation rate of approximately 1 μm/pulse in hard tissue such as bone at a repetition rate of 10 Hz[81,147]. This is compared to up to 30 μm/pulse for Er:YAG laser systems at a pulse rate of 4 Hz. At this repetition rate, the ablation rate would be 10 μm/sec, compared to 120 μm/sec for conventional laser systems. This can be further compared to mechanical drilling rates of 4–5 mm/s with larger burrs/drill bits that can achieve the ablation volume in a much shorter time. Research is ongoing into higher repetition rate femtosecond laser systems (upwards of 40 KHz) that would mitigate some of the differences through matching the ablation rate; however, the volume ablated per time is still inherently mismatched due to the size of mechanical drilling devices compared to the spot size of ultrafast laser devices[89]. Due to the time constraints of many public operating rooms and the number of patients requiring procedures such as hip and knee arthroplasty, the ablation rate would be required to come close to matching the shaving/feed rate of high-speed mechanical drills for clinical translation.

A second technical challenge for ultrafast laser systems is the adoption of these systems into endoscopic devices for minimally invasive surgery. These approaches are becoming more prevalent in all surgeries including orthopedic due to the potential for reduced tissue trauma and quicker recovery. In these approaches, such as transsphenoidal access or laminectomy, the limitation of ultrafast laser fibers in terms of attenuation and dispersion characteristics have precluded the adoption into endoscopes that are currently in use. Although fibers have been developed for implementation into an endoscope, the cutting power, modal quality, dispersion

and attenuation are dependent on the bending radius, compromising cutting efficiency or ablation rates in these applications altogether. Ongoing research of fibers for integration into endoscopes, which are flexible enough to generate continuous power input, provides the basis to suggest that this problem will be overcome, and adoption would be able to proceed[148–150].

In the scenarios envisioned where ultrafast lasers would potentially be of benefit, there are a number of future directions that should be addressed and examined. Firstly, a method to stop laser ablation as soon as the bone is cut through to prevent a similar laser-induced 'plunge' into tissue such as dura or nervous tissue would need to be developed, similar to the mechanical chuck that has been integrated into cranial perforators[151]. Plunging into inferior tissues such as the dura and/or brain would be of greater detriment compared to any gains made from reduced thermal deposition and reduced thermal damage from either direct brain damage or CSF leakage. A high degree of pre-planning using CT or MRI to determine bone thickness as well as depth control during the procedure would need to be achieved to prevent overcutting at any given volume currently being ablated. This degree of intraoperative control of cutting/ablation would, at a minimum, require a guidance platform demonstrated in procedures such as pedicle screw placement whereby interventional radiology (IR) based navigation is used to track the screw in real time with combined CT guidance[152], and the laser tip/front could be tracked in real time. A second approach would be to combine the ultrafast laser cutting tool with an optical approach such as diffuse reflectance spectroscopy (DRS) where optical properties of incoming tissue can be measured in real time. In combining DRS with ultrafast laser cutting/ablation, the relatively slower speed of laser-based ablation would allow for DRS measurements in combination with real-time optical property measurements, enabling in-line tissue differentiation. Nonetheless, a system of external tracking, such as IR navigation, or with fiber measurements of optical properties, such as DRS, would need to be implemented to prevent overcutting of tissue, leading to dural laceration or nerve/vessel injury that would provide no appreciable benefit to conventional surgical techniques.

Secondly, we propose that in the transition of the use of ultrafast lasers into bone surgery, integration either within a robotic or navigation platform will be necessary to allow for higher success chance in the proposed applications[153]. As mentioned previously, cutting depth is an important parameter in the procedures such as laminectomy or transsphenoidal placement. Surgeons currently use a combination of auditory cues and haptic feedback when assessing depth while drilling, and would not be able to use a laser-based cutting/ablation approach. We

propose that a robotic platform could be developed, including either a navigation device or optical ‘guidance’ system such as DRS. The addition of these platforms can overcome the loss of haptic feedback and auditory cues normally used by surgeons while maintaining the safety of the procedure. This can be expanded to include semi-autonomous or AI-driven robotic platforms where surgeons design cutting paths in conjunction with a robotic laser-based system that could perform cutting procedures, such as removal of the sphenoid bone or lamina with minimal surgeon oversight. This type of platform is appealing as it would lead to a reduction in exposure to X-rays to both patients and operators, commonly encountered in many orthopedic procedures and secondly, increase overall outcomes due to increased osteointegration and reduced thermal deposition.

Finally, laser systems and fibers need to be developed that can provide both high ablation rates and flexibility that would allow for integration into currently existing minimally invasive surgical devices. In terms of ablation rates, the rate would need to at least approximate the ablation rate of mechanical drills (4–5 mm/sec) as well as approximating the ablation volume. For example, in orthopedic surgery the drill bit size would be 6-8 mm with the aforementioned ablation rate in procedures such as hip and knee arthroplasty. It could be argued that with the added benefits of limited thermal deposition and improved wound healing, some leeway could be given to the ablation rate of bone; however, it needs to be fast enough to not unduly delay these procedures. With this in mind, ultrafast laser systems would be more beneficial in endoscopic-based ablation procedures where the ablation rate is not the limiting factor with the burrs commonly used being much smaller (0.5–1.0 mm), and thus the gap between ablation volume not as large. In these procedures, the benefits of ultrafast laser ablation combined with the more closely matched laser spot size and burr size would allow for an easier transition without unduly delaying any procedures. In this case, fiber development would need to allow for shaper bending radii without an impact on laser performance.

1.4.9 Subsection Summary

In examining the osteointegrative potential and hard tissue ablation, the use of ultrafast lasers in a number of surgical procedures such as total/hip knee arthroplasty, laminectomy and transsphenoidal resection could lead to meaningful benefits to both patients and operators; specifically, surface treatment of custom 3D-printed implants for patients, where ultrafast laser modification could address one of the limitations of increased implant loosening without the use of cement and lead to further adoption. In addition, reduced thermal damage to surrounding

tissues with laser cutting/ablation in areas adjacent to critical structures, such as in transsphenoidal resection, highlights one of the benefits ultrafast lasers can provide. Overall, with further research, specifically in flexible fiber technology without loss of ablation potential, ultrafast lasers can provide a notable change in outcomes and workflows in the surgical procedures emphasized in the subsection.

1.5 Thesis Design and Scope

1.5.1 Motivation

The motivation for this thesis stems from the clinical need of improved intraoperative guidance for bone-related surgeries in orthopedics and neurosurgery. The current surgical techniques and tools involved to gain access in hard tissues for screw placements, burr hole creations and implant fixation pose greater risks of accidental injuries to the patients, leading to prolonged recovery time and potentially deteriorated quality-of-life. Although innovative technologies such as real-time 3D navigation and robotics have been developed to optimize intraoperative localization and alignment, optical sensing can provide additional benefits, possibly as a multi-modal platform, by supplying precise guidance for point-of-care. On the other hand, there remains a lack of optically enhanced surgical tools for bone-related procedures. This thesis is motivated by both the clinical and technical challenges to address the potential of optical sensing in the field of orthopedics and neurosurgery and contributes to the development of integrated surgical devices that can be translated into the clinics in the future.

1.5.2 Hypothesis

The hypothesis for this thesis is that optically enhanced surgical guidance can improve intraoperative precision and accuracy by acting as a safety measure and providing real-time feedback information to differentiate tissue types. Furthermore, adequate reduction in instrumentation complexity as well as computational burden can expedite the development of optical integration with the existing surgical tools. The hypothesis is established based on previously published research in the literature, suggesting improvements in surgical guidance with optical sensing. Moreover, optical solutions are minimally invasive, cost-efficient and user-friendly with the capability of being readily miniaturized.

1.5.3 Aims and Objectives

The overall aim of this thesis is to evaluate the performance of optical sensing techniques to differentiate common tissue types encountered during orthopedic and neurosurgical procedures, and subsequently determine a strategy to reduce instrumentation complexity and computational burden.

Specifically, the thesis objectives are listed as the following:

1. To systematically evaluate the use of DRS to assist intraoperative guidance in bone-related procedures.
    a. To evaluate the performance of DRS in classifying different tissue types (Chapter 2, Chapter 3 and Chapter 5).
    b. To evaluate the performance of DRS in predicting depth in hard tissues (Chapter 2 and Chapter 4).
2. To identify an approach to reduce instrumentation complexity and computational burden based on DRS technology.
    a. To develop feature selection frameworks that determine wavelength features of optimal discriminative power (Chapter 3).
    b. To assess the performance of the selected wavelength features as DRS illumination light source (Chapter 3 and Chapter 4).
3. To investigate the potential of ultrafast lasers as a surgical tool in bone-related procedures.
    a. To systematically evaluate the clinical relevance of ultrafast lasers in orthopedic surgery (Chapter 1).
    b. To utilize ultrafast lasers to generate plumes for assessment by ambient mass spectrometry and determine the classification accuracy among different tissue types (Chapter 5).

1.5.4 Significance

The thesis contributes to the advancement of integrating optical sensing into surgical tools for orthopedics and neurosurgery. By examining the role of DRS in differentiating tissue types and

developing frameworks to select important wavelength features, the research sets the foundation for future translational studies by understanding the knowledge space of DRS in bone-related procedures and providing a platform that can be adapted to other spectral datasets. Furthermore, by conducting preliminary studies using ultrafast lasers, valuable insights are gained for developing multi-modal platforms with the emphasis on the benefits from each modality. This thesis not only addresses the development of basic science but also extends to clinical scenarios. The importance and implications of this research can inform innovative avenues to further scientific understanding and drive scientific progress.

1.6 Thesis Outline

The thesis is structured as follows:

Chapter 1 introduces background knowledge and summarizes the scope of the thesis, where the literature review of ultrafast lasers is based on the published review article:

- Li CL, Fisher CJ, Burke R, Andersson-Engels S. Orthopedics-Related Applications of Ultrafast Laser and Its Recent Advances. *Applied Sciences*. 2022;12(8):3957. doi: https://doi.org/10.3390/app12083957.

Chapter 2 elucidates the creation of the relevant DRS datasets for use with machine learning and deep learning techniques. This chapter is based on the published data descriptor article:

- Li CL, Fisher CJ, Komolibus K, et al. Extended-wavelength diffuse reflectance spectroscopy dataset of animal tissues for bone-related biomedical applications. *Sci Data*. 2024;11(1):136. doi: https://doi.org/10.1038/s41597-024-02972-3.

Chapter 3 describes the development of four feature selection frameworks for DRS datasets. This chapter is based on the published original research article:

- Li CL, Fisher CJ, Komolibus K, et al. Frameworks of wavelength selection in diffuse reflectance spectroscopy for tissue differentiation in orthopedic surgery. *J Biomed Opt*. 2023;28(12). doi: https://doi.org/10.1117/1.JBO.28.12.121207.

Chapter 4 discusses depth predictions in cranial bones using DRS combined with machine learning and deep learning techniques. This chapter is based on the ongoing original research manuscript:

- (In progress) Li CL, Fisher CJ, Komolibus K, et al. Depth prediction in cranial bones using diffuse reflectance spectroscopy for craniotomy. *Biomed Opt Express*. 2024.

Chapter 5 presents two preliminary studies on the probe design and the use of ambient mass spectroscopy for tissue differentiation, and subsequently concludes the thesis. The study on the probe design is based on the conference proceedings:

- (Oral Presentation) Li CL, Fisher CJ, Komolibus K, et al. Design and concept of a miniaturized optical probe for guidance of bone cement removal in orthopedic surgery. *European Conferences on Biomedical Optics.* 29 June 2023.

Chapter 2
Extended-wavelength diffuse reflectance spectroscopy dataset for bone-related biomedical applications

2.1 Chapter Overview

This chapter describes data collection and preparation in detail to set the basis for subsequent data analysis utilizing machine learning and deep learning techniques. The primary objective of this chapter is to provide a comprehensive explanation of the methodology employed by outlining the specific materials, equipment and procedures used during the experiments. Moreover, the dataset has been made publicly available for reuse as well as to ensure the reproducibility of the research presented in this thesis.

Diffuse reflectance spectroscopy (DRS) has been extensively studied in both preclinical and clinical settings for multiple applications, notably as a minimally invasive diagnostic tool for tissue identification and disease delineation. In this chapter, extended-wavelength DRS (EWDRS) measurements of *ex vivo* tissues ranging from ultraviolet through visible to the short-wave infrared region (355 – 1919 nm) are presented in two datasets. The first dataset contains labelled EWDRS measurements collected from bone cement samples and ovine specimens including 10 tissue types commonly encountered in orthopedic surgeries for data curation purposes. The other dataset includes labelled EWDRS measurements of primarily bone structures at different depths during stepwise drilling into intact porcine skulls until plunging into the cranial cavity. The raw data with code for pre-processing and calibration is publicly available for reuse on figshare and Zenodo. The datasets can be utilized not only for exploratory purposes in machine learning model construction, but also for knowledge discovery in the orthopedic domain to identify important features for surgical guidance, extract physiological parameters and provide diagnostic insights.

This chapter is based on the published data descriptor[154]:

Li CL, Fisher CJ, Komolibus K, et al. Extended-wavelength diffuse reflectance spectroscopy dataset of animal tissues for bone-related biomedical applications. *Sci Data*. 2024;11(1):136. doi:10.1038/s41597-024-02972-3

2.2 Background and Summary

Orthopedic and neurosurgical specialties encompass the majority of bone-related surgical interventions to treat musculoskeletal or neurological conditions, which routinely require the surgeon to operate on both hard and soft tissues while avoiding damage to the surrounding vital organs including brain, spinal cord and major peripheral nerves. General orthopedic surgeries, such as total knee arthroplasty, and spine surgery, such as laminectomy, represented two of the three most frequently performed procedures in the United States in 2012[1], mainly owing to population ageing. By 2018, spine fusion, knee and hip arthroplasty became the top three most costly principal operating room (OR) procedures, constituting approximately 24% of the top 20 OR procedures[2]. The incidence rate projection has also demonstrated a significant uptrend in the number of surgical cases to 2060, indicating an increase by 560% for primary total joint arthroplasty[155,156] and 270% for posterior spinal fusion in patients aged >75 years[157]. In response to the growing demand, the number of orthopedic and neurological surgeons increased by 11% and 9%, respectively, from 2012 to 2017[158].

Despite the increase in demand of orthopedic and neuro- surgery, reluctance of drilling is frequently witnessed with early-career practitioners due to insufficient experience and fear of excessive perforation causing severe damage[159]. Studies have found that surgical learning curves to these high-volume procedures can be significantly steep, requiring a substantial amount of time, effort and practice before mastery is attained[160–162]. The need for extensive training or new guidance devices thus becomes imperative to improve operative efficiency, patient outcome and safety. The risk of plunging and breaching into critical structures can be greatly reduced by implementing safety measures into the surgical tools so that either the mechanical processes can be automatically terminated in a timely manner, or the exact drilling speed and depth can be monitored in real time. Several approaches have been investigated including optical methods[163,164], surgical techniques[165–167] and mechanical tools[168,169]. It has, however, remained technically challenging for surgeons to navigate through bone-related surgical procedures because of limited visibility and a restricted field of view, though various intraoperative imaging techniques can be utilized for enhanced visualization and accuracy combined with computer-assisted technologies[170–172].

Diffuse reflectance spectroscopy (DRS) is an established technique routinely used for measuring electromagnetic radiation reflected off sample surfaces as a function of wavelength or frequency[173]. The utilization of DRS in preclinical and clinical settings has been extensively

studied for the purpose of diagnostic guidance in a wide range of applications, notably as a promising aid to cancer delineation in breast[174], liver[175] and gastrointestinal tract[176]. With relatively low-cost instrumentation and easy maneuverability, this spectroscopy method can offer non-contact to minimally invasive, usually point-based interrogation of tissues of interest based on their wavelength dependent absorption and scattering properties. Furthermore, machine learning (ML) algorithms are often seen deployed on DRS datasets for tissue classification and parameter extraction due to the information-rich nature[177–179]. ML can facilitate selection of the most important spectral features and help evaluate the diagnostic power of the technique.

Recently our and other groups introduced and discussed perspectives on optical integration to guide bone-related surgeries, of which the proposed techniques could potentially provide more effective surgical approaches with less side effects[180–182]. Along these lines we have demonstrated the potential of DRS for tissue differentiation in orthopedic procedures[183–185], and subsequently described four distinct feature selection frameworks formulated based on DRS measurements[186]. The aim of this specific publication was to discover a reduced number of wavelength features with sufficient discriminative power for tissue differentiation, thus decreasing instrumentation complexity of optical systems for clinical translation.

The publications in this field are, however, so far scarce and there is a need for more open-source data. This study was thereby designed to facilitate data re-utilization and the development of ML models for data mining tasks in bone-related biomedical applications. Two datasets are included with a technical analysis as validity check. Both datasets fulfill the pre-requisites for ML and deep learning (DL) techniques by collecting sufficiently large data libraries with labels from multiple *ex vivo* tissue specimens.

In this chapter, we explain in detail the experimental collection of two extended-wavelength DRS (EWDRS) datasets. EWDRS measurements ranging from 355 to 1919 nm were acquired from *ex vivo* specimens sourced from a local butcher shop in Cork, Ireland. All measurements were conducted employing a broadband light source for illumination with two commercialized spectrometers for simultaneous signal detection. As shown in Fig. 2.2.1a, measurements were acquired in a grid pattern of ~5 mm apart, while Fig. 2.2.1b summarizes the workflow of EWDRS data pre-processing.

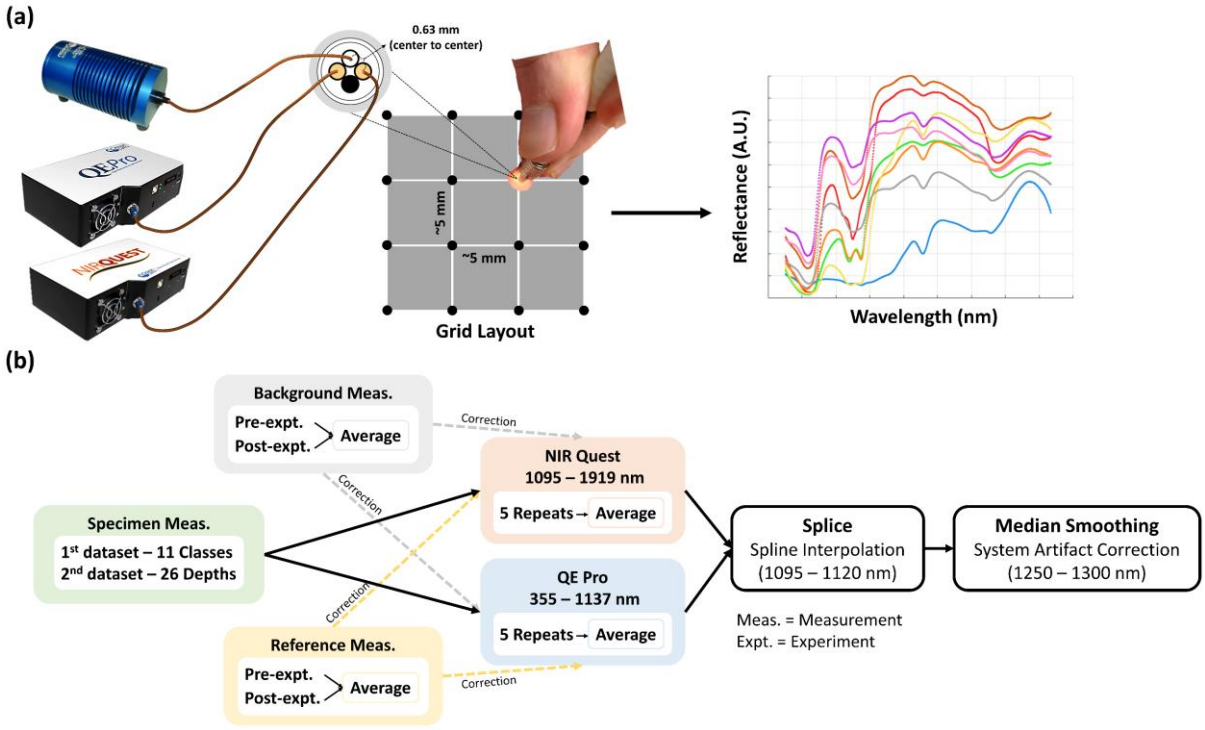


Figure 2.2.1 EWDRS dataset collection and pre-processing workflow. (a) Modified from the publication[186]. Experimental setup included two commercialized spectrometers and a tungsten-halogen broadband light source. The source-detector separations were 0.63 mm from center to center. The locations of measurements followed a grid layout of approximately 5 mm apart for all specimens. (b) Data pre-processing consisted of background correction, reference calibration, spectral splicing using spline interpolation and median smoothing.

The first dataset (Dataset 1) was created for general orthopedic applications and skull-based procedures, which included tissue types commonly encountered during the relevant surgical operations. As shown in Fig. 2.2.2a, Dataset 1 comprised data from 10 biological tissue types of ovine specimens, which were bone marrow, cartilage, cortical bone, endosteum, fat, muscle, trabecular bone, dura, grey and white matter. One non-biological specimen, namely bone cement, was also included in this dataset (Fig. 2.2.2c) since the targeted clinical application was optical guidance of bone cement removal in total hip arthroplasty. Part I of Dataset 1, including class labels for bone marrow, cartilage, cortical bone, muscle, trabecular bone and bone cement, can be found on Zenodo[187], while Part II, including class labels for endosteum, fat, dura, grey and white matter, can be found on figshare[188]. The second dataset (Dataset 2) was created for neurosurgical applications involving craniotomy, which included depth measurements of porcine skulls. This dataset consisted of EWDRS measurements of primarily

cortical bone at different depths during stepwise drilling of porcine skulls until plunging into the cranial cavity (Fig. 2.2.2b).

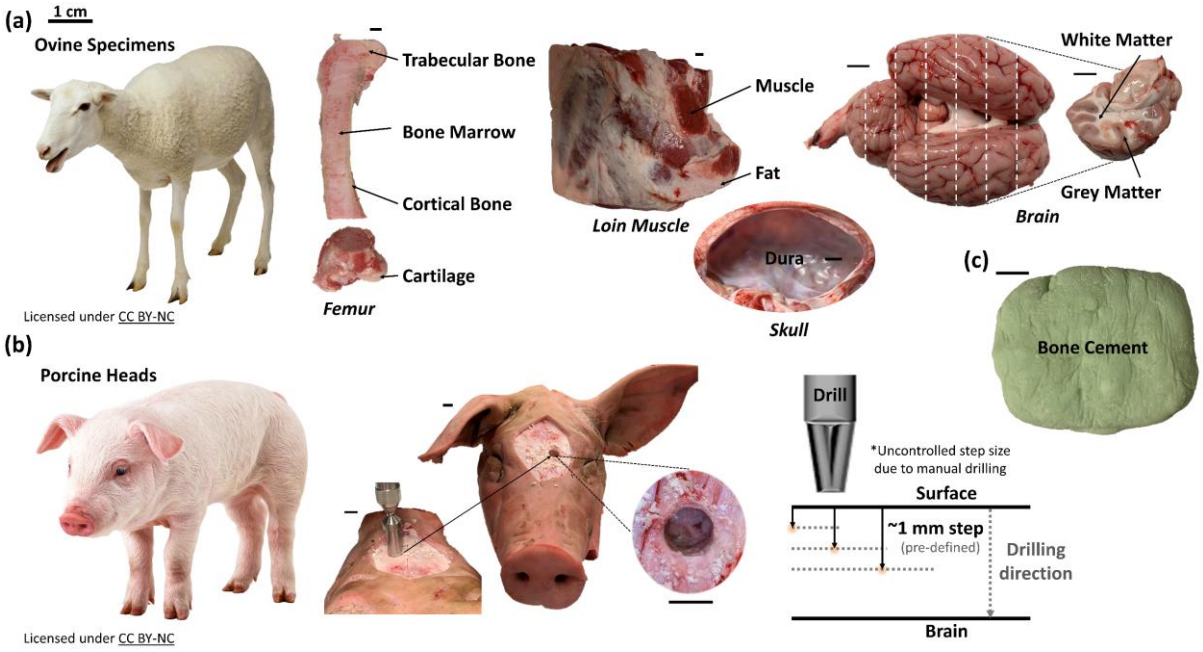


Figure 2.2.2 Example *ex vivo* specimens used for EWDRS dataset creation. (a) Ovine specimens included bone marrow, cartilage, cortical bone, trabecular bone (femur), dura, fat, muscle, grey and white matter (brain). Whole brain tissues were extracted from ovine cranial cavities and sectioned along the coronal plane to expose grey and white matter. (b) Stepwise drilling was performed manually on porcine heads into the cranial cavity from the surface. The step size was pre-defined to be 1 mm but was uncontrolled during drilling due to manual handling. EWDRS measurements were taken at each stop. (c) Adapted from the publication[186]. Bone cement samples were cured and hand-molded into blocks. The black scale bars represent 1 cm.

The collection of the published data library was motivated by the need to identify important spectral features for surgical guidance and better comprehend the knowledge space of DRS relating to orthopedics and neurosurgeries. The exploration could set the groundwork to select adequate wavelengths for tissue differentiation, predict layer thickness of cranial bones and benchmark classification metrics as a reference. For reuse, we believe that the data is useful for translational optics research and can enable the possibility to develop suitable ML or DL models utilizing DRS measurements. It can also boost the deployment of medical DL approaches based on EWDRS through transfer learning, which has gained considerable attention recently in spectroscopy[189,190]. While there has been spectroscopy data published in the literature[191], our data library not only encompasses a significantly broader spectral range

covering the ultraviolet A, visible, near infrared and short-wave infrared (UVA/VIS/NIR/SWIR) windows, but also provides measurements of more biological tissue types in greater amounts.

2.3 Methods

The following subsections describe the full experimental protocols of data collection and pre-processing expanded upon the previous work[186]. All *ex vivo* measurements were approved by and in compliance with the regulations at Tyndall National Institute, Cork, Ireland.

2.3.1 Specimen Preparation and Setup

All *ex vivo* specimens, from animals slaughtered two days prior to experiments, were immediately refrigerated until two hours before measurements on the same delivery day. The tissue specimens were unprocessed in the natural condition and kept moist at room temperature using saline spray during all experiments.

For Dataset 1 (Fig. 2.2.2a), femoral specimens containing bone marrow, cartilage, cortical bone and trabecular bone were approximately 23-cm long and 3-cm in diameter on average. Muscle specimens containing muscle and fat were approximately 22×23×8 cm on average. The cross sectional opening of ovine skulls representing dura was approximately 9×5 cm on average. Brain containing grey and white matter was approximately 11×8×3 cm on average in the relaxed form, which was sectioned coronally into approximately 1-cm thick slabs. Bone cement (PALACOS® R+G pro, Heraeus Medical GmbH, Wehrheim, Germany) samples were cured and hand-molded into approximately 6×5×4-cm blocks (Fig. 2.2.2c) one day beforehand. Dataset 2 included EWDRS measurements acquired from 5 porcine heads, of which the superficial layer of skin and connective tissue were shaved off to expose the skull (Fig. 2.2.2b). A commercial surgical drill (CD4, Stryker, USA) as previously reported[185] with no optical enhancement was employed, which was manually handled for drilling to closely approximate a stepwise thickness of 1 mm. No a priori knowledge of skull thickness was obtained. The thickness of the cranial bone was variable depending on the initial drilling location. As a result, the exact drilling depth per stop was uncontrolled, leading to a different number of measurements recorded at each pre-defined depth level. For instance, no measurement was collected at 23-mm thickness of the skull.

2.3.2 Extended-wavelength Diffuse Reflectance Spectroscopy

The experimental system is illustrated in Fig. 2.2.1a, with the data pre-processing shown in Fig. 2.2.1b. The DRS system consisted of dual spectrometers, measuring the 355 to 1137 -nm range (QEPro-FL, QE Pro spectrometer, Ocean Insight B.V., Duiven, The Netherlands) with approximately 6.9 nm optical resolution and a spectral bin width of approximately 0.76 nm, and the 1095 to 1919 -nm range (NIRQUEST512-1.9, NIR Quest spectrometer, Ocean Insight B.V., Duiven, The Netherlands) with approximately 12.3 nm optical resolution and a spectral bin width of approximately 1.6 nm per channel, respectively. The specimens were illuminated by a tungsten-halogen light source (8.8 mW, 350 – 2400 nm, HL-2000-HP, Ocean Insight B.V., Duiven, The Netherlands) and probed for 2 s by a commercialized fiberoptic bundle (BF46LS01, 600-μm core, Low OH, Thorlabs, Munich, Germany) as shown in Fig. 2.2.1a. The fiber optic probe was a 1-to-4 fan-out bundle, of which only three fiber channels were used. The source-detector separations were 0.63 mm from center to center between channels on the probe. Both background (without illumination light) and reference (with illumination light) measurements against a reflectance standard (FWS-99-01c, Avian Technologies LLC, New London, USA) were collected pre and post each experimental session with the same acquisition setting. For data acquisition, 5 repeats were included for each spectrometer. During each repeat, 250 spectra and 1 spectrum were recorded by the QE Pro spectrometer and the NIR Quest spectrometer with an individual exposure time of 8 ms and 2 s, respectively, to achieve a good signal-to-noise ratio. All specimens in Part II of Dataset 1 except dura were prepared with at least a 1-cm thickness. Dura was prepared as a single layer membrane. The overlapped region was utilized for merging and splicing spectra from the two spectrometers together as a continuum. It is recommended to trim off the spectral range beyond 1850 nm for further interpretive analysis due to increased noise level. One measurement is equivalent to one EWDRS spectrum. Specific details for the two datasets are summarized in Table 2.3.1.

Table 2.3.1 Summary of the EWDRS measurements included in Dataset 1 (left) and Dataset 2 (right).

	Dataset 1		
	Spec. Type	**No. of Spec.**	**No. of Meas.**
Part I	Bone Marrow	43	1000
	Cartilage	55	1000
	Cortical Bone	48	1000
	Muscle	31	1000
	Trabecular Bone	47	1000
	Bone Cement	3	215
Part II	Endosteum	38	245
	Fat	28	1000
	Dura	9	215
	Grey Matter	78	413
	White Matter	92	436
	Total	472	7524

Dataset 2	
No. of Heads	5
No. of Drilled Holes	11
No. of Meas.	102
Min. Thickness (mm)	0 (brain)
Max. Thickness (mm)	25 (surface)

Spec. = Specimen

Meas. = Measurements

No. = Number

Max. = Maximum

Min. = Minimum

Thickness = Distance away from the brain

2.3.3 Data Pre-processing

Data pre-processing was implemented in both the Python Programming Language Version 3.9 (Python Software Foundation, https://www.python.org/) and MATLAB (R2020b, The MathWorks Inc., Natick, Massachusetts, USA, https://www.mathworks.com). All code scripts for data pre-processing described here can be found in Code Availability. Due to the dual spectrometer configuration, two spectra were generated. Splicing via spline interpolation was performed over a selected range between 1095 and 1120 nm of the overlapped region using 1D interpolation (MATLAB default function). Background correction and reference calibration were calculated by Eqn. 2.3.1:

$$\textbf{\textit{Calibrated EWDRS spectrum}} = \frac{S_{raw} - S_{bkgd}}{S_{ref} - S_{bkgd}}, \qquad \textbf{\textit{(Equation 2.3.1)}}$$

where S_{raw} represents the averaged raw DRS spectrum over the five repeats, S_{bkgd} represents the averaged DRS spectrum of the background pre and post the experiment, and S_{ref} represents the averaged DRS spectrum of the reflectance standard pre and post the experiment. The spectral bin width over the spliced region was 0.23 nm. Class labels were recorded in the last column for both datasets. A systematic artifact from the spectrometer between 1250 and 1300 nm was corrected by a smoothing method using moving median with a window size of 2.2 (nm). Standard normal variate (SNV) transformation, a spectral scaling technique calculated by Eqn. 2.3.2, was used as scattering correction to remove unrelated offsets:

$$\boldsymbol{SNV\ EWDRS\ spectrum} = \frac{(S_{cal} - \overline{S_{cal}})}{SD(S_{cal})}, \textbf{\textit{(Equation 2.3.2)}}$$

where S_{cal} represents the calibrated spectrum from Eqn. 2.3.1, $\overline{S_{cal}}$ represents the mean of S_{cal} and $SD(S_{cal})$ represents the standard deviation (SD) of S_{cal}. Fig. 2.3.1 illustrates the averaged spectra for all labels in the two datasets, excluding the spectral range from 1850 to 1919 nm.

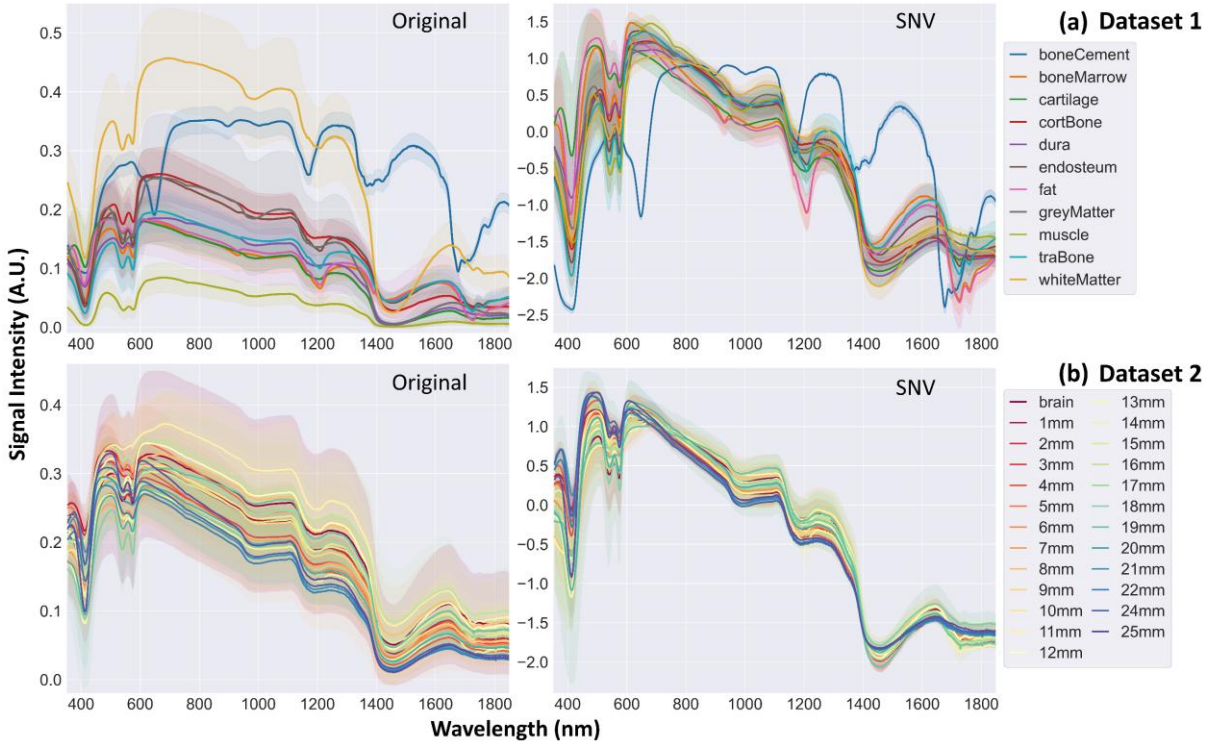


Figure 2.3.1 The averaged EWDRS spectra for all labels in (a) Dataset 1 and (b) Dataset 2 showing the original spectra (left) and the SNV transformed spectra (right). SDs are shown by shaded error bands. Spectral range beyond 1850 nm was trimmed off.

2.4 Data Records

Part I of Dataset 1 are publicly available in a Zenodo repository[187], while Part II of Dataset 1 and the full Dataset 2 can be found in a figshare repository[188]. The pre-processed data is stored in CSV files with headers (wavelengths) in the first row and class labels (tissue types or thicknesses) in the last column. Both the original and the SNV transformed data are provided in separate CSV files. There are 7524 and 102 EWDRS measurements in the full Dataset 1 and Dataset 2, respectively, and 1531 wavelength channels in total (trimmed beyond 1850 nm). The full Dataset 1 in one CSV file for easy access and formatting is available upon request. The class label column of Dataset 2 is formatted in both strings and numerical values in separate files for easier utilization with classification and regression tasks, respectively. Raw data with background and reference measurements is provided in both CSV files and MAT files. Metadata and licensing information are stored in the corresponding dataset folders.

The Dataset 1 folder "EWDRS_dataset_ortho" contains:

EWDRS_dataset_ortho/

- raw_data_archive/ (Wavelength Range: 355 – 1919 nm)
    - 15 subfolders (e.g. Expt_Dat_01/) representing individual experimental sessions containing:
        - cal_proc_csv/ including calibrated and processed data in CSV.
        - cal_proc_mat/ including the same as above in MAT.
        - cal_proc_plot_norm/ including normalized spectral plots.
        - raw_csv/ including raw, background, reference data in CSV.
        - raw_mat/ including raw, background, reference data in MAT.
- all_EWDRS_meas_cal_proc_new.csv: the processed original dataset (Part II), 355 – 1850 nm.
- all_EWDRS_meas_cal_proc_new_SNV.csv: the SNV transformed dataset of above.
- number_of_samples_ortho.xlsx: detailed information on specimens for each experiment.
- LICENSE.txt: licensing information.
- README.txt: basic information of the dataset.

The Dataset 2 folder "EWDRS_dataset_drilling_depth" contains:

EWDRS_dataset_drilling_depth/

- cal_proc_csv/ including 26 CSV files of calibrated and processed data for individual class labels, 355 – 1919 nm.
- cal_proc_mat/ including the same as above in MAT.
- drilling_cal_proc_all.csv: the fully processed original dataset with class labels in strings, 355 – 1850 nm.
- drilling_cal_proc_all_snv.csv: the SNV transformed dataset of above.
- drilling_cal_proc_all_regr.csv: the fully processed original dataset with class labels in numerical values, 355 – 1850 nm.
- drilling_cal_proc_all_snv_regr.csv: the SNV transformed dataset of above.
- LICENSE.txt: licensing information.
- README.txt: basic information of the dataset.

2.5 Technical Validation

Technical validation and integrity were ensured by following rigorous experimental protocols and data pre-processing steps. Data was acquired under controlled environmental factors from *ex vivo* specimens that were prepared and handled consistently throughout all sessions. Tissue identification was confirmed by a medical resident. Background and reference measurements against the same reference standard were always collected pre and post each experimental session to account for both inter- and intra- day variations and offsets using the standard correction method (Eqn. 2.3.1). The selected wavelength range spanning the UVA/VIS/NIR/SWIR windows was appropriate with the use of the illumination light source to provide more spectral information. No tissue damage was identified from the use of the light source.

Upon initial examination of the original spectral curves in Fig. 2.3.1, spectral features of typical biomarkers demonstrating absorption were detected, including oxy-hemoglobin near 414, 543 and 577 nm, deoxy-hemoglobin near 433 and 556 nm, as well as collagen, lipids and water near 1200, 1430 and 1750 nm[192], respectively, which were comparable to the literature[193]. The magnitude of SDs was variable depending on the class label while the error bands followed the same trend as the averaged spectra. For Dataset 1, brain tissue demonstrated the most variations, where the maximum was found in grey matter showing a ± 0.11 SD at 695 nm with an original data value of 0.25. For Dataset 2, the maximum was also found in brain showing a ± 0.13 SD at 875 nm with an original data value of 0.28. The behavior broadly suggested that no presence of outlier was detected, and the degree of variability was primarily caused by

intrinsic specimen heterogeneity. This was further verified by the observation that SDs diminished significantly after applying SNV transformation, especially for Dataset 1. Larger variations were indeed found near the spectral absorption features. The degree of SDs on the SNV-transformed Dataset 2 was marginally variable, as expected, because the data was mostly acquired from the same biological tissue type. Due to low noise level in the entire spectra, data smoothing was only applied to correct one systematic artifact instead of the whole range.

The two datasets encompass a sufficiently large amount of EWDRS measurements for use in ML and DL modeling. More data can be reproduced efficiently and reliably following the steps outlined here. Class imbalance can else be corrected by over-sampling techniques such as Synthetic Minority Over-sampling Technique (SMOTE) or under-sampling methods using K-means or nearest neighbors algorithms. Technical limitations not only existed in the instrument setup since measurements were collected from two adjacent acquisition volumes, but also in the experimental environment because the reported data was not collected from an *in vivo* setting and thus became less adequate for simulating ongoing clinical scenarios. Since diffuse reflectance measurements are predominantly dependent and governed by the optical properties of samples of interest, the physiological elements present in *in vivo* settings such as heart rate, respiratory rate and hemodynamics exert a significant impact on the optical property measurements. The resulting DRS measurements could exhibit dynamic behaviors due to the changing oxygenation levels. In addition, sample limitations were found in the *ex vivo* non-human specimens employed in the study. The findings might not be completely generalizable to clinical scenarios due to altered amounts of blood, lipid, collagen and water contents as well as the oxygenation states of hemoglobin and overall different tissue microenvironments as compared to human specimens, which would lead to changed optical properties and DRS measurements as compared to clinical trials[194]. For instance, DRS measurements of muscle tissue, one of the relevant tissue types in bone-related surgical procedures, is mainly influenced by the optical behavior (absorption) of hemoglobin and water contents. The interspecies differences in optical properties of muscle can be substantial among human, porcine, ovine, rat and rabbit specimens[195]. For bone tissues, distinct interspecies differences between animal models and humans have been demonstrated in bone composition, bone density and bone quality, with the most pronounced difference determined in lumbar spine[196]. Such limitations specifically existing in animal-to-human as well as *ex-vivo*-to-*in-vivo* translations could all be treated as contributing factors to translational failure. Nevertheless, porcine models demonstrate gross similarities in optical properties and tissue heterogeneity with human

subjects such as in brain and bone, and have been seen increasingly used in orthopedic research[194,197–199]. It is therefore believed that the present dataset can serve for reuse to facilitate development of clinical optical diagnostic and monitoring tools with artificial intelligence implementation.

2.6 Code Availability

Example codes are publicly available in a Github repository at: https://github.com/Biophotonics-Tyndall/PUB-DataDescriptorCode.git.

The repository contains one MATLAB script (DRS_cal_proc_example.m) demonstrating DRS data processing and systematic artifact correction, one Python function (calibDRS.py) for SNV transformation, and three MATLAB functions to namely calculate area-under-curve (AUC_DRS_fnc.m), splice two spectra via spline interpolation (DRS_splice_fnc.m) and calculate SNV transformation (snv_DRS_fnc.m) for DRS data.

With the fundamental aspects of data collection and experimental preparation established in the current chapter, the focus in the next chapter will shift to an important phase of the thesis research – Feature Selection in DRS. Robust and adaptable feature selection frameworks are crucial for surgical device development in DRS research as it assists with reducing instrumentation complexities. In this context, the methodology formulated for DRS feature selection becomes pivotal in enhancing machine learning model accuracy as well as improving the physical understanding of the knowledge space.

Chapter 3
Frameworks of wavelength Selection in diffuse reflectance spectroscopy for tissue differentiation in orthopedic surgery

3.1 Chapter Overview

This chapter describes the formulation of feature selection frameworks based on machine learning techniques, which was specifically developed for spectral data acquired from the previous chapter. The primary objective of this chapter is to demonstrate the utility of feature selection and provide a thorough explanation of the frameworks with a high degree of adaptability. Based on the results, important wavelengths can be selected and thus reduce instrumentation complexity.

Significance: Wavelength selection from a large diffuse reflectance spectroscopy (DRS) dataset enables removal of spectral multicollinearity and thus leads to improved understanding of the feature domain. Feature selection frameworks are essential to discover the optimal wavelengths for tissue differentiation in DRS-based measurements, which can facilitate the development of compact multispectral optical systems with suitable illumination wavelengths for clinical translation. **Aim:** The aim was to develop a feature selection methodology to determine wavelengths with optimal discriminative power for orthopedic applications, while providing the frameworks for adaptation to other clinical scenarios. **Approach:** An ensemble framework for feature selection was developed, validated and compared with frameworks incorporating conventional algorithms including principal component analysis (PCA), linear discriminant analysis (LDA), and backward interval partial least squares (biPLS). **Results:** Via the one-vs-rest binary classification approach, a feature subset of 10 wavelengths was selected from each framework yielding comparable balanced accuracy scores (PCA: 94.8 ± 3.47%; LDA: 98.2 ± 2.02%; biPLS: 95.8 ± 3.04%; Ensemble: 95.8 ± 3.16%) to those of using all features (100%) for cortical bone versus the rest class labels. 100% balanced accuracy scores

were generated for bone cement versus the rest. Different feature subsets achieving similar outcomes could be identified due to spectral multicollinearity. **Conclusions:** Wavelength selection frameworks provide a means to explore domain knowledge and discover important contributors to classification in spectroscopy. The ensemble framework generated a model with improved interpretability and preserved physical interpretation, which serves as the basis to determine illumination wavelengths in optical instrumentation design.

This chapter is based on the original research[200]:

Li CL, Fisher CJ, Komolibus K, et al. Frameworks of wavelength selection in diffuse reflectance spectroscopy for tissue differentiation in orthopedic surgery. *J Biomed Opt*. 2023;28(12). doi:10.1117/1.JBO.28.12.121207

3.2 Introduction

Surgical procedures involving osteotomies pose challenges and risks to breaching and plunging into critical neurovascular and musculoskeletal structures, often leading to operative morbidity or potentially mortality. One of the related clinical situations involves total hip and knee arthroplasty (THA/TKA) where periprosthetic fracture is considered as a major complication that requires revision. One study has found that 40% and 54% of primary THA and TKA patients, respectively, encountered at least one major complication such as fracture or one minor complication such as neurovasculature damage, or both[201,202]. Furthermore, with population ageing leading to rapidly growing incidence of primary arthroplasty, the number of revision surgeries will continue to increase substantially due to limited implant survivorship. The advanced surgical complexity and higher rates of associated complications with revision cases have become a prevalent concern that remains to be improved. Within orthopedics, incidence projections of revision total hip and total knee arthroplasty (rTHA/rTKA) to 2030 in the United States alone have indicated an increase of 43% - 70% and 78% - 182%, respectively, relative to the 50K rTHA and 72K rTKA cases recorded in 2014. In particular, the age group younger than 55 years is anticipated to undergo the highest increase of such procedures, suggesting that multiple revision surgeries would become necessary in the coming decades with implant failures in younger patients. Some common causes for rTHA include instability (28%), aseptic loosening (24%), periprosthetic fracture (18%) and prosthetic joint infection (18%)[203].

Our group previously proposed perspectives to integrating optical sensing into orthopedic surgical tools in the effort to stimulate innovations in translational biophotonics[180], and demonstrated preliminary results for tissue differentiation based on diffuse reflectance spectroscopy (DRS) measurements of tissue types encountered in general orthopedic surgery[183,204,205]. Despite many other clinical use-cases, we have explicitly examined the possibility of optical integration to guide cement removal – one of the most technically challenging and time-consuming steps for surgeons during rTHA/rTKA surgery, especially removal of the distal cement plug. Choices of intraoperative image guidance modalities such as endoscopy, fluoroscopy or ultrasound[206–208] are usually surgeon dependent, which can nonetheless be cumbersome and impractical to integrate in the operating room. Navigation through the procedure is therefore frequently dependent on the surgeon's experience as well as the safety measures implemented in the surgical tool. On the other hand, extraction of well-bound bone cement can be undesirably invasive under certain circumstances when, for

instance, creation of cortical windows is needed in the femur via trochanteric osteotomy to visualize the distal plug upon a failed initial attempt[209,210]. Severe complications including cortex perforation (5%) and intraoperative fracture (12%), as well as overall incomplete implant or cement extraction, can be associated with insufficient familiarity and expertise in the surgical procedure leading to prolonged postoperative recovery and higher infection rates, while several techniques and instruments such as cement-in-cement revision and ultrasonic cement removal have been employed to ameliorate the risk[211–213].

With this succinct background, we here consider the potential role of DRS measurements, as a means of integrated optical guidance in complement to standard imaging modalities, to assist the orthopedic surgeon with 1) differentiating bone cement[214] from biological tissues, 2) informing cement-to-bone interface as a safety measure to signal pre-breaching and 3) informing bone-to-tissue interface as an indicator to signal post-breaching during rTHA involving cemented implants. One of the advantages of DRS lies in the possibility of instrument miniaturization and hence easier integration to surgical workflows; the choice of discrete narrowband light sources can nonetheless be variable in different applications and sometimes inadequate without a selection methodology. In general, the utilization of DRS in preclinical and clinical settings has been extensively studied for the purpose of diagnostic guidance in a wide range of applications, notably as a promising aid to cancer delineation in breast[174], liver[175] and gastrointestinal tract[176]. With relatively low-cost instrumentation and maneuverability, DRS technique not only offers non-contact to minimally invasive, usually point-based interrogation of tissues of interest based on their wavelength dependent absorption and scattering properties, but also permits a greater flexibility of signal processing due to the abundant information embedded in the spectral data. As a result, there has been a growing interest in exploiting machine learning (ML) algorithms for tissue classification or physiological parameter extraction using DRS data[179,215–217], while another conventional approach predominantly relies on comparing extrapolated optical properties, commonly absorption and reduced scattering coefficients, for tissue differentiation using spectroscopic measurements combined with layered Monte Carlo simulation[163,218,219]. However, many challenges can be seen with deploying ML techniques in spectral data, because modern spectroscopy measures a multitude of wavelength features with widely known properties of multicollinearity, redundancy and noise that not only affect the accuracy performance due to overfitting of the training data, but also deteriorate interpretability and explainability of the ML model[220]. Feature selection (FS), namely to select a subset of wavelengths that best approaches

the classification or regression problem, becomes crucial for understanding the knowledge space, reducing data dimensionality and thereby instrument complexity, as well as finding accurate ML models in the context. There has been considerable research into wavelength selection in spectroscopy[189,221–223] as well as generic FS algorithms[224–227], for which novel approaches have been proposed to process spectral data. For example, a previous study by R. Gunaratne et al.[193] used multiclass Fisher's linear discriminant analysis to both select features and classify tissue types in ovine joint tissue samples for orthopedic applications, and achieved 100% accuracy with full DRS data of 2048 wavelengths from 190 – 1081 nm, 90% with the selected 10 wavelengths, and 70% with the selected single wavelength. F. Fanjul-Vélez et al.[216] examined the use of spectral characteristics extraction and PCA as a dimensionality reduction technique on DRS measurements collected from *ex vivo* porcine specimens, which demonstrated promising specificity and sensitivity values of greater than 98%. Another application of FS included the study by M. Mamouei et al.[228], where the group compared different variations of PLS techniques with a genetic algorithm for optimization to identify important spectral regions that could represent lactate concentrations in blood using optical sensing, and achieved higher accuracy scores with a reduced number of wavelengths.

In this work, we present four distinct FS frameworks that can be utilized to methodologically select a subset of wavelengths from original DRS measurements, where comparable classification accuracy scores can be computed from the selected subset or the full set of features to differentiate tissue types encountered in bone-related surgeries. The FS frameworks have been developed by investigating DRS measurements via the process of Knowledge Discovery in Databases (KDD), which consists of understanding the knowledge domain, defining research goals, creating dataset, and multiple iterations of data preparation, data mining and pattern interpretation[229–231]. The focus is on discovering this feature subset from the original DRS data domain via tailored FS frameworks, and the selected features will be implemented as the wavelength(s) of light source in the optical device to guide bone cement removal as a means of reducing instrument complexity in the next stage. As such, the primary aims are thereby defined as the following: 1) Exploring domain knowledge using the KDD process in the space of DRS relating to the field of orthopedics; 2) Subsequently determining an optimal subset of DRS wavelengths that can provide sufficient discriminative power between tissue types by comparing different FS algorithms; and 3) Developing a suitable wavelength selection methodology that allows for straightforward adaptation to a wider range of clinical scenarios.

3.3 Materials and Methods

All *ex vivo* measurements were approved by and in compliance with the regulations at Tyndall National Institute, Cork, Ireland. The term "wavelength", namely the spectral increment defined by the spectrometer, is referred to as "feature" (name of the wavelength feature) in this section to suit the context. The term "sample" in the context of FS refers to each DRS spectral data entry. All data preprocessing and analysis were implemented in the Python Programming Language Version 3.9 (Python Software Foundation, https://www.python.org/) built from open-source libraries, packages and dependencies including scikit-learn[232], SciPy[233] and SHAP[234,235].

3.3.1 Specimen Preparation and DRS Data Acquisition

The *ex vivo* ovine tissue specimens included bone marrow, cartilage, cortical bone, muscle, and trabecular bone sourced from a local butcher shop, which were sacrificed two days prior to delivery and immediately refrigerated in plastic bags until two hours prior to measurements. All measurements were acquired at room temperature, where tissue specimens were kept moist using saline spray. As described before, muscle specimens were approximately 22×23×8 cm in Fig. 3.3.1a; femoral specimens were approximately 23-cm long and 3-cm in diameter with cortical bone layer of approximately 5 mm in Fig. 3.3.1b; and bone cement (PALACOS® R+G pro, Heraeus Medical GmbH, Wehrheim, Germany) specimens were cured and hand-molded into approximately 6×5×4-cm blocks in Fig. 3.3.1c one day prior to experiments. All tissue specimens were unprocessed to imitate natural conditions and measured freshly upon delivery. DRS measurements of multiple unique locations were collected from one specimen with at least 5 mm apart in all four directions. The class label of cortical bone consisted of DRS measurements collected from both the outside and the inside of the femoral column, where the outside measurements were made with bone marrow in the femur and the inside measurements were made with muscle specimens layered underneath and bone marrow removed. The total number of tissue specimens and DRS measurements are summarized in Table 3.3.1.

Table 3.3.1 The total number of tissue specimens and DRS measurements used in the analysis.

	Bone Marrow	Cartilage	Cortical Bone	Muscle	Trabecular Bone	Bone Cement
Number of Specimens	43	55	48	31	47	3
Number of Data Entries	1000	1000	1000	1000	1000	215

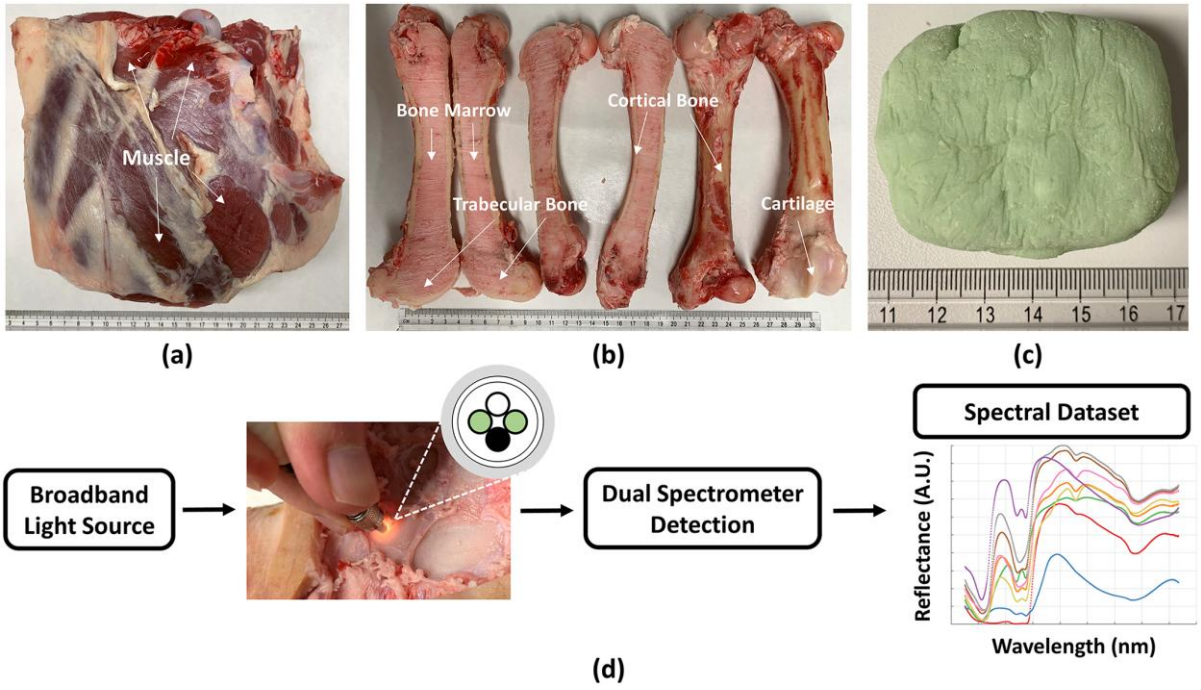


Figure 3.3.1 *Ex vivo* ovine tissue samples including (a) muscle mass; (b) femur containing bone marrow, cartilage, cortical bone and trabecular bone; and (c) bone cement sample. The EWDRS system in (d) shows the experimental setup, where the fiber optic probe, connected to a broadband light source and two spectrometers, was in contact with one tissue specimen. White circle: fiber channel to light source; green circles: fiber channels to spectrometers; black circle: not in use.

Briefly, the DRS system employed a dual spectrometer detection configuration across the ultraviolet A, visible, near-infrared and short-wave infrared (UVA/VIS/NIR/SWIR) spectral range, known as extended-wavelength DRS (EWDRS). The 355 to 1100 -nm and 1100 to 1850 -nm ranges were measured by QE Pro spectrometer (Ocean Insight B.V., Duiven, The Netherlands) and NIR Quest spectrometer (Ocean Insight B.V., Duiven, The Netherlands), respectively, with a tungsten-halogen broadband light source (HL-2000-HP, Ocean Insight

B.V., Duiven, The Netherlands) of emission from 350 – 2400 nm. The two spectrometers were set to acquire five repeats consecutively during one acquisition of 2 s for a single measurement location. The fiber optic probe was a 1-to-4 fan-out bundle with equidistant source-detector separations of 0.63 mm (BF46LS01, 600-µm core, Low OH, Thorlabs, Munich, Germany), of which only three fiber channels were used. A schematic depiction of the EWDRS system setup is shown in Fig. 3.3.1d.

3.3.2 Data Preprocessing

Each EWDRS data entry was obtained by firstly averaging over the five repeats followed by calibration, and secondly splicing the two spectra together using spline interpolation. Wavelength increments of the spectrometers were approximately 0.76 nm in the 355 to 1100 -nm range and approximately 1.6 nm in the 1100 to 1850 -nm range. All EWDRS measurements were calibrated against a reflectance standard (FWS-99-01c, Avian Technologies LLC, New London, USA) and corrected for dark counts pre and post each experiment using the standard method $\frac{S_{raw}-S_{bkgd}}{S_{ref}-S_{bkgd}}$. Savitzky-Golay (SG) filter, based on local least-squares polynomial approximation, was applied with a frame size of 5 and polynomial order of 2 to denoise the spectral data[236,237]. The EWDRS dataset, containing numerical features and categorical labels, was structured into an $m \times n$ matrix, where m represents the number of DRS data entries and n represents the number of features. There were 5215 DRS data entries and 1531 features in total subjected to further analysis, where the DRS data entries were treated as non-correlated and mutually independent entities.

3.3.3 Classification Models

Classification models were trained via the One-vs-Rest (OvR) binary approaches. The positive class (one) was defined as *bone cement*, and the negative class (rest) was collectively defined for *bone marrow*, *cartilage*, *cortical bone* and *trabecular bone* in the first scenario (*boneCement vs. rest*). In the second scenario, the positive class was *cortical bone*, and the rest included *bone marrow*, *cartilage*, *muscle* and *trabecular bone* (*cortBone vs. rest*). Six models were included to compute balanced accuracy using all features:

- logistic regression (LogReg) representing a baseline linear regression model used for classification,
- linear discriminant analysis (LDA) representing a baseline linear classification model,

- random forest (RF) representing an ensemble bagging classifier,
- k-nearest neighbors (KNN) representing an instance-based classifier,
- Gaussian Naïve Bayes (GNB) representing a probabilistic classifier, and
- support vector machine (SVM) representing a maximum margin classifier.

The balanced accuracy is equivalent to the arithmetic mean of sensitivity and specificity in binary classification (Eqn. 3.3.1),

$$\boldsymbol{balanced\ accuracy} = \frac{\mathbf{1}}{\mathbf{2}}\left(\frac{\boldsymbol{TP}}{\boldsymbol{TP+FN}} + \frac{\boldsymbol{TN}}{\boldsymbol{TN+FP}}\right), \qquad \textbf{(Equation 3.3.1)}$$

where TP is the true positive, TN is the true negative, FP is the false positive and FN is the false negative. For example, in the first scenario TP and TN represent the instances where bone cement and the rest are correctly identified, respectively. Default parameters implemented in scikit-learn library were used. The learning model that generated the highest balanced accuracy was subsequently chosen as the classifier to evaluate the quality of FS. Balanced accuracy was treated as a metric for quality check, where features of lower scores were discarded. Globally, the percentage of holdout dataset (test dataset) was stratified 20%, which was split out of the entire dataset prior to analysis. Global cross-validation (CV) setting was chosen to be stratified 10-fold for 10 repeats. Stratified sampling was used to preserve the same class distribution of features in the training, validation and holdout datasets as the complete dataset. The six learning models were trained, validated and then tested using the entire original EWDRS data.

3.3.4 Decision Tree Classifier – One Feature Classification

Single decision tree classifiers were trained with CV to compute balanced accuracy iteratively using only one feature at a time. Balanced accuracy of independent single features was obtained across the full spectral range for the entire dataset to indicate potential spectral ranges of high discriminative strength. The maximum depth of the tree was set to 2, and other parameters were set to default.

3.3.5 Feature Selection

Feature selection (FS) techniques were implemented via the OVR binary approach for the goal of achieving the highest discriminative power. An overview of FS process is shown in Fig. 3.3.2, which typically includes candidate feature subset generation from the original dataset

through user-defined search strategies, candidate subset evaluation through user-defined inclusion criteria, and model fitting of the training and testing datasets to assess performance. The final selection subset was pre-defined to contain 10 features. The following subsections first described the implementation of principal component analysis (PCA), LDA, and backward interval partial least squares (biPLS) into independent FS frameworks. The three algorithms have been chosen because they are frequently used in spectroscopic data analysis. Mathematical descriptions of these techniques are therefore not included here in depth; and sophisticated programming algorithms can be found in scikit-learn library[232]. More detailed explanations can also be found in review articles[238–241]. Subsequently, an ensemble framework of FS[242] was formulated to compare with FS frameworks using PCA, LDA and biPLS in a discovery-oriented data selection workflow.

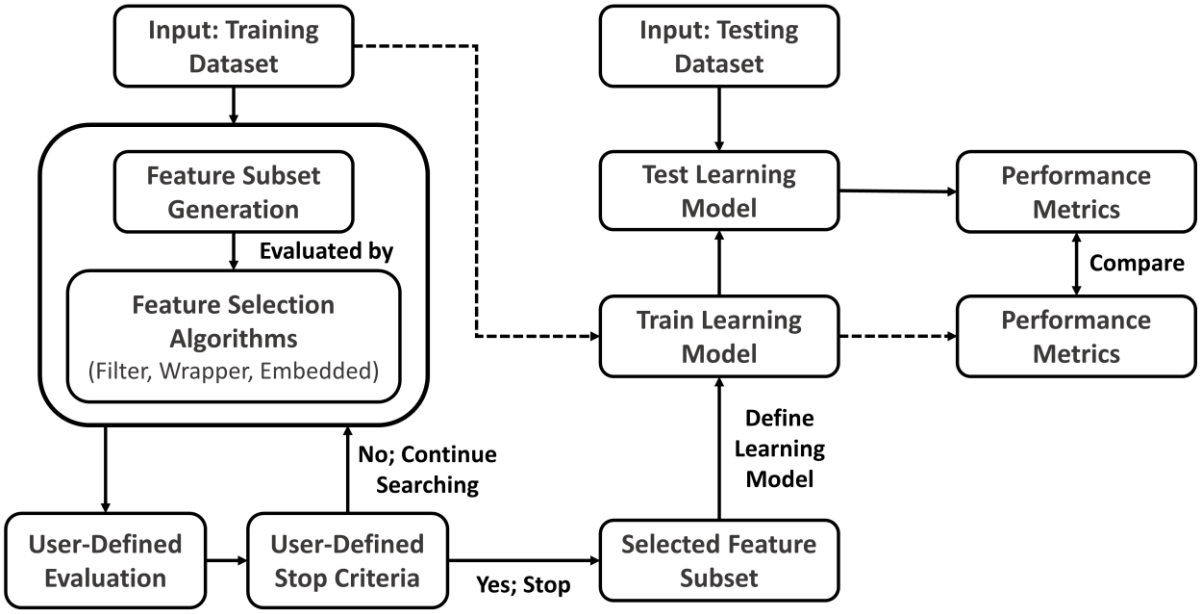


Figure 3.3.2 Overview of a typical feature selection (FS) workflow.

3.3.5.1 Feature selection framework – principal component analysis

Principal component analysis (PCA) is an unsupervised dimensionality reduction technique, or feature extraction process, that projects the original data based on maximized variance onto a lower dimension via an orthogonal linear transformation. The resulted principal components (PCs) from PCA transformation, ranked by the calculated variance in descending order, might not bear discriminative power in the same descending order for the classification problem[243]. A stochastic optimization algorithm, specifically simulated annealing (SA)[244], was therefore implemented to search for a set of PCs that approximated the global optimum of a user-defined

cost function. LDA was selected as the cost function due to its simplicity to calculate classification accuracy for optimization. Regularization parameters in SA were tuned by trial and error to suit the data domain. To minimize computational cost, the first 30 out of 1530 PCs were initially selected from the PCA transformation followed by SA optimization with 600 iterations to select 10 of the 30 PCs that jointly produced the highest LDA classification accuracy. SA optimization would be inactivated if the 10 randomly selected PCs generated a 100% accuracy score during the first iteration. The selected 10 PCs represented greater than 98% of total explained variance. The next step involved selecting peaks from the 10 PCA eigenvectors plotted against features (wavelengths) based on user-defined inclusion criteria, which comprised of removal of duplicates, features within 20 nm horizontally, features below scaled 20% vertically. Lastly, the final 10 features were determined by ranking and removing collinearity, that was, identifying the most relevant feature to the class label by ranked ANOVA F-values, and sequentially discarding the feature that was the most correlated with the most relevant feature based on Pearson correlation coefficients. The flowchart of PCA FS framework can be found in Fig. 3.3.3.

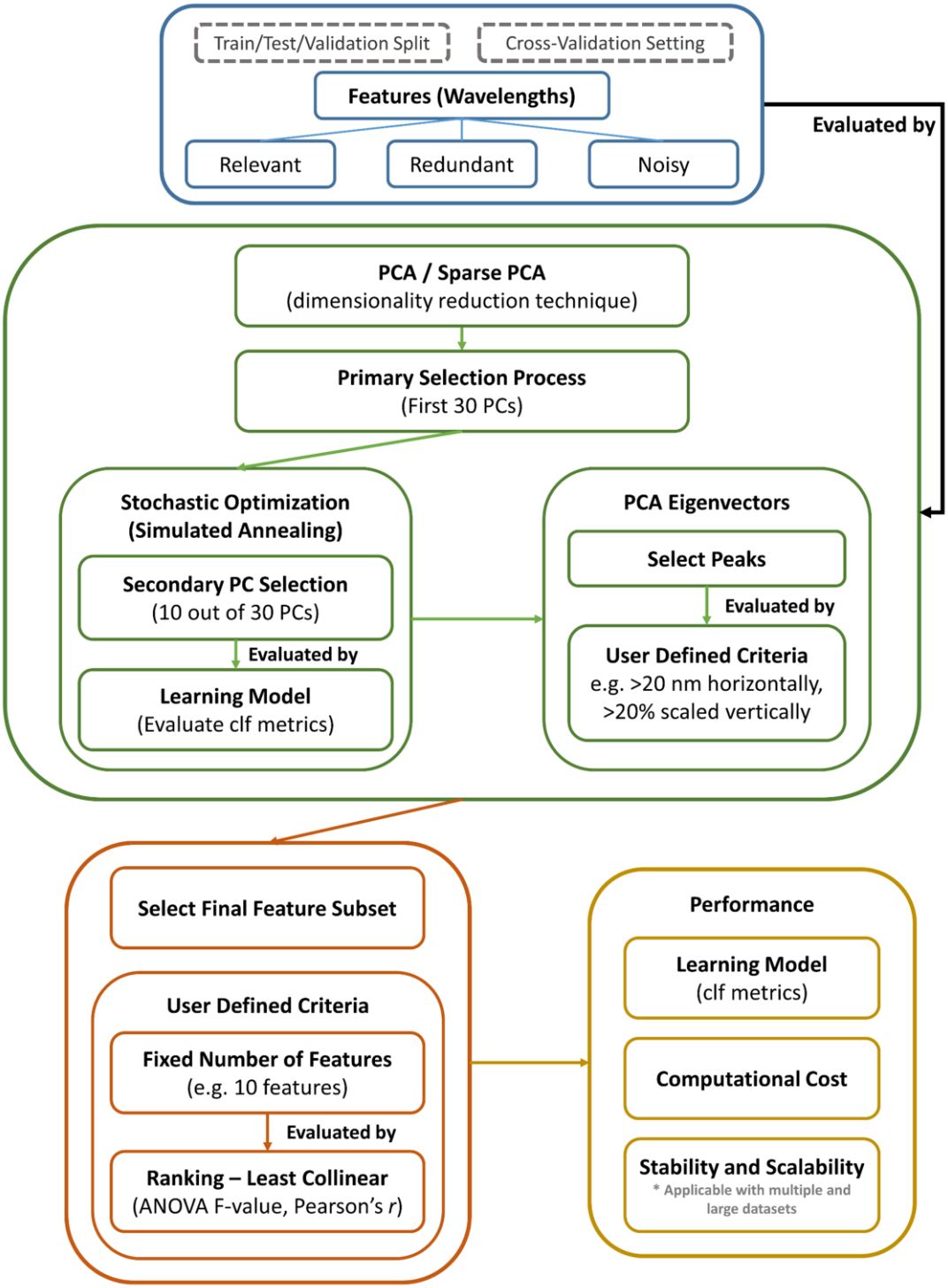


Figure 3.3.3 FS framework implementing PCA/Sparse PCA to process the EWDRS dataset. Acronyms: FS for feature selection; PCA for principal component analysis; PC for principal component; EWDRS for extended-wavelength diffuse reflectance spectroscopy.

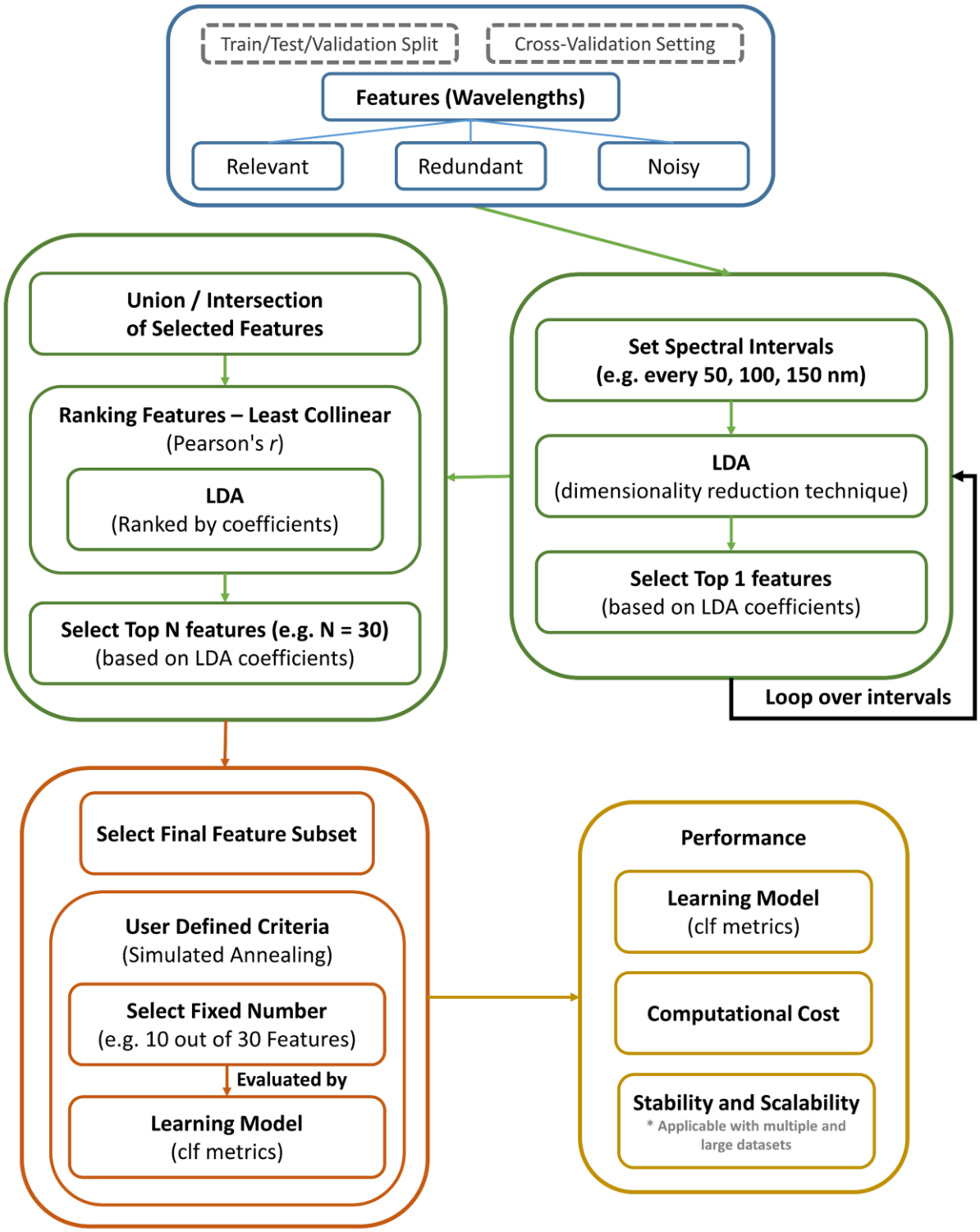


Figure 3.3.4 FS framework implementing LDA to process the EWDRS dataset. Acronyms: FS for feature selection; LDA for linear discriminant analysis; EWDRS for extended-wavelength diffuse reflectance spectroscopy.

3.3.5.2 Feature selection framework – linear discriminant analysis

Linear discriminant analysis (LDA) is a supervised technique that searches for a linear combination of features based on maximized class separation. It can be used as a linear predictive model for binary or multiclass classification as well as a dimensionality reduction technique. To implement LDA in a FS workflow, a moving-window approach was utilized by setting a series of feature intervals. Seven intervals of custom lengths were used, which were 25, 50, 75, 100, 150, 200, 300 nm. The initial feature subspace was constructed by selecting the top feature within the one interval based on the ranked LDA coefficients of this interval, for which the computation process was iterated over all interval sizes and across the full feature domain. Duplicates and features within 30 nm of each other were discarded. Then 75% of the initial feature subspace was chosen similarly by sequential removal of ranked feature collinearity, where the most relevant feature to the class label was instead determined by ranking LDA coefficients of the initial feature subspace using the original dataset. The final feature subset was calculated by performing SA optimization to search for the 10 features whose joint produced the highest LDA classification accuracy. SA optimization was always activated, and the number of iterations was set to 2000 to reach convergence. The flowchart of LDA FS framework can be found in Fig. 3.3.4.

3.3.5.3 Feature selection framework – backward interval partial least squares

Backward variable elimination partial least squares (PLS) is one of the many PLS method variations in FS to which backward interval PLS (biPLS) belongs. The basis is to compare the PLS root mean square error of cross-validation (RMSECV) of the N-1 intervals with the baseline RMSECV, and eliminate the feature interval whose removal yields the lowest RMSECV in a recursive way[245]. The baseline RMSECV was calculated using all features. Optimization of PLS components was performed for each PLS regression with 30 total components allowed to minimize computation. RMSECV calculation was iterated over the number of intervals, the size of intervals and the different shuffles of the training dataset for CV across the full feature domain. The custom sizes of feature intervals included 20, 40, 60, 70, 80 and 95 nm. Five different shuffles of the training dataset for CV were generated randomly and kept consistent for all biPLS FS analyses. The retained feature intervals from each iteration received a +1 vote. The features with the highest votes were deemed important. The final feature set was determined by searching the top 10 least collinear features, and the

most relevant feature to the class label was calculated by ranked PLS-Variable Importance in Prediction (PLS-VIP) scores[246]. The flowchart of biPLS FS framework can be found in Fig. 3.3.5.

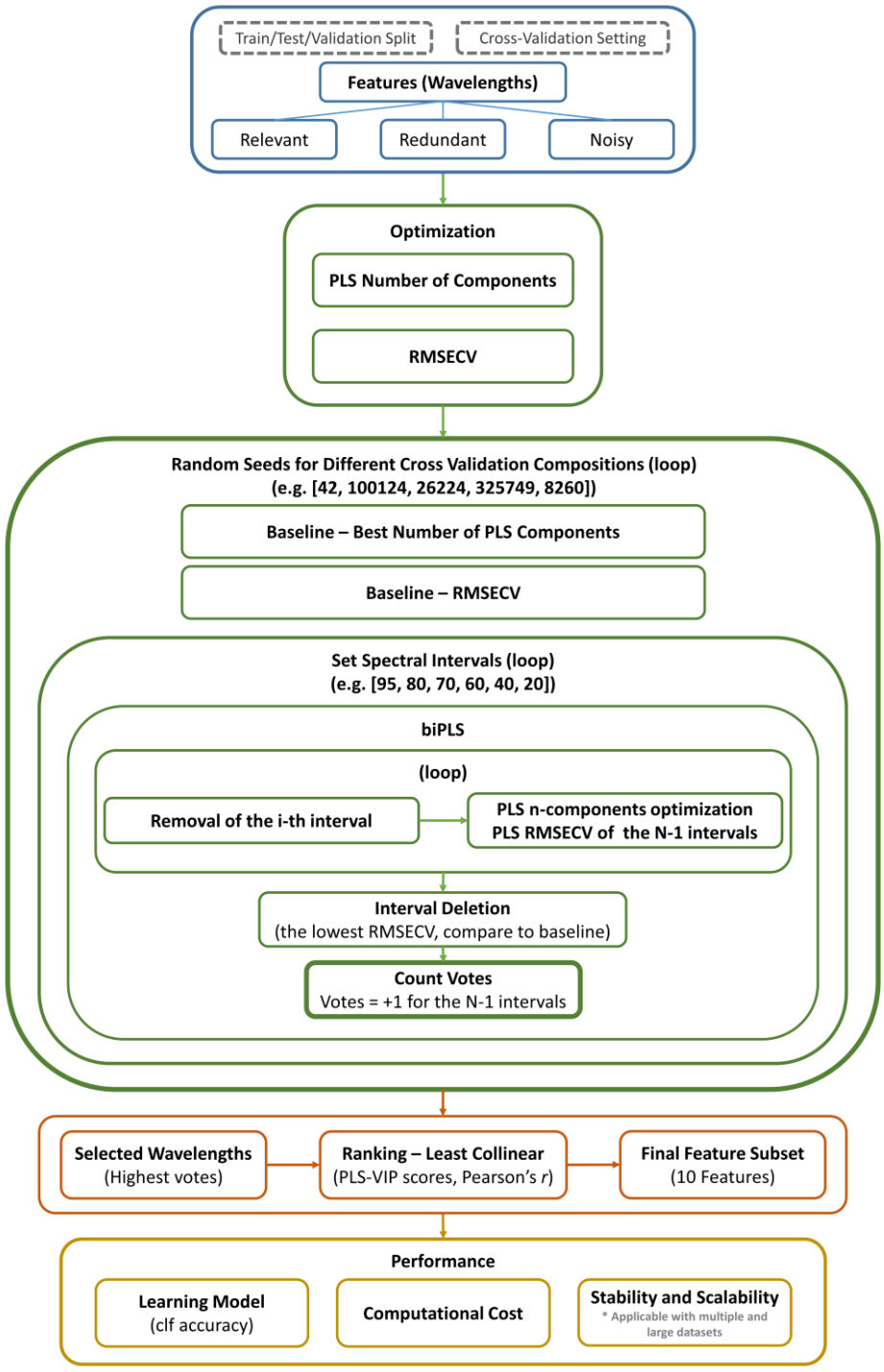


Figure 3.3.5 biPLS FS framework showing the workflow to process EWDRS dataset. Acronyms: biPLS for backward interval partial least squares; FS for feature selection; EWDRS for extended-wavelength diffuse reflectance spectroscopy; PLS for partial least squares; PLS-VIP for PLS-Variable Importance in Prediction; RMSECV for root mean square error of cross-validation; clf for classification.

3.3.5.4 Feature selection framework – ensemble

Ensemble feature selection (EFS) is a learning framework that principally combines different individual feature selection algorithms, namely filter, wrapper or embedded methods, to achieve improved outcomes by avoiding bias, merging advantages and compensating disadvantages of individual FS methods. The EFS framework in this study incorporated three univariate filtering methods, which were Maximum Relevance – Minimum Redundancy (mRMR)[247] that measures the most correlation with a class, Mutual Information (MI)[248] that measures the amount of information gain of one variable (feature) given the other known variable (class label), and ReliefF[249,250] that measures conditional dependencies between the k-nearest neighbors of one feature in an instance-based manner. Selected features from the union of outputs by mRMR, MI and ReliefF were input into Boruta-RF[251,252], which is a wrapper method around RF that utilizes shadow features to compute feature importance. The final feature subset could be determined by 1) selecting the top 10 features from Boruta-RF rank based on the ranked ANOVA F-values, resulting in a narrow spectral band (Ensemble SB), or 2) selecting the top 10 least collinear features out of the Boruta-RF rank, which was computed via the same collinearity removal process in the PCA FS framework (Ensemble LC). SHAP (SHapley Additive exPlanations)[253–258], one of the state-of-the-art tools in ML explainability, was performed to explain and quantify contributions of individual selected features to model prediction base on cooperative game theory. The SHAP value was proposed by Lundberg and Lee as a unified measure to represent additive feature importance, which was the average outcomes of marginal contributions from individual features over all possible feature permutations[259]. The SHAP algorithm used in the EFS framework was based on ensembles of trees. There were two optional optimization steps in the EFS framework including partition of the training dataset and aggregation of the final selection. In particular, partition involved segmenting the training dataset into multiple packets vertically by features or horizontally by samples, or both[260], and aggregation involved searching features from all vertical partitions to form a final subset that produced an optimal outcome based on user-defined criteria. Decisions were usually made by prior domain knowledge combined with the study objective. In the EFS framework, only vertical partition by features was adopted to divide the training dataset into three spectral ranges, which were approximately the VIS range of 355 – 700 nm, the NIR range of 700 – 1000 nm and the SWIR range of 1000 – 1850 nm. Horizontal partition was indirectly performed by iterating over different compositions of CV. Aggregation was achieved by incrementally adjoining the VIS, NIR and SWIR ranges, resulting in the VIS range of 355 –

700 nm, the VIS/NIR range of 355 – 1000 and the VIS/NIR/SWIR range of 355 – 1850 nm. The flowchart of EFS framework is shown in Fig. 3.3.6.

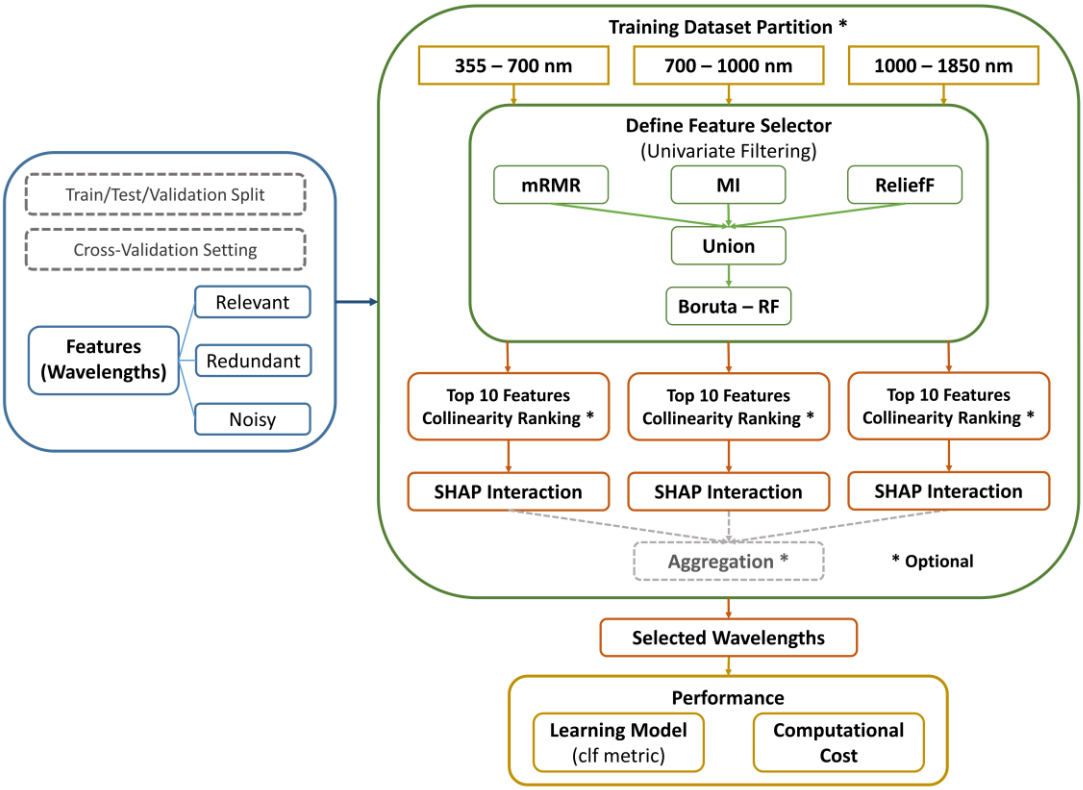


Figure 3.3.6 Ensemble feature selection (EFS) framework. Optional steps are labelled with asterisks, including training dataset partition, sequential removal of collinear features by ranking and aggregation of results from all partitions. Acronyms: mRMR for Maximum Relevance – Minimum Redundancy; MI for Mutual Information; Boruta – RF for Boruta – Random Forest; SHAP for SHapley Additive exPlanations; clf for classification.

3.4 Results

The classification models were benchmarked on the complete dataset as a reference of the achievable maximal accuracy, followed by performance comparison of the top 1 and 10 wavelength features selected by the four FS frameworks. Further investigations examined FS in different spectral ranges and the tradeoff between the number of selected features versus model accuracy. Model explainability was explored to understand individual feature contributions to classification prediction.

3.4.1 Classification Models

The six classification models were trained with CV on the train/validation and tested on the holdout datasets containing all features (Table 3.4.1). Two decimal places were retained for balanced accuracy. LDA was subsequently used to assess the quality of FS due to outperformance.

Table 3.4.1 Summary of the balanced accuracy scores on the holdout dataset generated by logistic regression (LogReg), linear discriminant analysis (LDA), random forest (RF), k-nearest neighbors (KNN), Gaussian Naïve Bayes (GNB) and support vector machine (SVM), and the average computation time to train one model.

Classifier	**Balanced Accuracy (%)**		**Computation Time (s)**
	boneCement vs. rest	***cortBone vs. rest***	
LogReg	100	95.68 ± 1.38	0.25
LDA	100	99.79 ± 0.33	1.4
RF	99.98 ± 0.05	97.70 ± 1.14	2.0
KNN	100	96.37 ± 1.32	0.21
GNB	99.98 ± 0.05	87.49 ± 1.75	0.12
SVM	100	95.48 ± 1.34	0.64

3.4.2 One Feature Classification Using Decision Tree

The balanced accuracy scores computed by one feature classification using decision tree classifiers plotted against wavelength features are shown in Fig. 3.4.1. Independent features that bore discriminative power between the binary classes were illustrated; for instance, results for bone cement as the positive class demonstrated high balanced accuracy scores in the 500 to 600 -nm range and beyond 700 nm, while improved balanced accuracy for cortical bone as the positive class were found around 1210 nm and in the 1450 to 1600 -nm range. One single decision tree classifier required approximately 8.5×10^{-3} s training time on average.

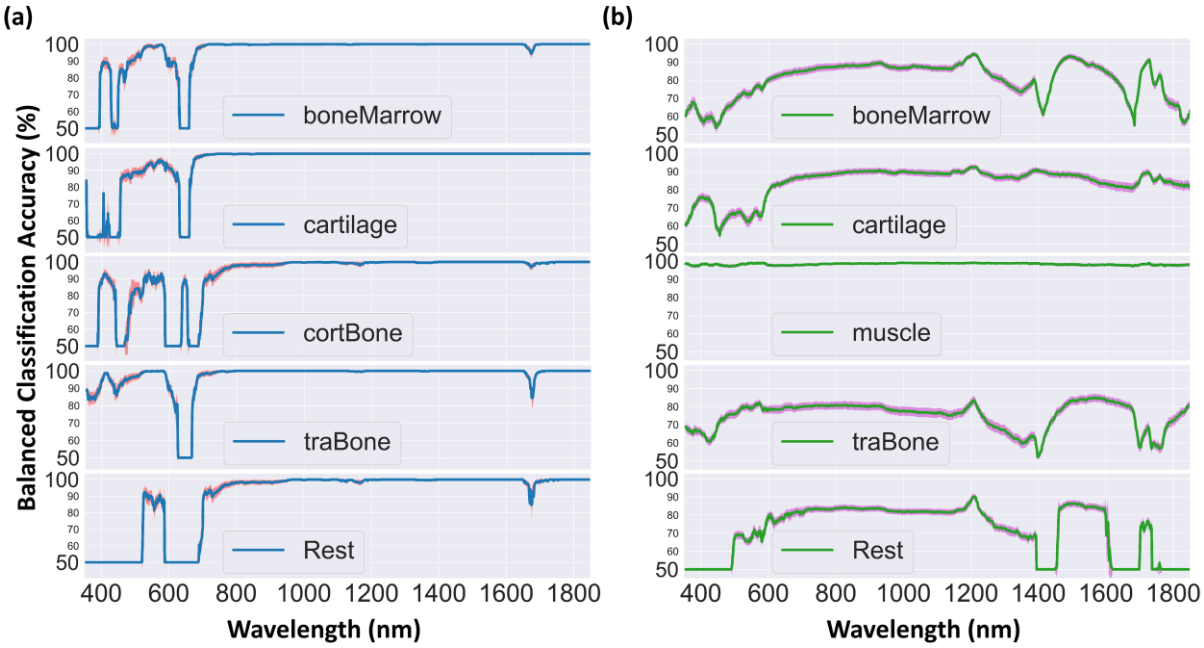


Figure 3.4.1 Balanced accuracy using one feature (wavelength) computed by decision tree classifiers plotted against wavelength features, for (a) bone cement vs. bone marrow, cartilage, cortical bone, trabecular bone, or the rest, respectively; (b) cortical bone vs. bone marrow, cartilage, muscle, trabecular bone, or the rest from top to bottom, respectively. Standard deviations are shown in shaded error bands. Acronyms: boneMarrow for bone marrow; cortBone for cortical bone; traBone for trabecular bone.

3.4.3 PCA, LDA, and biPLS Feature Selection Frameworks

The final 10 selected wavelength features from FS frameworks of PCA, LDA and biPLS overlaid on the SG smoothed original EWDRS spectra for *boneCement vs. rest* and *cortBone vs. rest* are shown in Fig. 3.4.2. As shown in Table 3.4.2 (Top), the final feature subset selected by the PCA FS framework jointly yielded balanced accuracy scores of 100% (train/validation) and 100% (holdout), 96.21 ± 1.39% (train/validation) and 94.78 ± 3.47% (holdout) for *boneCement vs. rest*, and *cortBone vs. rest*, respectively. The time required for one iteration of the PCA FS framework to complete was 0.64 and 21 min for bone cement and cortical bone as the positive class, respectively. SA optimization was only activated for *cortBone vs. rest*, which required longer time for the framework to complete. For LDA FS framework, the balanced classification accuracy scores were 100% (train/validation) and 100% (holdout), 98.41 ± 0.82% (train/validation) and 98.16 ± 2.02% (holdout) requiring approximately 0.16 and 1.1 min to complete for *boneCement vs. rest*, and *cortBone vs. rest*, respectively. For biPLS FS framework, the balanced accuracy scores were 100% (train/validation) and 100% (holdout), 96.12 ± 1.39% (train/validation) and 95.80 ± 3.04% (holdout) requiring approximately 6.3 and

7.4 days to complete for *boneCement vs. rest*, and *cortBone vs. rest*, respectively. The most relevant features to the classification problem in the data domain are summarized in Table 3.4.2 (Top) for the PCA, LDA and biPLS FS frameworks.

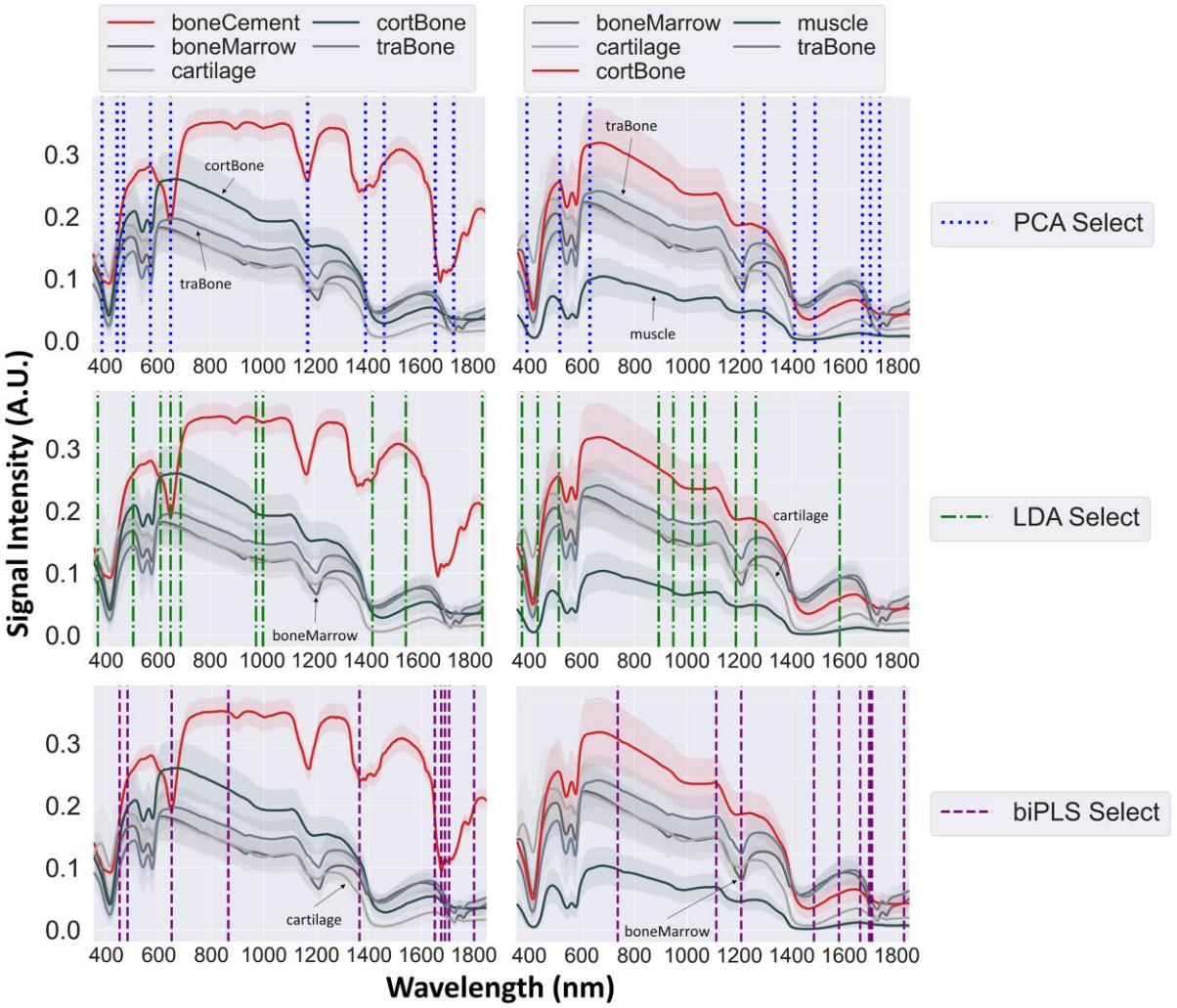


Fig. 3.4.2 The final 10 selected features from FS frameworks of PCA (top), LDA (middle) and biPLS (bottom) on the EWDRS spectra for *boneCement vs. rest* (left) and *cortBone vs. rest* (right). Standard deviations are shown in shaded error bands. The arrows highlight spectra of different class labels in subfigures for each scenario. Acronyms: boneCement for bone cement; boneMarrow for bone marrow; cortBone for cortical bone; traBone for trabecular bone; PCA for principal component analysis; LDA for linear discriminant analysis; biPLS for backward interval partial least squares.

Table 3.4.2 Summary of the balanced accuracy scores using the top 1 and 10 wavelength features generated from PCA, LDA, biPLS and EFS frameworks for *boneCement vs. rest* and *cortBone vs. rest*, the averaged computation time for one entire framework (top), and the scores generated by EFS framework on the holdout dataset in the VIS and VIS/NIR ranges (bottom). Accuracy using the top 1 wavelength was not applicable for Ensemble SB. Acronyms: PCA for principal component analysis; LDA for linear discriminant analysis; biPLS for backward interval partial least squares; SB for Spectral Band; LC for Least Collinear.

(Top)		*boneCement vs. rest*					*cortBone vs. rest*				
FS Framework Balanced Accuracy (%)		PCA	LDA	biPLS	Ensemble *VIS/NIR/SWIR*		PCA	LDA	biPLS	Ensemble *VIS/NIR/SWIR*	
					SB	LC				SB	LC
Top 1 Wavelength	Train/ Validation	100	100	99.98 ± 0.05	100	100	88.06 ± 2.15	84.98 ± 2.23	88.09 ± 2.15	N/A	88.13 ± 2.16
	Holdout	100	100	100	100	100	87.31 ± 3.91	83.69 ± 4.81	87.36 ± 3.90	N/A	87.36 ± 3.89
	Top Feature	1463	1424	1801	1457	1458	1211	1188	1207	1208	1209
Top 10 Wavelengths	Train/ Validation	100	100	100	100	100	96.21 ± 1.39	98.41 ± 0.82	96.12 ± 1.39	95.24 ± 1.48	96.56 ± 1.27
	Holdout	100	100	100	100	100	94.78 ± 3.47	98.16 ± 2.02	95.80 ± 3.04	93.74 ± 3.24	95.77 ± 3.16
Computation Time (min)		0.64	0.16	9072	4.6	4.6	21	1.1	10656	4.6	4.6

(Bottom)	*boneCement vs. rest*				*cortBone vs. rest*			
FS Framework Balanced Accuracy (%)	Ensemble *VIS/NIR*		Ensemble *VIS*		Ensemble *VIS/NIR*		Ensemble *VIS*	
	SB	LC	SB	LC	SB	LC	SB	LC
Holdout	99.94 ± 0.19	100	98.99 ± 0.77	100	92.07 ± 3.44	93.38 ± 3.36%	86.84 ± 3.90	91.95 ± 4.09
Top Feature	990	956	555	576	925	927	695	699

3.4.4 Ensemble Framework of Feature Selection

The final selection of 10 wavelength features overlaid on the SG smoothed original EWDRS in the VIS, VIS/NIR and VIS/NIR/SWIR ranges are shown in Fig. 3.4.3. For *boneCement vs. rest* and *cortBone vs. rest*, the selected spectral bands were centered around 555 and 695 nm in

the VIS range achieving 98.99 ± 0.77% and 86.84 ± 3.90%, 990 and 925 nm in the VIS/NIR range achieving 99.94 ± 0.19% and 92.07 ± 3.44%, and 1460 and 1200 nm in the VIS/NIR/SWIR range achieving 100% and 93.74 ± 3.24% balanced accuracy scores; the least collinear features collectively reached 100% and 91.95 ± 4.09 % in the VIS range, 100% and 93.38 ± 3.36% in the VIS/NIR range, and 100% and 95.77 ± 3.16 % in the VIS/NIR/SWIR range, respectively, on the holdout dataset as shown in Table 3.4.2 (Top and Bottom). Optimal performance was discovered from using Ensemble LC and biPLS FS frameworks based on the high averaged accuracy over the two holdout sets for the top 1 and 10 features. The latter framework, however, required excessive computational effort. The final subset generated by Ensemble SB collectively yielded a narrow spectral band, making its deployment comparable to using the top feature.

Fig. 3.4.4 (a-c) demonstrated the top 10 least collinear features on the x-axis ranked by contribution to class prediction for *boneCement vs. rest* (top) and *cortBone vs. rest* (bottom), as well as the balanced accuracy calculated using sequential inclusion of the ranked wavelength features. The accuracy scores reached the first plateau after including approximately 3-4 wavelength features. Distribution of individual feature contributions on the prediction calculated by SHAP values is shown in Fig. 3.4.4 (d-e), where the vertical axis illustrated the 10 features ranked in descending order of contribution and the SHAP value on the horizontal axis explained the association between the individual feature values and the level of their impact on the target prediction. The SHAP beeswarm summary plot visualized contributions from all instances determined by SHAP values on each feature row, which included 4215 and 5000 single dots for *boneCement vs. rest* and *cortBone vs. rest*, respectively. The red and blue indicated high and low feature values, which corresponded to high and low measurements of the original DRS signal intensity, respectively. Positive and negative SHAP values represented positive and negative contribution by the exact amount in log odds as additive feature importance to the binary model output [0, 1], respectively. For example, an instance of 0.2, as quantified in SHAP value, indicated 0.2 additive feature importance. The 1458 and 1209 -nm features had the strongest effect on whether the prediction was bone cement and cortical bone in the two scenarios, respectively. For *boneCement vs. rest*, the model prediction was overall more likely to be bone cement when the DRS signal intensity increased for all of the 10 wavelength features. This was reflected by the spectra in Fig. 3.4.3b, where the signal intensity of DRS measurements for bone cement was higher than those of biological tissues at the selected wavelengths. For *cortBone vs. rest*, although the distribution of SHAP values on each

feature row was more continuous, similar observations could be made and reflected by Fig. 3.4.3(d). Specifically, a positive correlation was illustrated at wavelength features including 1209 and 900 nm whereas wavelengths such as 1629 and 1850 nm displayed an inverse correlation with DRS signal intensity. In addition, one iteration of the EFS framework required approximately 4.6 min until completion on average.

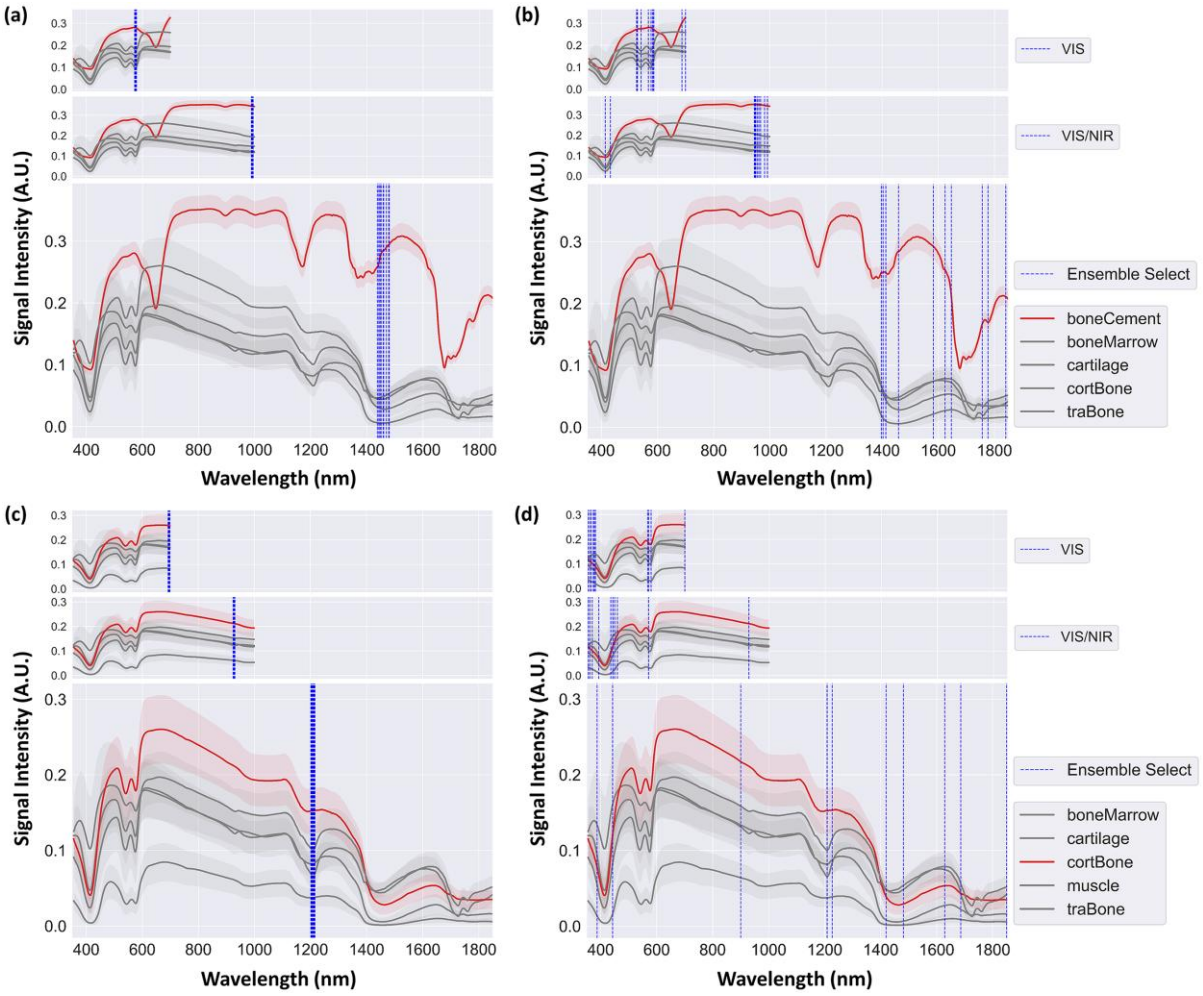


Figure 3.4.3 Savitzky-Golay (SG) smoothed original extended-wavelength DRS (EWDRS) spectra overlaid with the final 10 selected wavelength features as (a, c) spectral band and (b, d) the top least collinear features for *boneCement vs. rest* and *cortBone vs. rest* in the VIS (top), VIS/NIR (middle), and VIS/NIR/SWIR (bottom) spectral ranges, respectively. Standard deviations are shown in shaded error bands. Acronyms: boneCement for bone cement; boneMarrow for bone marrow; cortBone for cortical bone; traBone for trabecular bone.

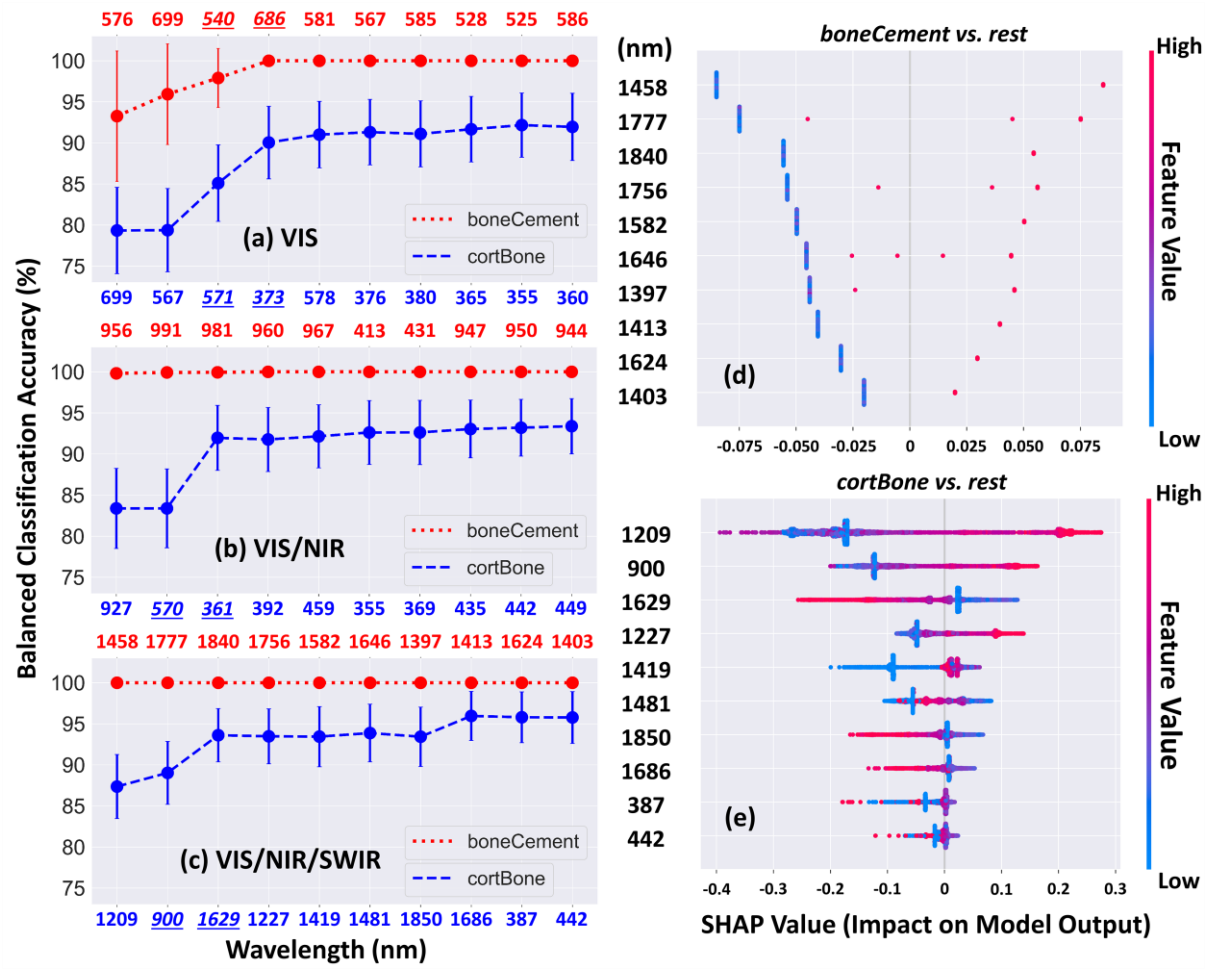


Figure 3.4.4 Balanced accuracy computed by LDA with CV plotted against sequential inclusion of the ranked least collinear wavelength features for *boneCement vs. rest* (top x-axis) and *cortBone vs. rest* (bottom x-axis) in the (a) VIS, (b) VIS/NIR and (c) VIS/NIR/SWIR ranges. The underscored features indicated the two wavelengths approaching the first plateau. Distribution of individual feature contributions on the prediction by SHAP analysis is shown for (d) *boneCement vs. rest* and (e) *cortBone vs. rest*. The 10 features were ranked on the vertical axis in descending order of their contributions to prediction. The horizontal axis illustrates the impact level of individual features of high or low value related to positive or negative prediction. Acronyms: LDA for linear discriminant analysis; CV for cross-validation; SHAP for SHapley Additive exPlanations.

3.5 Discussion

The EWDRS dataset, created by collecting DRS measurements from ovine specimens of tissue types commonly encountered in orthopedics-related surgery, was explored via the KDD process to determine an optimal subset of wavelength features that provided sufficiently high

discriminative power, with the emphasis on identifying the positive class. To achieve this goal, in this work we implemented three conventionally used algorithms in spectroscopy, namely PCA, LDA and PLS, into discovery-orientated FS frameworks, and additionally constructed an EFS framework for comparison to understand domain knowledge and determine an optimal subset of wavelengths with high discriminative power for the positive class.

Each of the four frameworks was designed to not only suit the study goal but also as a complete methodology that could be adapted to changes of class labels and used universally in different clinical scenarios. Disadvantages of individual algorithms were mitigated by implementing optimization techniques. In particular, the analysis aimed to select DRS wavelength features from the original data space that could classify bone cement or cortical bone, because the selected features would be utilized as the potential wavelengths of light source(s) in the subsequent optical instrumentation design to inform cement-to-bone and bone-to-tissue interfaces. This task could be accomplished by deploying an FS framework via solving classification problems. Data transformation would be undesirable and comparison of classification metrics on a transformed data space would generate falsities in our initial assumptions for the investigation. As a result, during data preprocessing, commonly used feature scaling techniques such as standardization and normalization, and spectral scaling techniques such as standard normal variate and multiplicative scatter correction were omitted to maintain the original EWDRS measurements. Algorithms involving data transformation such as PCA, LDA and PLS must be incorporated in a way that could permit FS for classification using the original features. As such, PCA, being unsupervised, was paired with a stochastic optimization technique in a wrapper-based manner to find PCs that jointly bore high discriminative power, on the assumption that 10 PCs could reveal important features in the original data space. The feature exclusion criterion of 20-nm separation was not only to match with the average full width at half maximum (FWHM) of a light-emitting diode (LED), but also to force separation between the selected features and therefore reduce multicollinearity. This was further refined by sequentially ranking and removing features of high correlation to the most relevant one. Another method to lessen computational cost and improve model interpretability for FS is to implement sparse PCA, which is a variant of the original PCA technique that introduces sparsity on the PCA regression coefficients (loadings) and thus retains only the most important features from the transformation[261]. For LDA and PLS, though being supervised, a moving-window approach starting at a narrow interval was employed to firstly ensure all relevant features were captured on the original data dimension;

secondly it helped alleviate the effect of multicollinearity by enforcing wavelength separation via the moving windows and manual deletions of adjacent features. This was an important step because the selected wavelengths needed to be sufficiently distinguishable and represented by light source(s) of sufficiently narrow bandwidths. Multiple iterations over different interval lengths and compositions of CV were also carried out to validate wavelength feature inclusion. In the case of LDA, the algorithm itself looks for maximized class separation, leading to clustered wavelength features in the EWDRS dataset, and therefore manually separating wavelength features yet also satisfying classification requirements were essential in the LDA FS framework to discover other contributors to class prediction in the rest of the spectral regions. For biPLS, although the classification results were comparable with other frameworks, a rigorous protocol using multiple algorithm conditions led to a prolonged evaluation time and was thus suboptimal practically in this case.

Multicollinearity is a well-known property of DRS data for which it offers the advantage of selecting multiple different feature subsets that can achieve similar outcomes for classification problems in spectroscopy, enabling flexibility in hardware design. This behavior was demonstrated by the clusters of the selected features from all four FS frameworks over the same spectral regions, especially the top ranked features. However, the disadvantage is also self-evident such that it deteriorates model interpretability, especially in models that involve data transformation, since the transformed features have lost physical representations thus resulting in less inferential model coefficients. Wavelength features selected by FS frameworks utilizing these coefficients became less representative as the potential wavelengths of light source(s) in hardware. Furthermore, we created the EFS framework comprising of three univariate filters and one tree model in a wrapper-based workflow without involving data transformation. The EFS framework produced another final subset of 10 wavelength features that offered comparable balanced accuracy scores as to using all features, which could be further reduced to only include 3-4 wavelength features since the rest contributed little additional benefits. The EFS was constructed with acceptable computational complexity where the algorithm itself was simple and the computational time was sufficiently fast.

An optimized FS framework for deployment in subsequent development should also be implemented with feature engineering techniques so that collinear features offering similar information will be merged into one new feature, and therefore decrease computational burden and redundant outcomes. The tradeoff between the number of wavelength features and

classification accuracy should also be considered to optimize instrument complexity and cost. In addition to using original DRS data, other conventional methods such as calculations of first and second derivatives could also provide decisive information to aid with FS in spectroscopy.

On the other hand, one feature classification using decision tree classifier can provide insights to understanding the full data domain. This method offered the opportunity to directly illustrate how independent wavelength features contributed to classification. In the case of this EWDRS dataset, the balanced accuracy curves along the full spectral range partially reconstructed the absorption spectra of tissue chromophores, suggesting that the difference of optical absorption between two classes could be a major contributor to the classification prediction and bear sufficient discriminative power. Prominent absorption peaks were identified for tissue biomarkers such as collagen, lipid and water in the SWIR range as well as different forms of hemoglobin (Hb) in the VIS/NIR range. For classification between cortical bone of dense composites versus other softer biological tissues in Fig. 3.4.1b, absorption signatures of lipids at 1210 nm, collagen at 1200, 1500 and 1725 nm, and water at 1440 nm were outlined by higher balanced accuracy with some contribution from Hb at 576 nm[192]. Similarly for classification between bone cement (non-biological) vs. biological specimens, not only the difference between collagen, lipid and water contents played a significant role in the SWIR range but also the region between 500 – 600 representing Hb absorption was recognized. It was essentially the lack of these tissue chromospheres in the non-biological specimens that contributed to the selection of the wavelength features over the region where the biological specimens exhibited stronger absorption and hence lower reflectance, amplifying the difference in signal intensity between the two classes. However, one feature classification evaluates each feature independently, in which assumptions of the method does not rigorously permit the conclusion that joining multiple independent wavelength features can also result in equivalent classification scores. The method itself was intuitive and simple to perform but, with the amount of CV embedded, it required more time than the EFS framework for execution.

To enhance understanding of the wavelength selection presented in Fig. 3.4.2, it is necessary to examine the role of the prominent biological chromophores in affecting diffuse reflectance. For instance, in the VIS-NIR range normally defined as 400 to 1000 nm, the oxygenation states of Hb is an important indicator that reveals tissue function, composition or structure, which optically exhibit a primary absorption peak at around 414 nm with secondary peaks at around 543 and 577 nm for oxygenated Hb, and for deoxygenated Hb, a primary peak at around 433

nm and a secondary peak at around 556 nm. In the SWIR region, collagen, lipid and water contents are significant absorbers. Specifically, collagen displays absorption peaks at around 1200, 1500, 1725 nm, and a shoulder at around 1690 nm; lipids at around 920, 1040, 1210, 1430, 1730 and 1760 nm; and water at around 970, 1180, 1430, 1930 and 1975 nm[192]. The study has also indicated that DRS measurements in the SWIR region could potentially offer increased sensitivity to detecting water and lipid contents for various clinical applications including cancer diagnoses, burn, and atherosclerotic plaque due to the corresponding differences in their distinct absorption coefficients at each peak.

For this study, the four FS frameworks, which highlighted the observation that absorption of tissue chromophores contributed to class prediction, considered the correlations in between the final 10 selected wavelengths, where they jointly formed the most suitable subset for the classification problem. Although PCA, LDA and biPLS are different algorithms in principle, FS frameworks implementing them systematically selected similar wavelengths as the most relevant features in *cortBone vs. rest* including 1211, 1188 and 1207 nm of less than 25 nm apart, corresponding to one signature absorption peak of lipid, where the difference in balance accuracy was statistically insignificant as shown by the standard deviations in Table 3.4.2 (Top). The fine resolution calculated by FS frameworks might not be precisely distinguished by hardware in practice given that the FWHM of an average LED is around 20 – 30 nm. The minimal difference between the three selected wavelengths could also be caused by the limited resolution of the DRS system. In some cases, LEDs of larger FWHM widths could be preferred over laser diodes of narrower bandwidths, since by encompassing more wavelengths such as the spectral band resulted from EFS framework covering 1200 – 1216 nm Fig. 3.4.4c the balanced accuracy was improved from 88% to 94%. For *boneCement vs. rest*, PCA and LDA FS frameworks both selected wavelengths at around 1460 nm corresponding to one prominent absorption peak of water, of which the behavior was also reflected by the spectral band generated from the EFS framework. The biPLS FS framework however chose the top wavelength in the farther SWIR region at 1800 nm, and the final subset of 10 features did not include features around 1460 nm. Balanced accuracy was nevertheless comparable. Such observations not only demonstrated multicollinearity in the EWDRS dataset but also implied drawbacks of implementing algorithms that involved data transformation. Specifically, the FS frameworks firstly identified all-relevant features via the core algorithms, namely based on PCA to search for maximized class variance, LDA to search for maximized class separability and PLS to search for a linear regression between features and class labels on a projected lower

dimension. The initial pool of all-relevant features was created through the computation process that satisfied the principles and conditions of the core algorithms, which might not necessarily translate to high classification scores in the original data space even with implementation of optimization techniques.

Secondly, the frameworks were designed to remove collinear features from the pool of all-relevant features, which discarded wavelength features that were not only adjacent on the spectrum but also bore similar discriminative strength, leading to a final subset of 10 selected features that potentially contained features of minimal predictive power but were still relevant. Wavelength selection from the three FS frameworks in Fig. 3.4.2 included features that did not correspond to specific signatures of prominent absorbers present or lacking in biological tissues. They were considered relevant in the original data space presumably due to the difference in signal intensity, namely the amount of tissue chromophores contained in the specimens leading to different levels of diffuse reflectance. For example, the features selected by the LDA FS framework included wavelengths in the 800 – 1000 nm range, over which prominent tissue chromophores such as collagen, Hb, lipid and water demonstrate broader absorption spectra. In general, the final subset of wavelength features tended to largely fall towards the SWIR region of 1100 – 1800 nm, especially for *boneCement vs. rest*, with some selection from the VIS region of 400 – 600 nm Fig. 3.4.2 and Fig. 3.4.3. The observation suggested that the higher level of diffuse reflectance signal in addition to the absorption signatures in the SWIR region contributed greater predictive power than absorption alone in the original DRS data space. During orthopedic surgery involving a low level of active bleeding, this behavior in fact demonstrated utility of the SWIR region as the illumination wavelengths over which Hb exhibited minimal absorption, and offered advantages as to reducing the effect of blood contamination on DRS measurements. Moreover, LDA was used both as a classifier and as part of the FS framework, which could contribute to the highest balanced accuracy on the final feature subset because the selection was tailored to this specific classifier resulting in an improved model performance.

A similar trend was also observed in the EFS framework. The EWDRS dataset might not contain as many important features that were both relevant to classification and unique to each other. The final subset of the least collinear features therefore included relevant features with minimal predictive power, rendering the order of features within the rank crucial. The first feature in the rank offered the greatest weight to classification whereas the lower ranked

features provided minimal contribution. This could be seen in Fig. 3.4.4 (a-c), where the balanced accuracy curves reached the first plateau with inclusion of the first 3 – 4 features though the increase in balance accuracy was statistically insignificant due to overlapping error bars in Fig. 3.4.4c. For *cortBone vs. rest*, the final subset of 10 least collinear features reached the highest balanced accuracy in the VIS/NIR/SWIR range when the input data to the EFS framework included all features. Increase of the classification score was observed as more features in the NIR and SWIR ranges were gradually added for evaluation using the EFS framework. A comparable pattern was shown for *boneCement vs. rest*, though a 100 % balanced accuracy was individually achieved in the three spectral ranges with inclusion of all 10 least collinear features. The least collinear features however formed clusters at certain wavelengths in the VIS and VIS/NIR ranges for both scenarios in Fig. 3.4.3 (b, d), suggesting that there were not as many important and distinct features of high discriminate power in the spectral range, over which it might be less suitable to select representative wavelength features from for this classification problem. Furthermore, the final subset of the least collinear features included wavelengths that did not correspond to distinct absorption signatures, indicating that they were rather selected as a result of maximized difference in signal intensity. For example, the EFS framework selected spectral bands at which the difference in signal intensity was maximized inside the VIS (top) and VIS/NIR (middle) ranges for both scenarios in Fig. 3.4.3 (a, c). Contribution of Hb absorption was only deemed important to classification when multicollinearity removal was required. This was seen in the VIS (top) and VIS/NIR (middle) ranges in Fig. 3.4.3 (b, d), where wavelengths at around 550 nm were included in the final selection as compared to Fig. 3.4.3 (a, c). Lastly, both the final subsets of a spectral band and the least collinear features tended to include wavelengths in the SWIR region of 1100 – 1800 nm, further illustrating that not only the higher level of diffuse reflectance signals but also the increase in absorption sensitivity of water and lipid contents played an important role to classification in both scenarios. Contribution of Hb in the DRS measurements could be one of the top factors that interfered with classification accuracy and thus its absorption signatures were not selected as features of sufficient discriminative power. In the literature, R. Gunaratne et al.[193] concluded that wavelength features with the most discriminative power largely existed in the spectral range of 370 – 470 nm and 800 – 1010 nm where Hb, water and lipid could be major contributors to classification, corresponding to the findings in our study.

Limitations of this work stemmed from dataset creation, which was specifically designed for data mining and was measured in a static laboratory environment. The exact results might not

be generalizable to other situations such as an ongoing surgery involving active bleeding or a different experimental setup generating new DRS datasets. Under such circumstances, rigorous data preprocessing will be required to standardize and normalize across different datasets, and new features or class labels will need to be engineered to address external environmental factors. It is nevertheless believed that the FS frameworks described here can be adapted to new scenarios of changed class labels with little modification, given that the usage is justified and assumptions of the algorithms are met. For future directions, the selected wavelengths from the FS framework including 1210 nm to inform the bone-to-tissue interface and 1460 nm to inform the cement-to-bone interface will be validated in a laboratory setting mimicking an orthopedic operation, and subsequently implemented in the optical probe as the light sources for further translational experiments in *in vivo* subjects. It is envisioned that an ML system will be established based on one-class classification to specifically identify bone cement during cement removal procedures. The initial train/validation dataset of bone cement in various conditions will be collected including ageing, blood contamination and PBS hydration at body temperature. The ML system shall be able to re-train itself iteratively given new data and polish its classification prediction.

3.6 Conclusions

The present work described four different FS frameworks designed for tissue differentiation in the field of orthopedics to select important wavelength features in the EWDRS dataset. Three FS frameworks were constructed by implementing conventionally used algorithms including PCA, LDA and PLS to identify important features for classification, while the other was formulated via an ensemble approach to achieve the same goal without involving data transformation. All frameworks generated comparable results and model performance; in particular, the EFS framework was able to generate more interpretable models as well as being more efficient on algorithm and time complexity. The final subset of 10 selected features contained not only wavelengths corresponding to prominent absorption peaks of major tissue chromophores such as Hb, water, lipid and collagen at around 600, 1200, 1400 and 1500 nm, but also wavelengths at maximized difference of signal intensity to further improve classification accuracy. In the future, the EFS framework will be adapted to an application-specific scenario where it will be used as a rigorous basis for determining light source(s) and

fast-track optical design in the subsequent stage of instrumentation for bone cement removal guidance in rTHA surgery.

3.7 Code, Data, and Materials Availability

The EWDRS dataset used for the analysis is available in a public Github repository or Zenodo repository (DOI: 10.5281/zenodo.7554759) all licensed under CC-BY-NC-SA-4.0:

https://github.com/Biophotonics-Tyndall/PUB-FeatureSelectionDataset.git.

The code in .ipynb format used to generate the results and figures is available in a public Github repository or Zenodo repository (DOI: 10.5281/zenodo.7554778) all licensed under CC-BY-NC-SA-4.0:

https://github.com/Biophotonics-Tyndall/PUB-FeatureSelectionCode.git.

Supplementary material can be found in a public Github licensed under CC-BY-NC-SA-4.0:

https://github.com/Biophotonics-Tyndall/PUB-FeatureSelectionSuppl.git.

The authors intend to submit a complementary Data Descriptor article to Scientific Data subsequently upon acceptance of this article.

Following the successful development of DRS feature selection frameworks and the identification of discriminative DRS wavelengths, the focus of the next chapter shifts to the predictive capability of DRS measurements. For bone drilling especially in cranial bones, important DRS wavelength features for depth prediction in hard tissues are explored. The next chapter demonstrates the potential of DRS to effectively predict lookahead distances in cranial bones, providing insights into the clinical translation of DRS technology in bone-related surgical applications.

Chapter 4
Depth prediction in cranial bones using diffuse reflectance spectroscopy for craniotomy

4.1 Chapter Overview

This chapter introduces the concept of depth prediction using spectral data collected in Chapter 2. The primary objective of this chapter is to demonstrate the feasibility of predicting lookahead distance in hard tissues using diffuse reflectance spectroscopy data.

Removal of cranial bone flaps, which is often required in neurological surgery via craniotomy, is frequently performed using surgical drill perforators to create burr holes in the skull. Associated risks with drill plunging can be life-threatening to the patients. In this *ex vivo* study, we investigated the feasibility of diffuse reflectance spectroscopy (DRS) to predict lookahead distance in cranial bones as a potential safety measure during craniotomy. The dataset was established by collecting DRS measurements from stepwise drilling of fresh porcine skulls, and subsequently corrected by oversampling techniques. Wavelength features including 450, 700 and 1200 nm each with a ± 25-nm range were selected to reduce computational burden. Linear discriminant analysis (LDA), random forest (RF) and K-nearest neighbors (KNN) were deployed to compare classification accuracy scores between all versus selected features (LDA: 88% and 88%; RF: 91% and 90%; 82% and 82%, respectively). Monte Carlo simulation was employed for diffuse reflectance simulation at selected wavelengths to determine the thickness of the skull at which DRS signals started to change. Partial least squares (PLS) regression and feedforward neural networks (FNN) were used to construct prediction models for skull thickness ranging from 1 to 5 mm away from the brain, yielding a root mean squared error regression loss of 0.08 and 0.06 mm from PLS, and 0.2 and 0.1 mm from FNN for all versus selected features, respectively. The potential of DRS to predict lookahead distance in cranial

bones was demonstrated in this study. Future studies will focus on comparison of different DRS probes and integration into surgical devices.

This chapter is based on the original research (in progress as of the time of writing):

(In progress) Li CL, Fisher CJ, Komolibus K, et al. Depth prediction in cranial bones using diffuse reflectance spectroscopy for craniotomy. *Biomed Opt Express*. 2024.

4.2 Introduction

In neurological surgery, adequate access to the inside of the cranium is routinely required by the surgeon to resect malignancies or repair abnormalities. The removal of cranial bone flaps is often performed through traditional craniotomy or craniectomy using surgical drill perforators, thus creating burr holes in the skull to expose the brain[262]. Although such procedures are necessary and beneficial for a wide range of conditions from cancer to traumatic injuries, the inherent risks associated with removing part of the skull can lead to life-threatening complications in the post-operative setting, including but not limited to external cerebral herniation, intracranial hemorrhage and epilepsy[263,264]. Moreover, intraoperative risks related to the mechanical operation of the cranial drill can pose uncertainties to the surgical outcome. Plunging, namely a sudden increase of drilling speed and depth in an uncontrolled manner towards the brain, is one of the top concerns that can cause severe penetrating injuries such as dura mater laceration and cerebral contusions[265]. Several studies have also indicated that the event of plunging is underreported, and records showed sufficient prevalence with an occurrence rate of as high as 66% for a singular experience and 22% for more than one encounter[266,267].

In the past few decades, technical advancements have moderately optimized operational performance of surgical drills for craniotomy by introducing safety measures such as a mechanical clutch design. For instance, a commercial electric dual-motor drill with real-time monitoring of drilling depth and torque was assessed by Welcome et al., which demonstrated improved accuracy and precision of burr holes as compared to a manual hand drill[151]. Our group developed an optically enhanced cranial perforator by implementing diffuse reflectance spectroscopy (DRS) detection sensors as a real-time feedback system to inform the bone-to-brain boundary while simultaneously terminating the drill, yielding a success rate of 88%[268]. The use of DRS, which is a point-based optical technique that measures reflected light off samples of interest using a broadband illumination light source, has been widely investigated in various pre-clinical and clinical studies for tumor detection or boundary detection due to relatively lower cost and easy integration with surgical instrumentation[269,270].

Despite the research effort to address the risk of plunging during cranial drilling, the number of studies published in recent years is still very limited in the field. One challenge remains in predicting the lookahead distance of the drilling trajectory, which is especially important for the path transitioning from hard to soft tissues. With advances in machine learning (ML) and

deep learning (DL) model constructions, optical methods such DRS can offer an optimal opportunity to achieve sufficiently accurate depth prediction, since DRS measurements are generated based upon wavelength-dependent optical properties, which could be utilized to approximate the distance between the brain and the perforator. In the literature, prior research focused on Monte Carlo simulations using two- or multi- layered tissue models to extract tissue optical properties and parameters[271,272]. One recent study employed DRS to predict the thickness of top layer in a two-layer model using tissue-mimicking phantoms and *ex vivo* soft tissues, of which the results were compared with ultrasound imaging[273]. The depth prediction model based on DRS achieved a maximum accuracy of 0.35 mm with classification accuracy scores of 95% and 99% for the top and bottom layers, respectively.

In this present study, we aim to investigate the maximal lookahead distance that DRS alone can accurately predict in the cranial bone using Monte Carlo (MC) simulations, as well as ML and DL models. To achieve the primary goal, three objectives are defined, which are 1) To select the most discriminative DRS wavelength features for depth prediction using feature selection frameworks previously developed by our group[200]; 2) To determine the theoretical lookahead distance that DRS could potentially inform by using MC simulations; 3) Based on the previous study on successful detection of immediate bone-to-brain boundaries[268], to examine and compare the classification and regression metrics for depth prediction using selected features versus all features.

4.3 Materials and Methods

All experimental procedures were conducted in accordance with regulatory requirements at Tyndall National Institute, Cork, Ireland. Data analysis was performed using the Python Programming Language Version 3.11.5 (Python Software Foundation, https://www.python.org/) and MATLAB (R2023b, The MathWorks Inc., Natick, Massachusetts, USA, https://www.mathworks.com). Experimental workflow was summarized in Fig. 4.3.1(a).

4.3.1 Experimental Setup

Specimen preparation, data acquisition and data pre-processing were described in detail in our previous publication[154]. In short, fresh *ex vivo* porcine heads (n = 5) were acquired from a local butcher store in Cork, Ireland, and measured immediately post-delivery. Two commercialized spectrometers were utilized with broadband illumination for DRS measurements between 355

to 1850 nm, containing 1531 wavelength channels. Stepwise drilling of porcine skulls was performed manually using a commercialized surgical drill. DRS was measured at each stepwise stop until plunging into the cranium. Depths were measured by a digital caliper to indicate the thickness of the skull, which ranged from 0 (brain) to 25 (surface) mm at a step size of 1 mm. There were in total 23 and 79 measurements of the brain tissues (grey matter) and different thicknesses of the skulls, respectively, with corresponding labels. Standard normal variate (SNV) transformation was applied to the dataset to normalize signal intensities and correct multiplicative scattering effects prior to data analysis.

4.3.2 DRS Feature Selection

To enhance computational robustness, DRS feature selection was performed via two selection strategies, targeting at wavelengths that bear the highest discriminative power for binary classification between brain tissues and cranial bones. The first method was based on the three feature selection frameworks incorporating principal component analysis, linear discriminant analysis (LDA) and ensemble approach developed previously by our group[200]. Common features generated from the three frameworks were selected. The second method was based on the spectral difference between DRS measurements of brain tissues and cranial bones at different depths, calculated by Equation (1):

$$Spectral\ difference = \boldsymbol{S}_{depth} - \boldsymbol{s}_{brain} \quad (1)$$

where $\boldsymbol{S}_{depth}$ denotes an $m \times n$ matrix containing m number of averaged DRS measurements per depth level of the skull and n number of wavelength features, and $\boldsymbol{s}_{brain}$ denotes a $1 \times n$ row vector containing averaged DRS measurements of brain tissues. With DRS signals of brain as the reference spectrum, the selection criteria were pre-defined as spectral regions of the maximum, all positive and all negative differences. Selected features with a ± 25-nm range were included in the downstream analysis. Overlapping features were treated as belonging to the same selected spectral region.

4.3.3 Monte Carlo simulation

To model light transport in turbid media, Monte Carlo eXtreme (MCX) was implemented to generate simulated diffuse reflectance signals at the selected wavelengths in a 3D 4-layered head model comprising skull of 20 mm, cerebrospinal fluid (CSF) of 5 mm, grey matter (GM) of 10 mm and white matter (WM) of 25 mm[274]. The theoretical lookahead distance was

determined by identifying the critical depth where the simulated diffuse reflectance began to change significantly with respect to the thickness of the skull as drilling approached the brain layer. The injected photon package number was 5×10^7. There was one source and one detector included with a separation distance of 1 mm to simulate the optical probe used in the experiments. The optical parameters for MC simulations at the selected wavelengths were found from the literature[194,275,276] (Table 4.3.1), including absorption coefficient (μ_a), reduced scattering coefficient (μ_s'), refractive index (n), and anisotropic factor (g). The optical parameters of CSF were represented as generic values averaged from published studies[276–279]. The refractive index and anisotropic factor of the environment outside of the skull were set to 1.46 and 1, respectively. Table 4.3.1 summarizes the optical parameters used in the 4-layered head model for MCX simulations at approximately the selected wavelengths, excluding 1463 nm due to the lack of reference.

Table 4.3.1 Summary of optical parameters used in the 4-layered head model for MC simulations at 450, 700, 1200 and 1400 nm.

Tissue Type	$\lambda\ (nm)$	$\mu_a\ (mm^{-1})$	$\mu_s'\ (mm^{-1})$	g	n
Skull	450	0.0942	2.43	0.89	1.37
	700	0.00436	1.45		
	1200	0.0879	0.988		
	1400	0.860	0.905		
CSF	Generic	0.00288	0.0100	0.89	1.37
GM	450	0.403	2.05	0.89	1.37
	700	0.0139	1.05		
	1200	0.0998	0.523		
	1400	0.972	0.606		
WM	450	0.102	10.7	0.84	1.37
	700	0.00967	7.69		
	1200	0.122	4.75		
	1400	0.915	4.21		

4.3.4 Class Imbalance Correction

Due to the existing class imbalance, a resampling strategy was developed to oversample classes that were underrepresented in the SNV-transformed dataset. The strategy framework consisted of firstly Random Over-Sampling Examples (ROSE)[280] and secondly the Synthetic Minority Oversampling Technique (SMOTE)[281]. ROSE was used to oversample each class with replacement to contain 10 samples of DRS measurements. Shrinkage, a hyperparameter used to control the degree of dispersion, was set to 0.7 to generate relatively close-spaced sample points. The original SMOTE was then applied to the ROSE-oversampled dataset, increasing the number of samples to 100 per class. Feature selection was performed in advance of oversampling to prevent data leakage.

4.3.5 Classification

The quality of DRS feature selection was validated by comparing classification accuracy scores computed from using all features versus selected spectral regions on the oversampled dataset. Oversampling for classification was performed similarly using the same ROSE-SMOTE strategy, where all DRS measurements on brain and cranial bone were grouped accordingly and oversampled to 100 per class. Three classification models were employed, which were LDA as a linear learner, random forest (RF) as an ensemble bagging learner and K-nearest neighbors (KNN) as an instance-based learner. The One-vs-Rest (OvR) strategy was implemented for binary classification between class labels of brain versus all the rest depth levels. Cross validation (CV) was set to stratified 10 folds with 10 repeats.

4.3.6 Lookahead Distance Prediction

The upper limit of lookahead distance predicted using DRS measurements was decided based on the critical depth value generated from MC simulations at the selected wavelengths. Due to the continuous and linear nature as drilling towards the brain, regression techniques were chosen for the task, which included partial least squares (PLS) regression and feedforward neural networks (FNN). Selected wavelength features were used in the analysis and compared with using all features. The holdout dataset of 20% was split out prior to analysis. Coefficient of determination (r^2) and root mean squared error regression loss (RMSE) were reported as the metrics of model performance on both the training and holdout datasets. For PLS regression, CV was set to 10 folds with 10 repeats on the training dataset. For FNN, the number

of epochs was set to 1000. CV was not implemented due to the limited size of the dataset. PLS regression and FNN model summary were shown in Fig. 4.3.1(b).

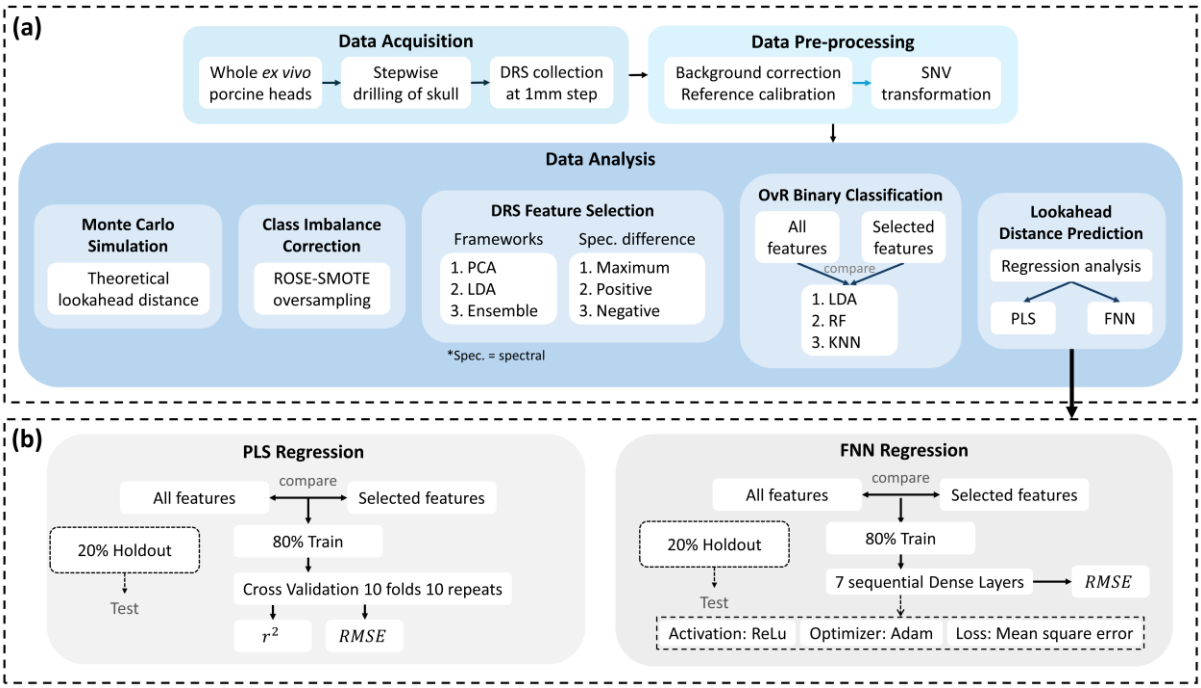


Figure 4.3.1 Experimental workflow. (a) Flowchart of data acquisition, pre-processing and analysis. DRS feature selection frameworks can be found in[200]. (b) Model summary for PLS regression and FNN.

4.4 Results and Discussion

In this work, DRS data was investigated to predict lookahead distance in cranial bones for craniotomy. Feature selection techniques were employed to reduce not only computational burden by removing data redundancies, but also instrumentation complexity by selecting specific wavelength ranges that bore high discriminative power as illumination light sources for future translational studies. Fig. 4.4.1 illustrates the selected wavelength features via the two strategies based on spectral change and the three selection frameworks. There were overall four important regions identified, which included 400, 700, 1200 nm and in between 1400 and 1460 nm, all with a ± 25-nm range. The maximum, all positive and all negative spectral differences between brain and cranial bone were found at 414, 1463 and 1200 nm, respectively, which were entirely dependent on the spectral characteristics of the SNV-transformed dataset (Fig 4.4.1a). One additional feature was identified at 1400 nm, highlighting the cross-over region with the reference spectrum (GM, brain). The three feature selection frameworks

outlined two spectral regions, including 700 and 1200 nm (Fig 4.4.1b). One outlier at 760 nm was merged with the closest feature. The 450 and 700 -nm regions correspond to the absorption troughs of oxy- and deoxy- hemoglobin in the visible and near infrared windows, while the 1200 and 1400 -nm regions correspond to the absorption peaks of lipids[192,282]. In practice, given that lipid contents are one of the major differences in composition between brain and cranial bone, the selection is advantageous such that thickness prediction would be primarily dependent on the differences in lipid contents with minimized signal contribution from blood. The criterion for this feature selection task, which was to discover discrimination features between brain and bone via binary classification, was determined based on the assumption that the depth information through DRS is mostly provided by the second layer (GM, brain) as the reference in a geometry that broadly resembles a two-layer model. In the ideal situation where the perforator never plunges into the cranium while approaching closer and closer to the brain, the change of DRS signals with respect to the thickness of the first layer (cranial bone) is established upon the combination of the optical properties of both layers and would vary greatly if the second layer were changed.

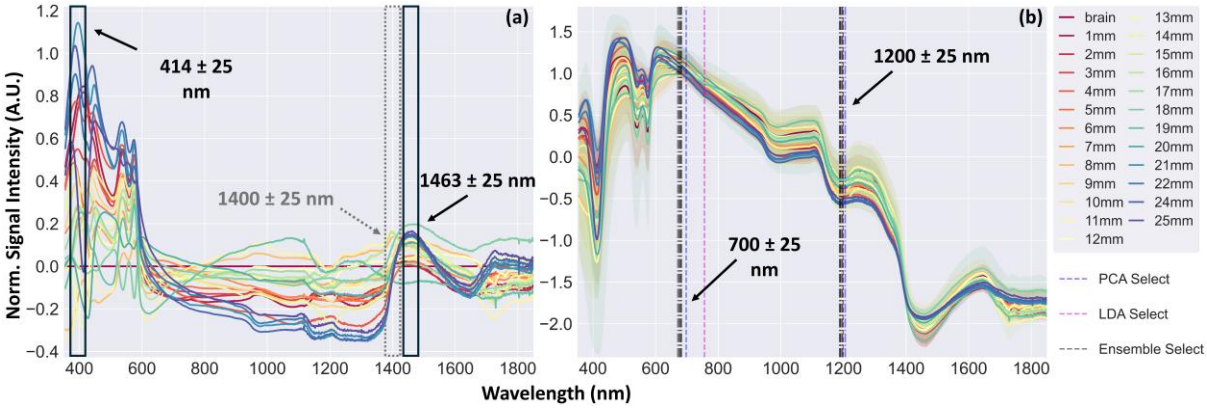


Figure 4.4.1 The selected wavelength features for the OvR binary classification on the SNV-transformed DRS dataset between brain and cranial bone implementing (a) calculation of spectral difference showing features that satisfy user-defined criteria, with one additionally identified feature; and (b) feature selection frameworks based on PCA, LDA and ensemble approach. Number of pig heads = 5; number of drilled holes = 11; number of DRS measurements = 102.

Fig. 4.4.2 shows the MCX simulated diffuse reflectance as a function of skull thickness with distribution of fluence rate at surface for the corresponding wavelengths. The critical depth at which the DRS signal began to decrease significantly was estimated to be approximately 5 mm away from the CSF layer at 450, 700 and 1200 nm, while the simulated reflectance exhibited an opposite behavior at 1400 nm. The signal level decreased to the lowest point at CSF and

increased back to approximately 50% of the maximum level once the brain layer was reached. Additionally, the porcine skulls used in the experiments lacked the CSF layer due to the severed necks. As a result, to prevent confusion in the regression models, the upper limit for predicting lookahead distance based on DRS was theoretically determined to be 5 mm and lower limit to be 1 mm just prior to plunging. Spectral region around 1400 was also excluded from regression analysis due to the reversed behavior. The increment resolution was configured to 1 mm, providing sufficient time and distance for the drill to come to a full stop.

The OvR binary classification accuracy scores using LDA, RF and KNN classifiers on the ROSE-SMOTE oversampled dataset were summarized in Table 4.4.1 for all versus selected wavelength features. The three supervised learners were chosen to diverse the classification approaches for robustness, which represented different underlying assumptions and algorithms such that LDA utilizes a linear combination for class separations, RF relies on bootstrap aggregation of sub-decision trees via ensembles, and KNN is instance-based that defines class membership by votes of neighbors. The resulting classification accuracy scores showed similarities with overlapping standard deviation ranges among the three classifiers, suggesting that the existing pattern in the dataset was consistent with straightforward separations. Another possibility for such behaviors could be stemming from overfitting, which should be largely avoided with the amount of CV implemented in classification. By comparing selected with all features, consistent accuracy scores were also observed, indicating that the selected features held the most discriminative power and thus became representative in this classification task for downstream analysis to mitigate the curse of dimensionality in ML.

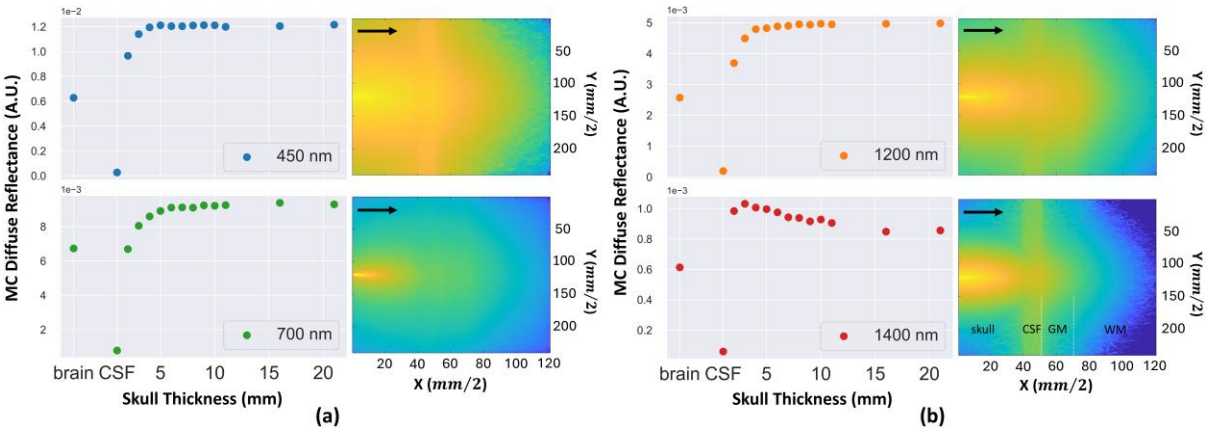


Figure 4.4.2 Monte Carlo simulations of diffuse reflectance as a function of skull thickness (left) and fluence rate distribution (right) at (a) 450, 700, (b) 1200 and 1400 nm in the four-layered head model with separations shown at the bottom right.

Table 4.4.1 OvR binary classification accuracy scores between brain and cranial bone using LDA, RF and KNN classifiers on the ROSE-SMOTE oversampled dataset with all and selected wavelength features.

Accuracy (%)	All Features	Selected Features
LDA	88.3 ± 7.69	88.0 ± 8.06
RF	91.2 ± 5.57	89.8 ± 6.42
KNN	82.1 ± 7.49	82.0 ± 8.54

Fig. 4.4.3 and 4.4.4 show the predicted thickness of cranial bone by PLS regression on the training dataset and FNN on the holdout dataset using all features versus selected features plotted against the true thickness, respectively. Regression metrics on the training and holdout datasets of the ROSE-SMOTE oversampled dataset were summarized in Table 4.4.2. Values were rounded up to three decimal places. By comparing both r^2 and RMSE of CV, regression performance of selected features was slightly improved from using all features. No signs of overfitting were observed by comparing results on training and holdout/validation datasets in cross validation. Standard deviations were generated from CV and repeated testing. The value of r^2 was unavailable for FNN on the training dataset. PLS regression slightly outperformed FNN on this dataset to predict lookahead distance. In particular, as comparing to FNN, PLS regression is more proficient in handling comparatively smaller datasets, and addressing multicollinearity, which is a common phenomenon in spectral data[200]. To prevent limitations such as overfitting, FNN conversely requires larger datasets for better performance. Furthermore, some of the predicted thicknesses tended to be greater than the true thicknesses in the PLS model (Fig. 4.4.3a,b) and the FNN model (Fig. 4.4.4a) with a few outliers. One possible explanation for the observation could be attributed to influential outliers leading to biased predictions. Such a disadvantage in the regression analysis could be alleviated by increasing the dataset size by experiments and thus reducing the amount of oversampling. In clinical settings it would be preferred to underestimate (lower than true values) in the monitoring phase to allow for more time to stop and thereby ensure drilling safety.

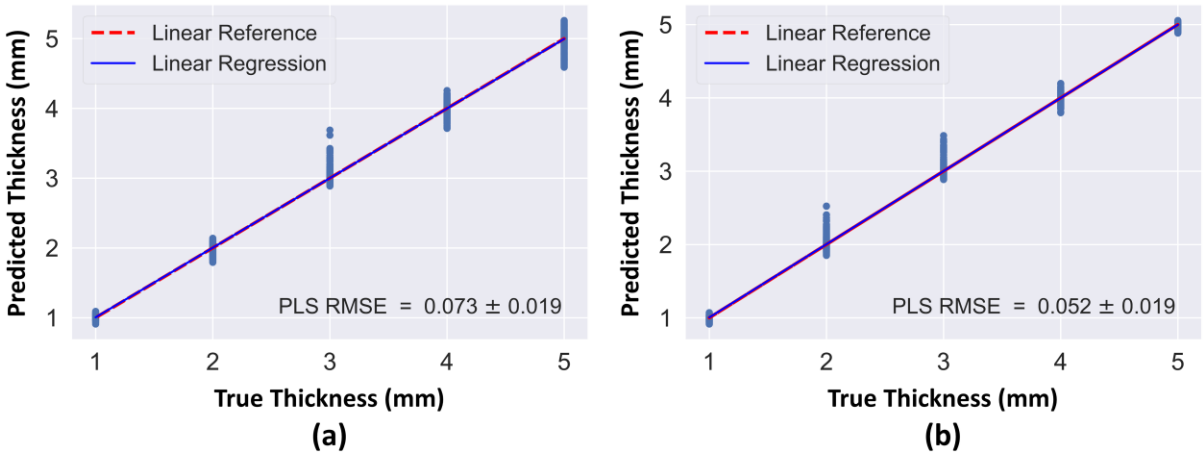


Figure 4.4.3 PLS regression showing the predicted compared to the true thickness of the cranial bone ranging from 1 to 5 mm on the ROSE-SMOTE oversampled dataset with (a) all features and (b) selected features.

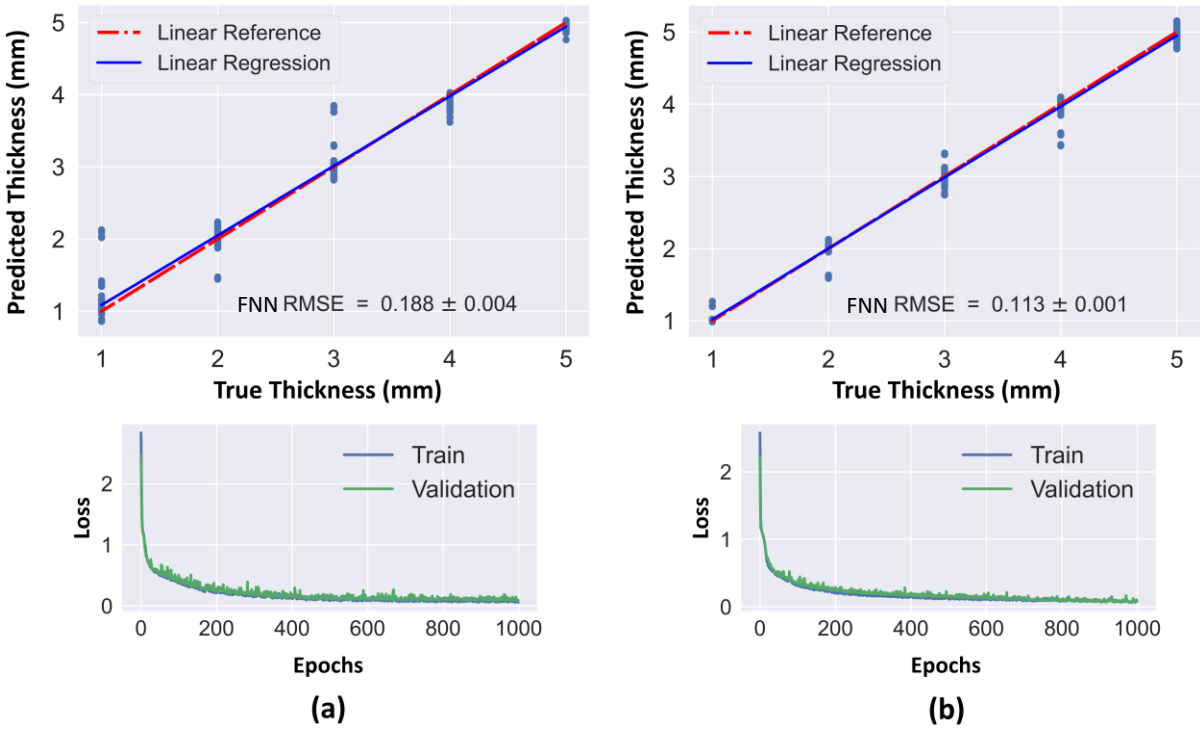


Figure 4.4.4 FNN showing the predicted compared to the true thickness of the cranial bone ranging from 1 to 5 mm on the ROSE-SMOTE oversampled dataset with (a) all features and (b) selected features. Validation loss is shown on the bottom panel.

Table 4.4.2 Summary of regression metrics from PLS and FNN for all features and selected features on the ROSE-SMOTE oversampled dataset. Values were rounded up to three decimal places.

		All Features		**Selected Features**	
		Train	Holdout	Train	Holdout
PLS	r^2	0.997 ± 0.002	0.997	0.998 ± 0.001	0.997
	$RMSE$ (mm)	0.073 ± 0.019	0.078	0.052 ± 0.019	0.059
FNN	r^2	N/A	0.982 ± 0.001	N/A	0.987
	$RMSE$ (mm)	0.127	0.188 ± 0.004	0.194	0.113 ± 0.001

On the other hand, the role of oversampling in this study was crucial as it corrected class imbalance in the dataset, where the number of DRS measurements at each thickness of cranial bone was significantly lower than that of brain. For instance, classification model performance was improved from accuracy scores of 50 – 60% pre oversampling to 80 – 90% post oversampling. The underrepresented class was learnt more efficiently by the models with less bias based on a larger dataset. Because of data sparsity in the original dataset, oversampling additionally increased model stability and reduced variability for the regression analysis. Despite the advantages, overfitting can be a major issue that leads to loss of model diversity, inability to capture underlying patterns and poor generalization on unseen data. This could be mitigated by setting hyperparameters to produce closer-spaced data points and limit the size of oversampling. One major disadvantage present in the study was the limited number of measurements per class. Data leakage would be observed during the process of train test split after oversampling, where the small dataset of original measurements was replicated and distributed leading to severe bias. For instance, the prediction at 1 mm was particularly less scattered as compared to the rest, because the original number of measurements prior to oversampling was low. No treatment was performed to split the original dataset therefore leading to data leakage. Techniques such as data split before oversampling, leave-one-out cross validation and increasing the dataset should be implemented to correct the issue. In any case, the feasibility of DRS to predict lookahead distance was demonstrated using existing data. More generalizable prediction models could be built with larger datasets.

In addition, the maximum lookahead distance predicted by DRS in cranial bone would be influenced considerably by the source-to-detector separation distance on the probe. Based on MC simulations, greater source-to-detector separation distance could lead to predictions of

longer lookahead distances, namely farther boundary detection between two tissue types up to 10 mm, due to the increased DRS acquisition volume. It would however possibly compromise the prediction accuracy of short distances when it becomes more important to signal plunging events. For clinical translation, a notable challenge present in this study is the absence of *in vivo* validation experiments. Even though the predictive models constructed based on the existing *ex vivo* dataset demonstrated promising outcomes and provided valuable insights, the complete assessment of model generalizability and translation to a more versatile clinical environment could not be accomplished without *in vivo* validation testing. Interspecies differences in bone properties including density, composition and thickness could all contribute to model performance, possibly making it less relevant for clinical scenarios. For technical limitations, the key obstacle lies in the practicality of integrating DRS technology with existing surgical tools, where not only the size of the components and portability of the equipment could potentially lead to translation failure, but also the light coupling between static and rotating components as well as the opto-mechanical misalignment in drilling could complicate the translation process.

4.5 Conclusions

This study explored the potential of using DRS alone to predict lookahead distance as a safety measure for drilling in craniotomy. Feature selection techniques were used to discover wavelength feature ranges that held high discriminative power for binary classification between brain and cranial bone and therefore reduce computational burden. LDA, RF and KNN generated comparable classification accuracy scores by using all features versus selected features. MC simulation was utilized to simulate diffuse reflectance at the selected spectral regions including 450, 700, 1200 and 1400 nm. The thickness of skull at which the simulated diffuse reflectance began to decrease was found at 5 mm away from the CSF layer. PLS regression and FNN model were employed to predict the lookahead distance, yielding a RMSE value of approximately 0.06 and 0.1 mm, respectively. The feasibility of the proposed technique was demonstrated by the results; however, to construct a more generalizable prediction model more experimental DRS measurements are required. For future directions, DRS probes with larger SD separation distance will be examined and compared to determine the optimal configuration.

Following the feasibility assessment of DRS in predicting depth in hard tissues, the focus of the next chapter shifts to two preliminary studies that aim to serve as the basis for future research with broader implications. The first study demonstrates the practical aspects of DRS device prototyping for future clinical experiments. Performance of the miniaturized optical prototype device is evaluated. The second study explores additional clinical opportunities for ultrafast lasers, specifically with the use of picosecond infrared laser mass spectrometry for tissue differentiation in bone-related surgical procedures. The last chapter concludes with a summary of the thesis research, an evaluation of study limitations and suggestions for future research. Self-reflections on personal and professional development along the PhD journey are provided at the end.

Chapter 5
Future research and conclusions

5.1 Chapter Overview

This chapter discusses the future research directions based on two preliminary studies and lastly presents the conclusion of the thesis. The first preliminary study presents the concept design of a miniaturized optical probe developed for guidance of bone cement removal and the first *ex vivo* experiment performed to assess the probe. The second preliminary study analyzes the potential of ambient mass spectrometry using a picosecond infrared laser for plume generation to differentiate biological tissue types and bone cement. Limitations and future research directions are considered. Conclusion is subsequently provided to summarize the thesis. Finally, a reflection on the personal and professional development during my Ph.D. journey is provided at the end.

5.2 Preliminary Study I: Concept design of a miniaturized optical probe for guidance of bone cement removal in orthopedic surgery

5.2.1 Background

The incidence of primary total hip arthroplasty (pTHA) has been increasing globally because of the ageing population, leading to the projection of more revision total hip arthroplasty (rTHA) cases in the forthcoming years and a higher occurrence of multiple revisions in individuals due to longer life expectancy. Technology advances have prolonged implant survival and quality of life for patients post pTHA; several complications however can indicate the need for early revision including periprosthetic fracture, implant instability, sepsis and pain. For the past several decades, the surgical procedure of rTHA has been technically challenging and time consuming for orthopedic surgeons because extraction of well-fixed implant and bone cement often involves significant risks of substantial bone loss, femoral fracture and cortex perforation[283,284]. Caution and considerations of reconstruction techniques are necessary to minimize the zone of injury therefore allowing for the possibility of subsequent revision surgeries especially for the older patient cohort. Holt et al.[285] discussed the technique of cement-in-cement revision for cemented implants under different clinical conditions with well-fixed cement-bone interface from pTHA, periprosthetic fractures and impaction grafting. In particular, this technique retains and re-utilizes the existing cement mantle of which the surface is prepared by rasping and drying, and has offered favorable results while avoiding damage and problems from the conventional method. On the other hand, endoscopy is also employed to visualize the intramedullary space for each step of the revision procedure, assisting the orthopedic surgeon to determine sufficient removal of bone cement if not complete, evaluate implant bed and identify infections[286]. Ultrasonic-driven curettes can also be used to extract the distal cement plug with minimal mechanical damage but have the potential to induce thermal burns on the endosteal surface of the femur[287].

Adoption of new techniques and tools is nevertheless dependent on the preference and training of the arthroplasty surgeon. Possible factors such as time constraints, high maintenance, expensive cost, and low maneuverability can prevent wider dissemination and adaptation of novel equipment and complicate its usage during surgery. For instance, in local hospitals it is presently more common to perform pTHA and rTHA using the conventional method where chisels, reamers and drills are used without any image guidance; the success of bone cement

extraction essentially depends on the surgeon's experience and expertise. Due to the absence of adequate visualization tools, optical integration into existing surgical tools for bone cement removal has been investigated by our group, due to its cost-effectiveness, with the aim to guide orthopedic surgeons through rTHA by providing contrast between the cement versus biological tissues as well as visualization of the intramedullary environment. We have since considered different clinical applications of optical sensing in orthopedics and examined potential algorithms for differentiating tissue types and bone cement[28]. Leveraging the existing utilization of endoscopes, in this study we propose the development of an integrated optical system employing diffuse reflectance spectroscopy (DRS) for bone cement detection and miniature image sensors for visual inspection. The optical sensing components are inserted at the tip of bone reamer used to remove the distal cement plug, offering no additional equipment during the surgery and minimal changes to the current clinical workflow.

5.2.2 Materials and Methods

The instrument consists of three subsystems: 1) the custom optical probing unit that collects DRS signals and RGB images, 2) the light source unit that delivers broadband light for illumination as well as narrowband light for spectroscopy, and 3) the light detection unit that processes optical signals. Specifically, Figure 5.2.1a shows the optical reamer probe of approximately 7.5 mm in diameter, where RGB images are acquired by the miniature camera module (NanEye, ams-OSRAM AG, Premstätten, Austria; Footprint: 1.0 x 1.0 mm) in the center of 8 equidistantly-arranged fiberoptic channels and illuminated symmetrically by four source channels, and DRS measurements are collected via two source-detector pairs on both sides of the camera. The optical unit is assembled into a flexible endoscope, which is inserted into the bone reamer and fed through to the tip via a locking mechanism so that it is secured and flush with the surface. Further extension or retraction are permitted depending on specific clinical use cases to provide greater flexibility. The fiber bundle and power cable exist from the center position on the side of the bone reamer handle so that the top part remains intact to allow for hammering.

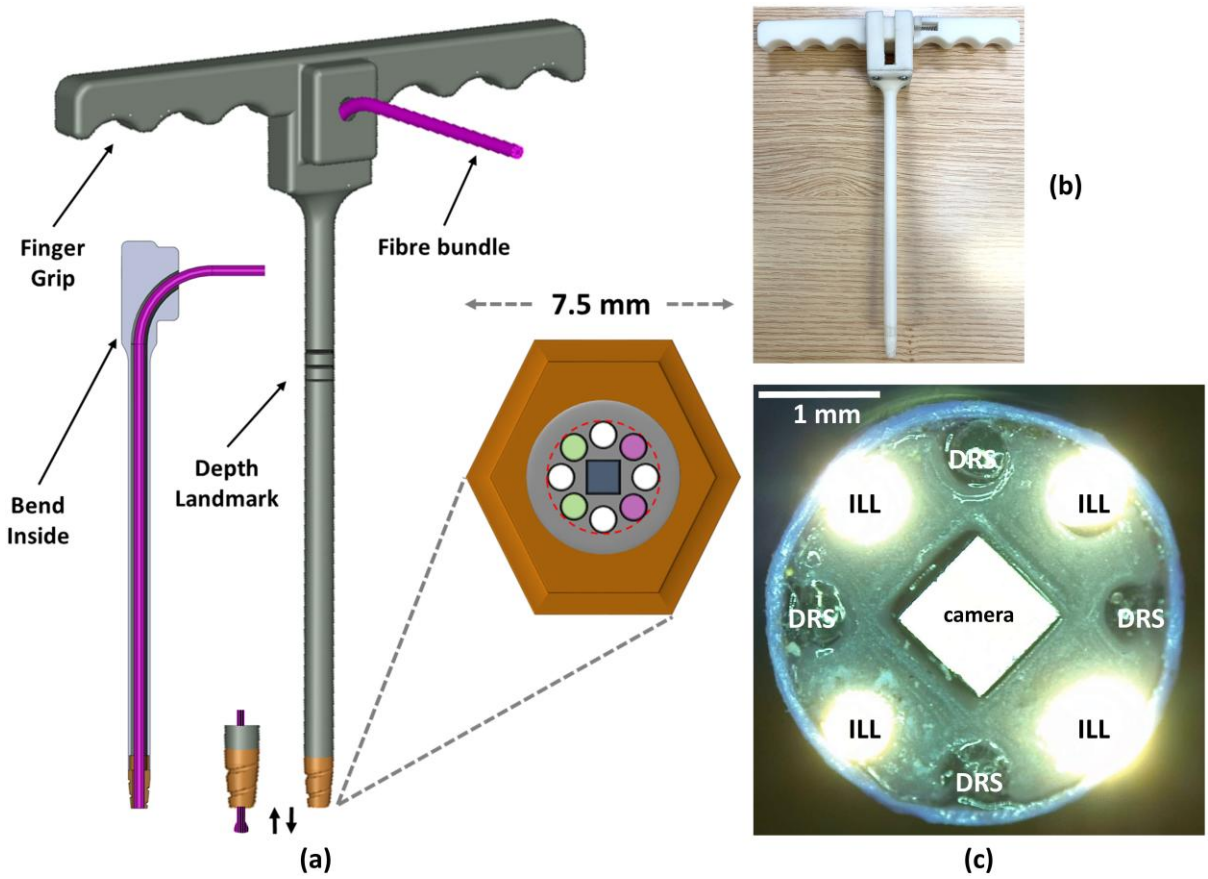


Figure 5.2.1 The optical reamer system for bone cement removal during rTHA. (a) Schematic showing the concept design of the reamer and the optical sensing unit. The miniature camera module (blue square) is positioned in the center of 8 fiberoptic channels arranged equidistantly in a circle (Blue: camera module; green and magenta: DRS acquisition pairs; white: camera illumination (ILL)). (b) 3D printed mock-up reamer. (c) Probe footprint with illumination on.

In the current version of the system, a broadband light source (tungsten-halogen broadband, HL-2000-HP, Ocean Insight B.V., Duiven, The Netherlands) is used as the optical excitation for DRS and imaging, and two spectrometers (Ocean Insight B.V., Duiven, The Netherlands) are used for optical detection across the visible/near-infrared/short-wave infrared (VIS/NIR/SWIR) spectral range. The spectrometers and the broadband source will be replaced by affordable photodiodes and discrete light sources in the subsequent experiments. The initial experiment to test the system included three *ex vivo* specimens. In particular, the bone cement sample (PALACOS® R+G pro, Heraeus Medical GmbH, Wehrheim, Germany) was freshly cured into a single block of approximately 4×4×4 cm prior to measurements. The ovine bone marrow and cortical bone samples were freshly sourced from a local butcher shop and immediately refrigerated.

A more sophisticated experiment was subsequently carried out using one fresh *ex vivo* bovine femur to simulate rTHA, where bone cement was injected into the femoral column as shown in Figure 5.2.2. The bovine femur, which was cross sectioned longitudinally to allow for convenient bone cement injection, was similarly sourced from a local butcher shop and used in the experiment immediately post-delivery. Three different data types were obtained during the simulation experiment as shown in Figure 5.2.3, which included RGB images using the miniature camera module, extended-wavelength DRS spectra using the two commercialized spectrometers with broadband illumination, and intensity signals in voltage measured by an oscilloscope with one InGaAs detector (PDA10CS2, InGaAs Switchable Gain Amplified Detector, 900 - 1700 nm, Thorlabs, Munich, Germany) and two narrowband LED light sources (M1450F1, 1450 nm, 0.86 mW (Min); M1200F1, 1200 nm, 1.6 mW (Min), Fiber-Coupled LED, 1000 mA, Thorlabs, Munich, Germany). For extended-wavelength DRS, there were 20 measurements acquired for individual tissue types including bone cement, bone marrow, cortical bone and the inside of cortical bone. For narrowband DRS, there were 10 measurements acquired for individual tissue types including bone cement, bone marrow and cortical bone at each selected wavelength. Narrowband DRS measurements were subsequently analyzed to determine the classification strength via both One-vs-One (OvO) and One-vs-Rest (OvR) strategies. OvO classification was performed to compute accuracy scores among the three class labels, and OvR was performed between bone cement and the rest class labels. There were six classification models employed to compute classification accuracy scores, which were the same as described in Chapter 3 including logistic regression (LogReg), linear discriminant analysis (LDA), random forest (RF), k-nearest neighbors (KNN), Gaussian Naïve Bayes (GNB), support vector machine (SVM).

All measurements were acquired at room temperature, where the bone cement sample was kept dry and tissue specimens were kept moist with saline spray. All data processing and analysis were performed in the Python Programming Language Version 3.9 (Python Software Foundation, https://www.python.org/) built from open-source libraries, packages and dependencies.

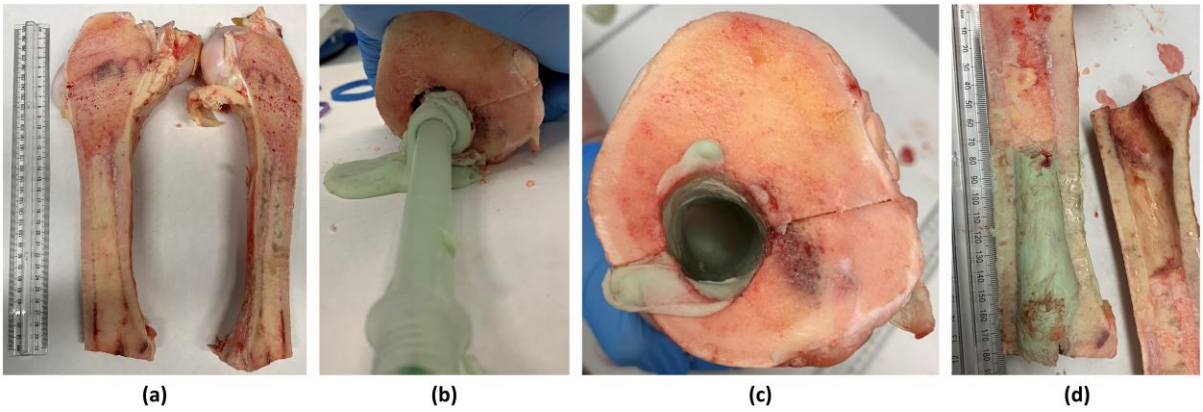


Figure 5.2.2 Bovine femur specimen used in the rTHA simulation experiment showing (a) the original bovine femur cross-sectioned longitudinally, (b) bone cement injection into the femoral column after removal of bone marrow, (c) cemented femoral canal and (b) inside of the bovine femur once the cement was cured.

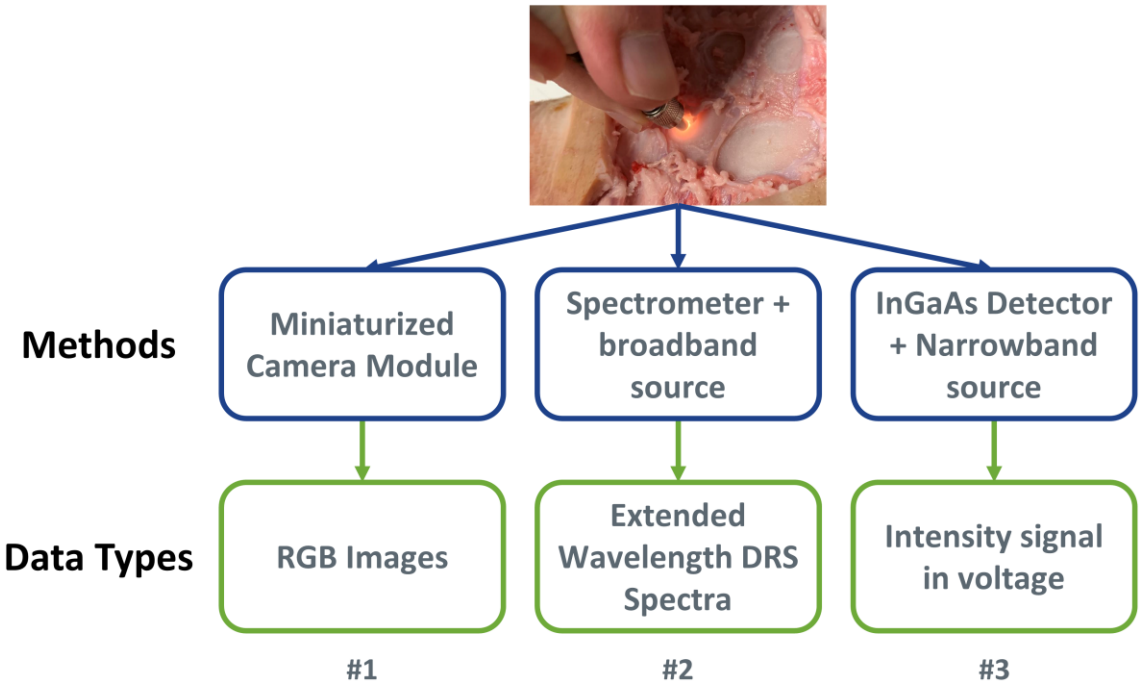


Figure 5.2.3 Workflow of the rTHA simulation experiment consisting of three different methods generating corresponding data types.

5.2.3 Results and Discussion

5.2.3.1 Probe – Design, Construction and Validation

To demonstrate the feasibility of the system, DRS measurements and RGB images were separately acquired from the bone cement sample. DRS measurements of bone marrow and cortical bone samples were additionally collected to address spectral features that could be of

potential use for tissue differentiation. Original RGB images of the bone cement sample are shown in Figure 5.2.4a. Normalized DRS spectra of bone cement, bone marrow and cortical bone are shown in Figure 5.2.4b with black arrows indicating discriminative spectral features at around 650, 1210, 1465 and 1725 nm. The miniature camera module could provide images of bone cement with sufficient spatial resolution to show distinctive surface textures and characteristics. For instance, troughs and speckles were evidently visible in both Figure 5.2.4a and the original image in Figure 5.2.5a. This preliminary observation confirmed that the miniature camera module was suitable for visual guidance during rTHA. The different spectral peaks illustrated by DRS measurements could be utilized as the illumination light sources in the downstream development stages, further reducing and simplifying instrumentation burden and equipment need.

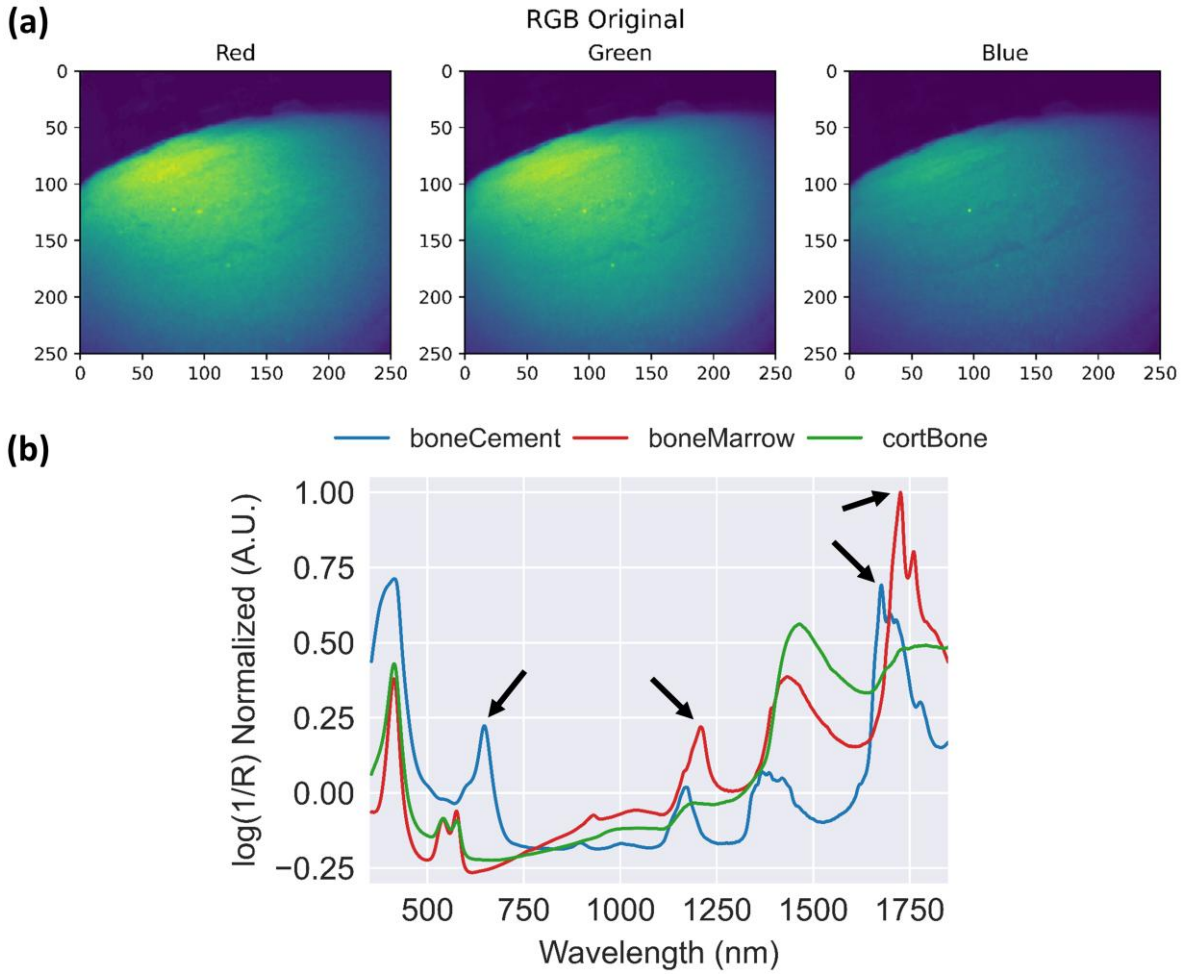


Figure 5.2.4 Initial experiment to test the optical probe. (a) Images showing the original RGB channels from the miniature camera. (b) DRS spectral measurements of bone cement, bone marrow and cortical bone samples. Black arrows indicate the spectral features that could be used to differentiate different tissue types and bone cement.

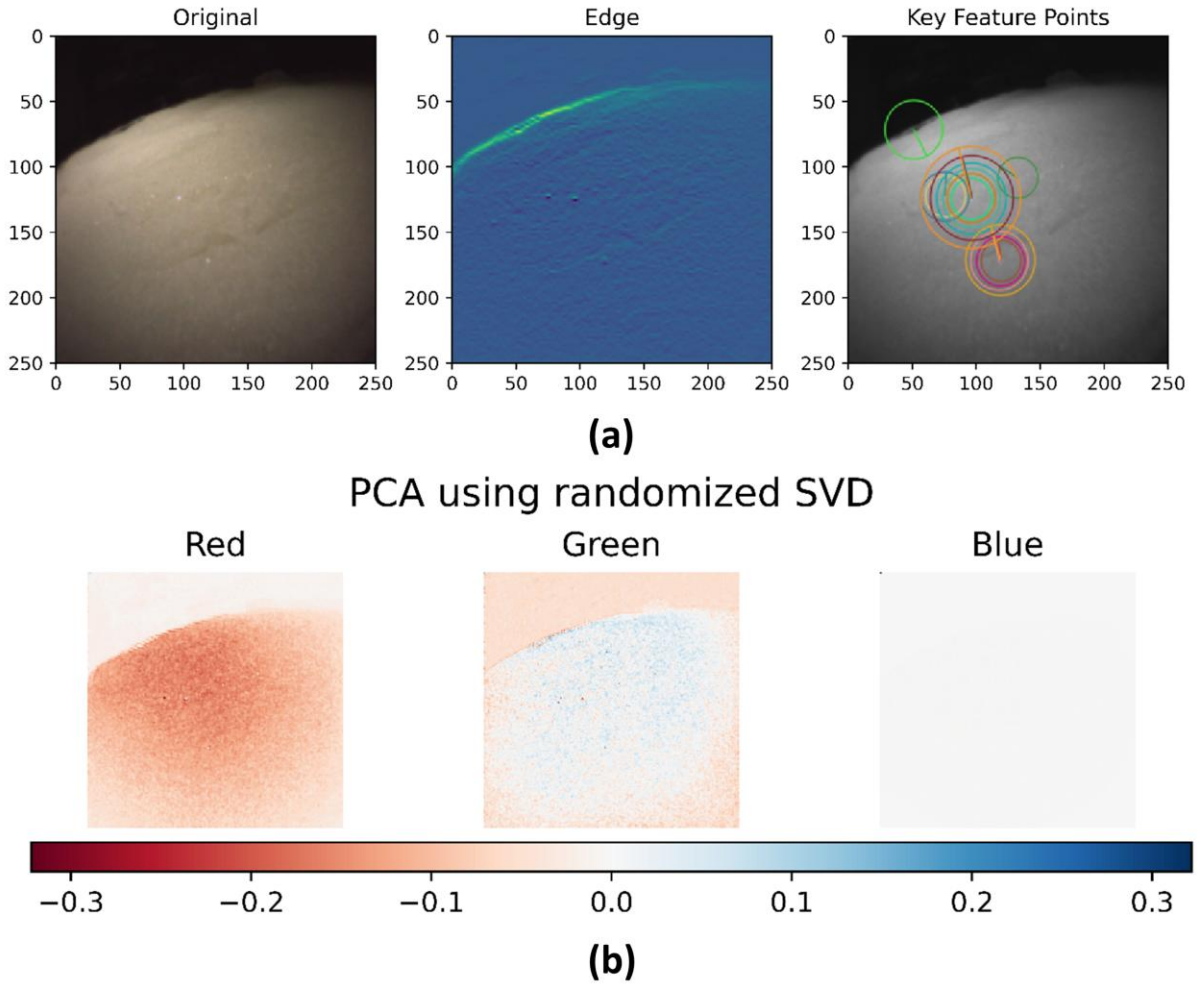


Figure 5.2.5 Image features. (a) From left to right, the original image acquired of the bone cement sample using the miniature camera module, edge features detected by Prewitt filter in the horizontal direction and key feature points computed by Oriented FAST and Rotated BRIEF where the circle indicates the size of the important neighborhood, and the bar indicates the orientation of the key point. (b) Image decomposition by PCA using randomized SVD from left to right showing the red, green and blue channels.

Furthermore, image features could be extracted to assist with identifying not only bone cement but also orientation and position of the probe. Figure 5.2.5a from left to right shows the original image acquired of the bone cement sample by the miniature camera module, edge features detected by Prewitt filter in the horizontal direction and key points computed by Oriented FAST and Rotated BRIEF where the circle indicates the size of the important neighborhood and the bar indicates the orientation of the key point. In particular, edge detection highlighted the surface texture of the material, which could be used as an indicator of different materials or biological tissues encountered by the optically enhanced bone reamer, while key points identified within the field of view could be used to match position and orientation therefore

signaling the depth of bone cement in the intramedullary space. Moreover, image decomposition was performed using principal component analysis (PCA) with singular value decomposition (SVD). This PCA-SVD algorithm projects the image data onto a lower dimension that retains the most variance, which will be useful to compress a stack of images of the same bone cement and thus highlight important features. In Figure 5.2.5b, the blue channel became empty post decomposition while most of the explained variance was preserved in the red and green channels. This observation concurred with the spectral measurements where the difference remained mostly in the green, red and far-red regions.

5.2.3.2 rTHA Simulation in *ex vivo* Bovine Femurs

The RGB images of the bovine femur injected with bone cement acquired by the miniature camera module are shown in Figure 5.2.6, demonstrating some key characteristics such as the bone-to-cement boundary, distal cement plug, blood drops on trabecular bone and surface characteristics of the bone cement with sufficient resolution. Light reflection off the sample during this preliminary experiment was however very high, saturating the detection range of the camera. Optimizations would be needed to adjust the dynamic range of the camera module as well as removing specular reflections by using polarizers.

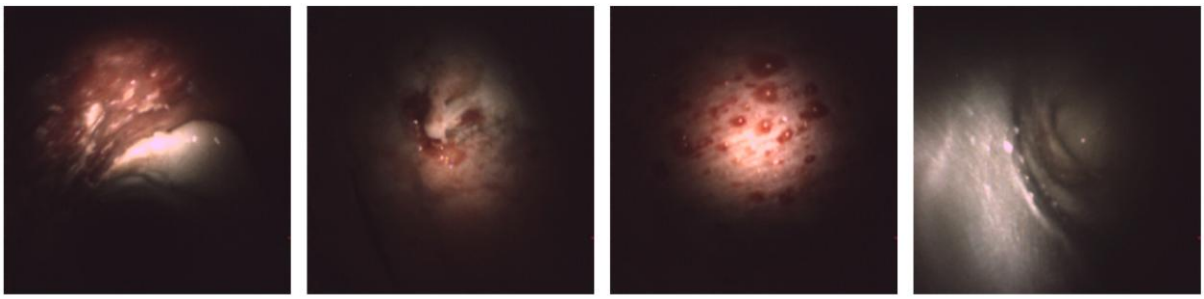


Figure 5.2.6 RGB images acquired by the miniature camera module showing (a) bone-to-cement boundary, (b) distal cement plug, (c) blood drops on trabecular bone and (d) surface characteristics of bone cement.

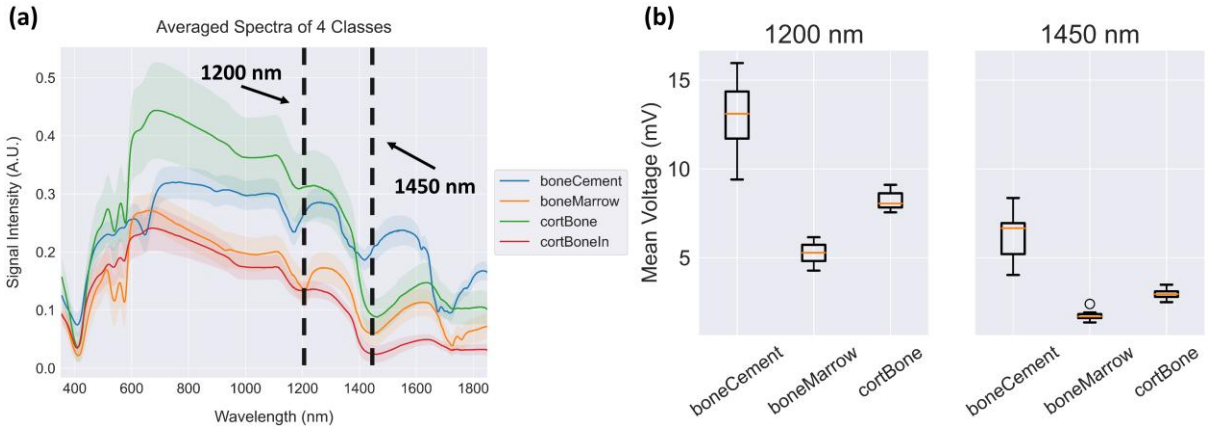


Figure 5.2.7 Results obtained from the optical probe in the rTHA simulation experiment showing (a) broadband DRS from bone cement, bone marrow, cortical bone and inside of cortical bone for 355-1850 nm highlighting lipid absorption at 1200 nm and water absorption at 1450 nm, and (b) mean voltage signals from narrowband DRS at 1200 and 1450 nm for bone cement, bone marrow and cortical bone.

Extended-wavelength DRS measurements of bone cement, bone marrow, cortical bone and the inside of cortical bone are shown in Figure 5.2.7a. Two wavelength features 1200 and 1450 nm representing the absorption peaks of lipids and water, respectively, were selected based on the collected DRS spectra, which were used to inform bone-to-tissue and cement-to-tissue interfaces, respectively. These two wavelengths were utilized as the wavelengths of the narrowband LED light sources to acquire reflectance signals in voltage. Figure 5.2.7b shows the mean voltage signals collected from bone cement, bone marrow and cortical bone at 1200 and 1450 nm. The mean voltage signals were systematically lower at 1450 than 1200 nm for all class labels. The highest mean voltage signal was found from bone cement at both 1200 and 1450 nm. Narrowband DRS signals exhibited consistent patterns at both the two selected wavelengths, where bone cement showed the highest, cortical bone the second and bone marrow the lowest signal level. This observation validated that the two wavelengths could be used for detection of boundaries among bone, soft tissue and bone cement without creating confusion in the classification model.

For OvO binary classification, Table 5.2.1 summarizes the accuracy scores for all pairs and lists the highest performing model. Between bone cement and cortical bone, GNB yielded the highest score of 100%, while other models generated an accuracy score at approximately 95%. For bone marrow and cortical bone, RF generated an accuracy score of approximately 98%, while other models were at 100%. Table 5.2.2 summarizes the classification accuracy scores

for OvR binary classification between bone cement biological tissue types. The six classification models yielded accuracy scores ranging from 92% to 99%, indicating that there was a distinct pattern in the data for the models to discover class separation. In terms of instrument engineering, the number of wavelengths could be safely reduced to only two wavelengths in this scenario.

Table 5.2.1 OvO binary classification among bone cement, bone marrow and cortical bone showing the classification model generating the highest accuracy score.

Class Labels	Bone Cement	Bone Marrow	Cortical Bone
Bone Cement		100% (All)	100% (GNB)
Bone Marrow	100% (All)		100% (All but RF)
Cortical Bone	100% (GNB)	100% (All but RF)	

Table 5.2.2 OvR binary classification between bone cement and the rest class labels showing classification accuracy scores from the six models.

Model	LogReg	LDA	RF	KNN	GNB	SVM
Accuracy (%)	95.8 ± 5.89	91.7 ± 8.12	95.8 ± 5.89	95.8 ± 5.89	98.8 ± 3.75	95.8 ± 5.89

5.2.4 Future studies and Conclusion

For future studies, the system will be examined in phantoms, *ex vivo* samples and *in vivo* animal models. We envision optimizing the system such that discrete excitation light sources will be used in addition to a broadband light source, with the possibility to contribute a new feature to detect infections *in vivo*. The use of miniature spectrometers is also being considered for implementation to capture spectral information. The challenges in the next step can be two-fold: 1) Integration of miniaturized components such as the camera module, DRS spectrometer and discrete narrowband LED sources into one optical probe; 2) Implementation of this sensing unit into a high-speed drilling burr without compromising signal quality.

The clinical motivation of this study is based on the lack of practical image guidance during rTHA. Our preliminary results have clearly demonstrated the feasibility of implementing both spectroscopic measurements, particularly DRS, and imaging to an existing surgical tool, for which the integrated system offers the capability of not only detecting bone cement but also displaying visuals of the intramedullary space.

5.3 Preliminary Study II: PIRL-MS to differentiate bone and surrounding tissues

5.3.1 Background

Ultrafast laser (pico- to femtosecond) for bone ablation has been investigated extensively for clinical translation due to the advantage of high precision and minimal collateral thermal damage as compared to conventional long pulse laser systems[45]. The most frequent clinical use-case is found in dentistry[57] and stapedotomy[288] as a means of precision surgery to achieve improved patient outcomes. Although there is an immense potential for ultrafast laser to be utilized in the clinic, the adoption to general orthopedic surgery such as total knee/hip arthroplasty is moderately restricted by the limited bone ablation efficiency[45] and the lack of sufficient research in direct monitoring. To the best of our knowledge, in the literature only Zhang et al.[87] developed a real-time optical monitoring system via plasma emission spectroscopy by using an inductively coupled plasma optical emission spectrometer to differentiate the bone-to-marrow interface in ovine femur specimens.

Picosecond infrared laser mass spectrometry (PIRL-MS) has demonstrated the capability beyond tissue differentiation to rapidly determine cancer subtypes by analyzing biomolecular constituents, subsequently allowing for tumour grading *in situ* on intra-surgical timescales[289–292]. The PIRL-MS system captures laser plume as samples for MS analysis, which is created by a solid-state picosecond mid IR laser. The collection end consists of a PIRL source probe and a laser plume collection tube, which can be both handheld by the surgeon during an operation for quick assessment of the target tumor.

In this study, we would like to investigate the use of PIRL-MS to differentiate different tissue types and bone cement as a preliminary experiment prior to the next step, where PIRL-MS would be employed to directly monitor ultrafast laser ablation for bone cement removal in total hip arthroplasty. We hypothesize that PIRL-MS can be used effectively to differentiate bone cement from other biological tissues and monitor the progression of ultrafast laser ablation in near real time. The development of such a direct monitoring for ultrafast laser ablation can facilitate clinical adoption of the technology.

5.3.2 Materials and Methods

A fresh *ex vivo* porcine femur was acquired from a local butcher store in Toronto, Canada, which contained specimens of bone marrow, cartilage, cortical bone, fat, muscle, trabecular

bone (Figure 5.3.1). All specimens were unprocessed to mimic the natural condition and measured immediately after purchase. The experimental setup of PIRL-MS was described in other previously published works[290–293]. Briefly, a PIRL laser (~300 mW, 1kHz, Light Matter Interaction, Etobicoke, ON, Canada) was used for laser ablated plume generation, which was collected by a Tygon tube (Figure 5.3.1) to a Xevo-G2-XS quadrupole time of flight MS instrument (Waters) in the negative ion mode from 100 to 1000 *m/z* with a bin size of 0.1 *m/z* for approximately 10 s at the rate of 1 Hz. PIRL ablated specimens including muscle, cartilage, cortical bone, trabecular bone and bone cement are shown in Figure 5.3.2. Table 5.3.1 summarizes the number of measurements for each specimen. There were in total 151 measurements and 9000 spectral bins.

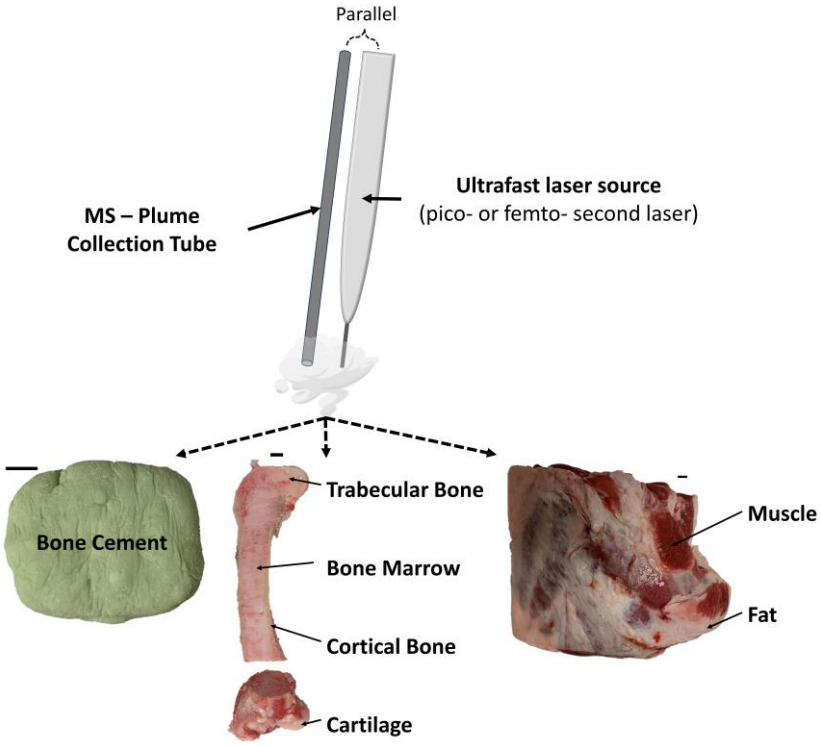


Figure 5.3.1 Schematics of the PIRL-MS collection setup and specimens included for the experiment.

For PIRL-MS analysis, the classification model employed was firstly principal component analysis to reduce data dimensionality and secondly linear discriminant analysis for multi-class classification (PCA-LDA). Cross validation (CV) was performed similarly using 10 splits with 10 repeats generating 100 runs to check for overfitting. No holdout dataset was created because the specimens were intrinsically from one animal subject. All data analysis was performed in the Python Programming Language Version 3.11.5 (Python Software Foundation, https://www.python.org/). Default hyperparameter values were used for all models.

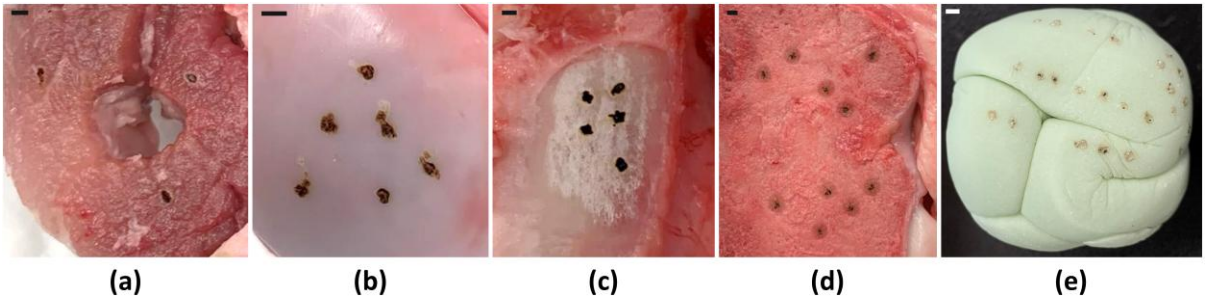


Figure 5.3.2 Specimens post PIRL ablation showing (a) muscle, (b) cartilage, (c) cortical bone, (d) trabecular bone and (e) bone cement.

Table 5.3.1 Summary of the number of PIRL-MS measurements from bone cement, cartilage, cortical bone, muscle and trabecular bone.

Samples	Bone Cement	Cartilage	Cortical Bone	Muscle	Trabecular Bone
Number of Meas.	40	30	29	24	28

5.3.3 Results and Discussion

Figure 5.3.3 shows the preliminary mass spectra averaged over each tissue type for bone cement, cartilage, cortical bone, muscle and trabecular bone. The MS data was normalized by total ion current. Some distinct spectral features could be visualized from the raw spectra. For instance, unique spectral peaks could be seen in the 250 – 350 and 650 – 800 *m/z* regions, which would contribute positively to classification outcomes using PCA-LDA. The fragmentation patterns occurred in the lower *m/z* region (below 350 *m/z*) generally indicated smaller molecule fragments in weight, which were visible for all tissue types as well as bone cement. These line peaks were less informative as they represented smaller fragment pieces that could be found in abundance in different materials. Bone cement, mainly consisted of polymethyl methacrylate (PMMA) polymers, usually produced low mass fragments including hydrocarbons and ester groups as well as H^-, C^-, O^-, and OH^-[294]. For bone tissues, the line peaks between 200 to 500 *m/z* could be derived from a $Ca_{10}(PO_4)_6(OH)_2$ precursor species such as $CA_4PO_6^+$ and $CA_5PO_6^+$[295,296]. The more discriminative features occurred in the higher *m/z* region of which the lines were generated by larger molecules. For the biological tissues, the mass spectral features were primarily produced by molecular ions from phospholipids and peptides in the 500 – 800 *m/z* range, such as collagen, phosphatidylcholine and phosphatidylinositol[297–299], which were the dominant differentiator in the classification task. Figure 5.3.4 illustrates PCA feature extraction for bone cement, cartilage, cortical bone, muscle and trabecular bone. The number of features (*m/z* bins) was reduced from 9000 to 30 PCs, of which the first three

PCs were shown in Figure 5.3.4. The 30 PCs ranked by the percentage of explained variance in the descending order constituted 95.6% total explained variance, where the first 3 PCs accounted for 82.3%. Distinct clusters for individual class labels were observed on the PCA plot. Well-defined separation could be found along the second PC between bone cement and biological tissue types. There were some outliers in the data group of bone cement, which could be seen at a farther distance away from the main cluster. All 30 PCs were utilized for classification using LDA. In addition, to further reduce the number of PCs included in the classification task, optimizations could be performed to select a subset of the 30 PCs, which could give rise to higher or equivalent classification accuracy. This procedure could further lessen the computation burden.

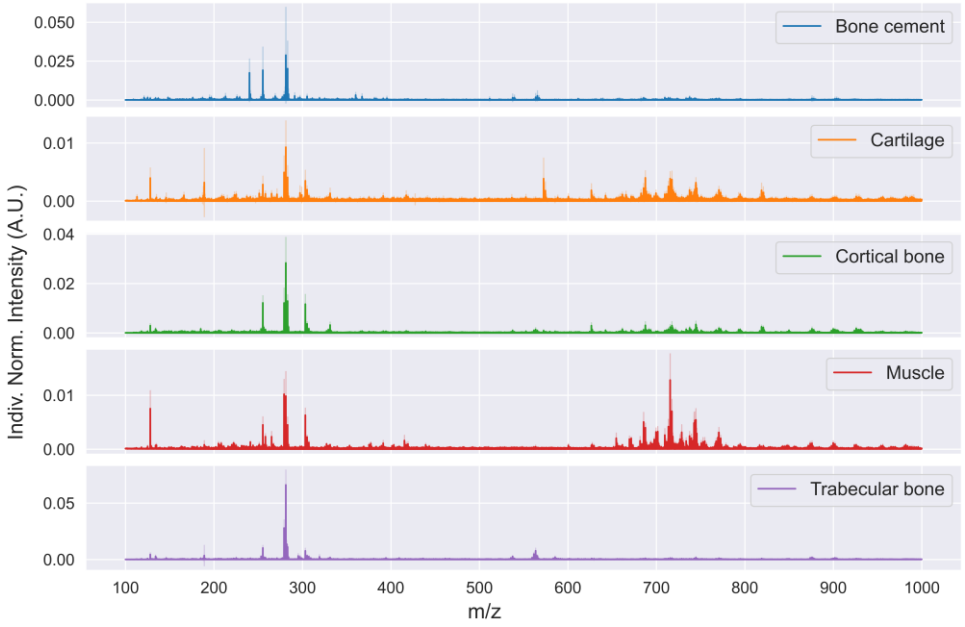


Figure 5.3.3 Preliminary mass spectra averaged over the number of measurements for bone cement, cartilage, cortical bone, muscle and trabecular bone. Signal intensities were normalized by total ion current. Standard deviations were represented by the shaded error bands. Peak annotations were omitted for the sake of clarity.

Figure 5.3.5 shows the confusion matrix for multi-class classification using LDA summed over the 100 runs of CV for bone cement, cartilage, cortical bone, muscle and trabecular bone. Table 5.3.2 summarizes all classification metrics obtained from multi-class classification using LDA, where all values were rounded up to two decimal places. Classification of bone cement from the rest biological tissue types demonstrated 100% in precision, recall and F1 score. The highest misclassification rate was found in trabecular bone versus cortical bone, where there

were 18 instances of trabecular bone being identified as cortical bone. Such an observation was largely in line with expectations due to the similar compositions of the two bone types. In particular, as compared to cortical bone, trabecular bone is of high porosity where the medullary cavities are filled with bone marrow. One of the major differences between the two bones is the lipid and blood content, which could potentially confuse the classification model leading to a slightly lower accuracy score. Multi-class classification using PCA-LDA overall was capable of classifying the 5 groups of MS measurements accurately. Different optimization techniques such as feature selection or oversampling could potentially improve the classification scores; overfitting however needs to be checked before implementing such optimization techniques.

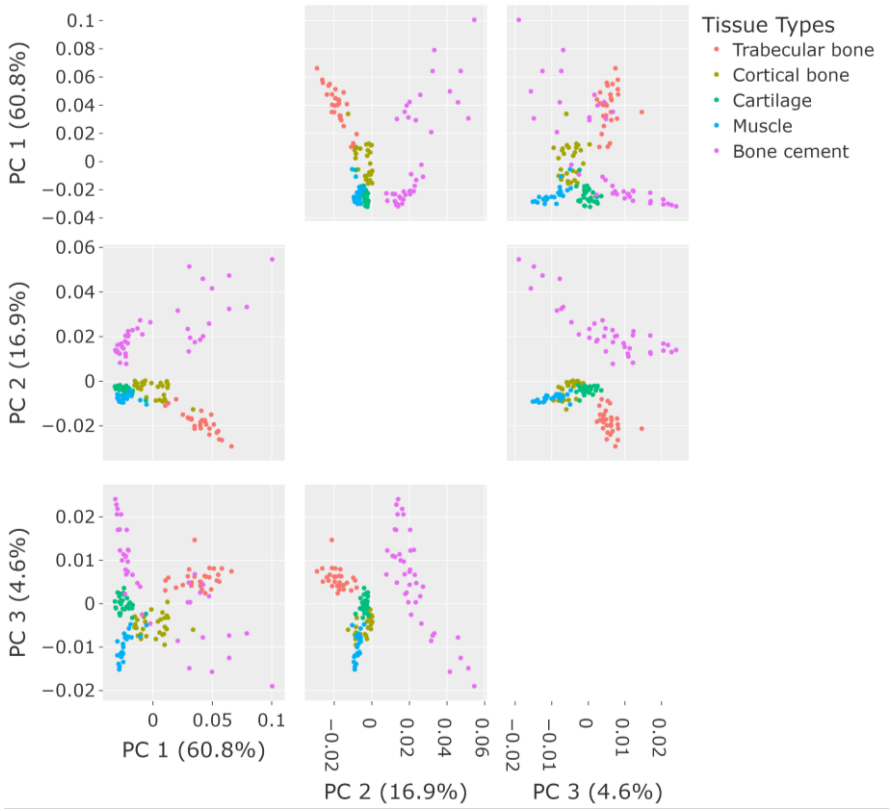


Figure 5.3.4 PCA feature extraction for trabecular bone, cortical bone, cartilage, muscle and bone cement showing the first three PCs.

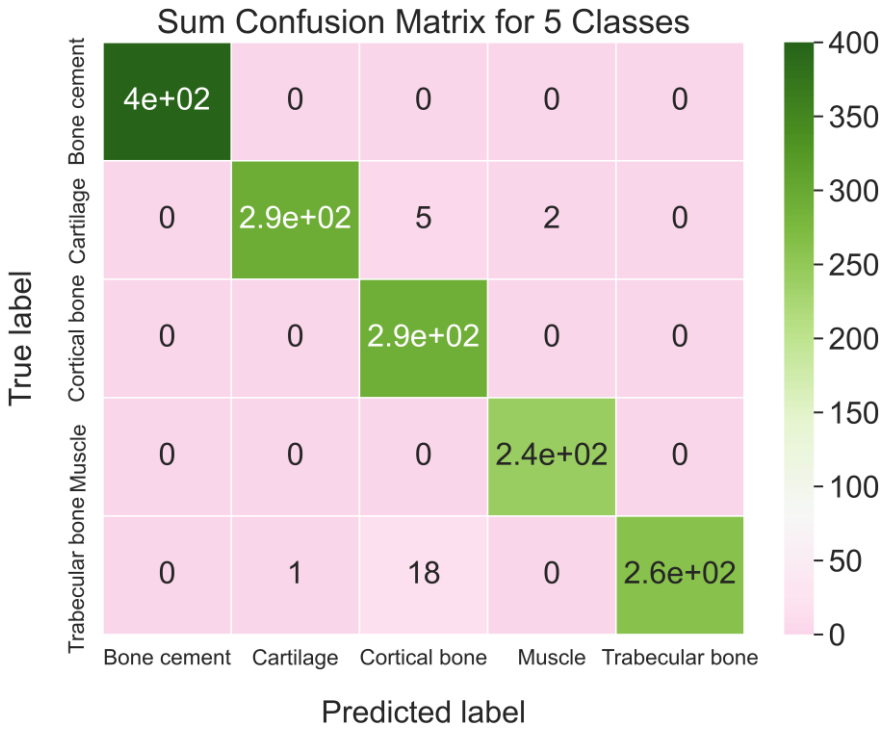


Figure 5.3.5 Confusion matrix for multi-class classification using LDA summed over 100 runs of CV for bone cement, cartilage, cortical bone, muscle and trabecular bone.

Table 5.3.2 Classification report summarizing all metrics including precision, recall, F1 score, support, macro and weighted accuracy scores for multi-class classification using LDA for bone cement, cartilage, cortical bone, muscle and trabecular bone. Values are rounded up to two decimal places.

Mean	**Precision**	**Recall**	**F1 Score**	**Support**
Bone Cement	1.00	1.00	1.00	4.00
Cartilage	1.00 ± 0.03	0.98 ± 0.09	0.98 ± 0.05	3.00
Cortical Bone	0.94 ± 0.12	1.00	0.97 ± 0.07	2.90 ± 0.30
Muscle	0.99 ± 0.05	1.00	1.00 ± 0.03	2.40 ± 0.49
Trabecular Bone	1.00	0.94 ± 0.14	0.96 ± 0.08	2.80 ± 0.40
Accuracy			0.98 ± 0.03	15.10 ± 0.30
Macro Avg	0.99 ± 0.03	0.98 ± 0.03	0.98 ± 0.03	15.10 ± 0.30
Weighted Avg	0.99 ± 0.02	0.98 ± 0.03	0.98 ± 0.03	15.10 ± 0.30

5.3.4 Future studies and Conclusion

This proof-of-concept study has laid the groundwork for the utilization of PIRL-MS measurements to classify tissue types and potentially tissue interfaces in orthopedic surgeries, where the results demonstrated sufficiently high classification accuracy scores. For future studies, the aim is to investigate whether PIRL-MS can offer benefits to other orthopedics-related procedures in general and discover *m/z* features (biomarkers) from PIRL-MS spectra that contribute the most to classification for a particular bone diseases or conditions. The potential applications could include bone tumour margin detection and osteoporosis. Complementarity of PIRL-MS with other optical methods such as Raman spectroscopy or imaging will also be examined to determine whether the multi-modal combination could offer more benefits than single techniques alone with more accurate and precise information for diagnostic purposes.

I would like to express my sincere gratitude to Dr. Brian C. Wilson, Dr. Margarete Akens, Dr. Arash Zarrine-Afsar, Dr. Michael Woolman and Lan Anna Ye at University Health Network for their invaluable support and contributions to this research. This work was also supported by Wrixon Travel Bursary for Research Excellence.

5.4 Discussion and Conclusion of the Thesis

The research presented in this thesis has established groundwork for the integration of optical sensing into surgical tools for bone-related procedures in orthopedics and neurosurgery. Based upon the overall aim, the thesis has successfully evaluated the performance of optical techniques to differentiate common tissue types encountered during bone-related surgeries, developed feature selection frameworks to discover important wavelength features for reduced computational burden, and lastly verified the selected features in *ex vivo* experiments to achieve reduced instrumentation complexity. Furthermore, preliminary investigations on the use of ultrafast lasers have been initiated to demonstrate utility in surgical guidance and possibly ablation. The findings presented in this thesis have directly addressed the research question stated in Chapter 1, further confirming the hypothesis and advancing the research of optical sensing beyond the state-of-the-art by introducing novel analytical frameworks and constructing prototypes. Valuable insights were generated from experiments, offering the opportunity to improve surgical treatments in orthopedics and neurosurgery and thus reducing the financial burden on the healthcare system. During the course, we have also initiated collaborations with other research groups and partners to advance the technology for commercial applications. For future directions, it is envisioned that the probe design will be optimized and assessed in *in vivo* settings for verification. More experiments regarding ultrafast lasers will be performed including the use of ambient mass spectrometry. The molecular compositions of the generated plume will be compared between picosecond and femtosecond laser systems. In summary, the research work combined with machine learning and deep learning techniques is fundamental and will continue providing insights to understanding the knowledge domain for translational and clinical studies.

5.5 Personal and Professional Development – Reflection on the PhD Experience

Threshold concepts are very important ideas in the field of educational research, which have been widely discussed since the publication of the famous paper by Meyer and Land[300]. When I first encountered these principles in pedagogy, I came to the realization that my own learning experience throughout my educational journey could be explained and summarized by this theory. During the past four years, I have embarked on an educational journey filled with rigorous scientific exploration and research in the pursuit of my doctoral degree of Engineering

Science specialized in the field of Biophotonics at University College Cork, Cork, Ireland. As my Ph.D. study is approaching its completion, it is favorable for myself to start reflecting on my learning experience together with challenges and growths along the way.

Upon retrospective consideration, I have gone through different personal learning phases; in particular, secondary school – the phase where efforts were seemingly not needed to achieve good grades; undergraduate study – the phase where basic knowledge suddenly became difficult to grasp with so much struggle to pass each class; Masters and Ph.D. – the stage where integration of accumulated knowledge and experiences took place during the course, resulting in enhanced critical thinking and problem solving skills. I often think back and reflect on my own memories: What happened during higher education that led me to cross, as described by Perkins[301], from a pre-liminal to a liminal to a post-liminal space, allowing me to gain transformative understanding of learning? Will I be able to conclude some useful advice and patterns for my future career? To this end, the role of self-directed learning objectives in crossing threshold concepts must have contributed significantly to the outcome. To be more specific, what would be an effective approach to set up achievable learning objectives and how should learning progress be assessed? How should I prepare and motivate myself for foreseeable improvement and success? Perhaps the answers could be found from the following experiences.

When I first started the Ph.D. program, I was very excited for new things – new projects, new challenges, new people, and new environments. I was eager to establish myself for the new role. However, just two months later when COVID-19 pandemic hit, I was only able to familiarize myself with the new environment. A substantial amount of time and effort was then spent adjusting to a new norm, where I needed to become significantly more self-motivated to formulate a working routine so that I could stay on track with my own study. This was an unprecedented challenge both mentally and physically at the moment due to experiencing a lockdown for the first time. On the bright side, I was able to acquire important skills of being effectively self-oriented and self-directed given the circumstances that support from my team members was nearly impossible. I eventually managed to adhere to a regular daily schedule (with noticeable procrastination at the beginning) focusing on the key tasks that I aimed to complete by a deadline. Repeated practice also played a crucial role in my personal development. I found that, for myself, repetition served as the fundamental building blocks of the greater comprehension, which also ensured the quality of my work. Just like linking stars

in the sky to form constellations, I was able to slowly integrate physical concepts together and reform my way of thinking subconsciously in the background. To this date, I still maintain this mindset in research. I believe that self-directed learning through setting up specific objectives enables myself and perhaps other learners to assess their personal strengths and weaknesses in particular disciplines, ultimately boosting the crossing of threshold concepts, especially in the context of COVID-19 when isolation was inevitable, personal flow of study could still be maintained without interruption. After all, if there is a will there is a way. Self-directedness is like the will; the key is how to find, initiate and grow fruits from it.

To continue the interrogation of my personal and professional development during my Ph.D. study, I would like to reflect on my learning experience to address a potentially effective approach to achieve objectives and assess progress. My motivation stemmed from personal reflections of my own learning experiences from different stages of life, in which realization of the importance of threshold concepts in each discipline had a pivotal impact. In particular, when I looked at my Ph.D. learning journey retrospectively with experiences that even went back to high school, I successfully crossed some learning thresholds in the discipline each time I 'leveled up' with a degree. Identifying the very threshold concepts that helped me with knowledge enhancement became very easy from recollection. However, foreseeing such learning obstacles/challenges was certainly difficult for me by only conducting self-reflections at the moment when I was still 'sailing' in the process, as there had not been previous personal experiences for me to refer to. To me personally, professional growth was gained by directly accepting challenges and actively looking for solutions. For instance, after I was acclimated to working from home, I sought out opportunities by accepting a manuscript invitation and contributed a review article to the journal *Applied Sciences*. This was my first published work for my Ph.D., which significantly boosted my confidence as a researcher. Furthermore, I was also committed to improving relevant skills. My Ph.D. research fell under the project theme that targeted at surgical guidance for procedures involving brain or bone. Establishing collaborative relationships was critical because my work could be seen as three-fold involving aspects of clinical, engineering and data science expertise. I was able to foster such collaborations and generate interesting research questions, during which I gained new knowledge, developed a deeper understanding of the complexities of scientific research, and attained a greater appreciation of personal perseverance.

Threshold concepts, surprisingly controversial, can be summarized using five specific criteria, which are transformative, irreversible, integrative, bounded and troublesome[300]. It can be related to, by definition, “akin to a portal, opening up a new and previously inaccessible way of thinking about something. It represents a transformed way of understanding, or interpreting, or viewing something without which the learner cannot progress. As a consequence of comprehending a threshold concept there may thus be a transformed internal view of subject matter, subject landscape, or even world view”. However, there have been many criticisms over the past years due to vagueness of the theory definition together with the lack of empirical supporting evidence, and therefore threshold concept is a scientific dead end[302]. I am not here to defend or argue against the claims; instead, my experience during the Ph.D. study resonates with the theory and I would like to share my strategies based on my own perspectives. Some of the key evidence that signals learning improvement and success upon reflection would be based on the threshold concept theory: Have I recognized or developed an instinct to recognize the difference between the last versus the current phase of a project (transformative in perception)? Will I be able to adapt the new method from the last study phase (irreversible)? Am I able to transition smoothly to a new project (troublesome)? Will I be able to discover the links between different learning experiences and thus gain some knowledge boosters (integrative)? Are there specific understandings of concepts required to gain entry to a discipline-specific project (bounded)? Will I establish connections between new information and my own way of reasoning (discursive)? Would the learning eventually help me build bridges and cross disciplinary boundaries (reconstitutive)? These are the important questions to ask during the process to track my progress and confirm achievements. Fortunately, it is satisfying to report that my answers to the above questions are “YES” as I near the completion of my doctoral degree.

Regardless of success, setbacks, fulfillments or frustrations, I have learned valuable life lessons by navigating through the learning process. For my future endeavors, the skills that I gained from my Ph.D. study will serve me well, either in academia or industry. I really appreciate the opportunities, support, and mentorship I have received during the past four years, and I am ready for the next chapter of my life with enthusiasm and optimism through my dedication to lifelong learning.

References

1. Fingar KR, Stocks C, Weiss AJ, Steiner CA. Most frequent operating room procedures performed in US Hospitals, 2003–2012. In: *Healthcare Cost and Utilization Project (HCUP) Statistical Briefs #186*. Agency for Healthcare Research and Quality (US); 2014. Accessed August 29, 2023. https://hcup-us.ahrq.gov/reports/statbriefs/sb186-Operating-Room-Procedures-United-States-2012.jsp

2. McDermott KW, Ph D, Liang L, Ph D. Overview of Operating Room Procedures During Inpatient Stays in U.S. Hospitals, 2018. Healthcare Cost and Utilization Project (HCUP) Statistical Briefs [Internet]. 2021. https://hcup-us.ahrq.gov/reports/statbriefs/sb281-Operating-Room-Procedures-During-Hospitalization-2018.jsp

3. Varacallo M, Luo TD, Johanson NA. Total Knee Arthroplasty Techniques. In: *StatPearls [Internet]*. StatPearls Publishing; 2023. Accessed February 25, 2024. https://www.ncbi.nlm.nih.gov/books/NBK499896/

4. Varacallo M, Luo TD, Johanson NA. Total Hip Arthroplasty Techniques. In: *StatPearls [Internet]*. StatPearls Publishing; 2023. Accessed February 25, 2024. https://www.ncbi.nlm.nih.gov/books/NBK507864/

5. Reisener MJ, Pumberger M, Shue J, Girardi FP, Hughes AP. Trends in lumbar spinal fusion—a literature review. *Journal of Spine Surgery*. 2020;6(4):752-776. doi:10.21037/jss-20-492

6. Alkhaibary A, Alharbi A, Alnefaie N, Oqalaa Almubarak A, Aloraidi A, Khairy S. Cranioplasty: A Comprehensive Review of the History, Materials, Surgical Aspects, and Complications. *World Neurosurg*. 2020;139:445-452. doi:10.1016/j.wneu.2020.04.211

7. Fernández-de Thomas RJ, Munakomi S, De Jesus O. Craniotomy. In: *StatPearls [Internet]*. StatPearls Publishing; 2023. Accessed February 26, 2024. https://www.ncbi.nlm.nih.gov/books/NBK560922/

8. Rao D, Le RT, Fiester P, Patel J, Rahmathulla G. An Illustrative Review of Common Modern Craniotomies. *J Clin Imaging Sci*. 2020;10. doi:10.25259/JCIS_176_2020

9. Rangankar V, Singh A, Khaladkar S. Pictorial review of the post-operative cranium. *South African Journal of Radiology*. 2023;27(1). doi:10.4102/sajr.v27i1.2684

10. Lee SM, Shin WC, Woo SH, Kim TW, Kim DH, Suh KT. Hip arthroplasty for patients with chronic renal failure on dialysis. *Sci Rep*. 2023;13(1). doi:10.1038/s41598-023-30283-x

11. Yamada M, Nakajima A, Sonobe M, et al. The impact of postoperative inclination of the joint line on clinical outcomes in total knee arthroplasty using a prosthesis with anatomical geometry. *Sci Rep*. 2023;13(1). doi:10.1038/s41598-023-28182-2

12. Qin R, Wu T, Liu H, Zhou B, Zhou P, Zhang X. Minimally invasive versus traditional open transforaminal lumbar interbody fusion for the treatment of low-grade degenerative spondylolisthesis: a retrospective study. *Sci Rep*. 2020;10(1). doi:10.1038/s41598-020-78984-x

13. Dahdaleh NS, Smith ZA, Hitchon PW. Percutaneous Pedicle Screw Fixation for Thoracolumbar Fractures. *Neurosurgery Clinics of NA*. 2014;25(2):337-346. doi:10.1016/j.nec.2013.12.011

14. Kim TT, Johnson JP, Pashman R, Drazin D. Minimally Invasive Spinal Surgery with Intraoperative Image-Guided Navigation. *Biomed Res Int*. 2016;2016. doi:10.1155/2016/5716235

15. Brismar BH, Hallert O, Tedhamre A, Lindgren JU. Early gain in pain reduction and hip function, but more complications following the direct anterior minimally invasive approach for total hip arthroplasty: a randomized trial of 100 patients with 5 years of follow up. *Acta Orthop*. 2018;89(5):484-489. doi:10.1080/17453674.2018.1504505

16. Migliorini F, Biagini M, Rath B, Meisen N, Tingart M, Eschweiler J. Total hip arthroplasty: minimally invasive surgery or not? Meta-analysis of clinical trials. *Int Orthop*. 2019;43(7):1573-1582. doi:10.1007/s00264-018-4124-3

17. Allahabadi S, Cheung EC, Hodax JD, Feeley BT, Ma CB, Lansdown DA. Outpatient Shoulder Arthroplasty—A Systematic Review. *J Shoulder Elb Arthroplast*. 2021;5:1-19. doi:10.1177/24715492211028025

18. Cordemans V, Kaminski L, Banse X, Francq BG, Detrembleur C, Cartiaux O. Pedicle screw insertion accuracy in terms of breach and reposition using a new intraoperative cone beam computed tomography imaging technique and evaluation of the factors associated with these parameters of accuracy: a series of 695 screws. *European Spine Journal*. 2017;26(11):2917-2926. doi:10.1007/s00586-017-5195-3

19. Chiu RG, Patel S, Zhu A, Aguilar E, Mehta AI. Endoscopic Versus Open Laminectomy for Lumbar Spinal Stenosis: An International, Multi-Institutional Analysis of Outcomes and Adverse Events. *Global Spine J*. 2020;10(6):720-728. doi:10.1177/2192568219872157

20. Nayar G, Blizzard DJ, Wang TY, et al. Pedicle screw placement accuracy using ultra-low radiation imaging with image enhancement versus conventional fluoroscopy in minimally invasive transforaminal lumbar interbody fusion: An internally randomized controlled trial. *J Neurosurg Spine*. 2018;28(2):186-193. doi:10.3171/2017.5.SPINE17123

21. Paczesny Ł, Lorkowski M, Pielak T, Wójcicki R, Huri G, Zabrzyński J. The Role of Ultrasound Guidance in Mini-Invasive Musculoskeletal Surgery—A Pictorial Essay. *Applied Sciences*. 2023;13(19):10900. doi:10.3390/app131910900

22. Kleck CJ, Johnson C, Akiyama M, Burger EL, Cain CJ, Patel V V. One-step minimally invasive pedicle screw instrumentation using o-arm and stealth navigation. *Clin Spine Surg*. 2018;31(5):197-202. doi:10.1097/BSD.0000000000000616

23. St Mart JP, Goh EL, Shah Z. Robotics in total hip arthroplasty: a review of the evolution, application and evidence base. *EFORT Open Rev*. 2020;5(12):866-873. doi:10.1302/2058-5241.5.200037

24. Patel MR, Jacob KC, Parsons AW, et al. Systematic Review: Applications of Intraoperative Ultrasonography in Spinal Surgery. *World Neurosurg*. 2022;164:e45-e58. doi:10.1016/j.wneu.2022.02.130

25. Yanni DS, Ozgur BM, Louis RG, et al. Real-time navigation guidance with intraoperative CT imaging for pedicle screw placement using an augmented reality head-

mounted display: a proof-of-concept study. *Neurosurg Focus*. 2021;51(2):E11. doi:10.3171/2021.5.FOCUS21209

26. Navarro-Ramirez R, Lang G, Lian X, et al. Total Navigation in Spine Surgery; A Concise Guide to Eliminate Fluoroscopy Using a Portable Intraoperative Computed Tomography 3-Dimensional Navigation System. *World Neurosurg*. 2017;100:325-335. doi:10.1016/j.wneu.2017.01.025

27. Chaudhry FA, Ismail SZ, Davis ET. A new system of computer-assisted navigation leading to reduction in operating time in uncemented total hip replacement in a matched population. *European Journal of Orthopaedic Surgery & Traumatology*. 2018;28(4):645-648. doi:10.1007/s00590-018-2133-y

28. Fisher C, Harty J, Yee A, et al. Perspective on the integration of optical sensing into orthopedic surgical devices. *J Biomed Opt*. 2022;27(01):010601. doi:10.1117/1.JBO.27.1.010601

29. Simmons EL. Diffuse reflectance spectroscopy: a comparison of the theories. *Appl Opt*. 1975;14(6):1380. doi:10.1364/AO.14.001380

30. Kortüm G, Braun W, Herzog G. Principles and Techniques of Diffuse-Reflectance Spectroscopy. *Angewandte Chemie International Edition in English*. 1963;2(7):333-341. doi:10.1002/anie.196303331

31. Tuchin V V. Tissue Optics and Photonics: Biological Tissue Structures. *J Biomed Photonics Eng*. 2015;1(1):3-21. doi:10.18287/JBPE-2015-1-1-3

32. Martins IS, Silva HF, Lazareva EN, et al. Measurement of tissue optical properties in a wide spectral range: a review [Invited]. *Biomed Opt Express*. 2023;14(1):249. doi:10.1364/BOE.479320

33. Dinish US, Wong CL, Sriram S, et al. Diffuse Optical Spectroscopy and Imaging to Detect and Quantify Adipose Tissue Browning. *Sci Rep*. 2017;7(1):41357. doi:10.1038/srep41357

34. Konugolu Venkata Sekar S, Lanka P, Farina A, et al. Broadband Time Domain Diffuse Optical Reflectance Spectroscopy: A Review of Systems, Methods, and Applications. *Applied Sciences*. 2019;9(24):5465. doi:10.3390/app9245465

35. Cuccia DJ, Bevilacqua F, Durkin AJ, Ayers FR, Tromberg BJ. Quantitation and mapping of tissue optical properties using modulated imaging. *J Biomed Opt*. 2009;14(2):024012. doi:10.1117/1.3088140

36. Kitsmiller VJ, Dummer MM, Johnson K, Cole GD, O'Sullivan TD. Frequency domain diffuse optical spectroscopy with a near-infrared tunable vertical cavity surface emitting laser. *Opt Express*. 2018;26(16):21033. doi:10.1364/oe.26.021033

37. Nazarian S, Gkouzionis I, Murphy J, et al. Real-time classification of tumour and non-tumour tissue in colorectal cancer using diffuse reflectance spectroscopy and neural networks to aid margin assessment. *International Journal of Surgery*. Published online January 22, 2024. doi:10.1097/JS9.0000000000001102

38. Geldof F, Schrage YM, van Houdt WJ, Sterenborg HJCM, Dashtbozorg B, Ruers TJM. Toward the use of diffuse reflection spectroscopy for intra-operative tissue discrimination during sarcoma surgery. *J Biomed Opt*. 2024;29(02). doi:10.1117/1.JBO.29.2.027001

39. Surkov YI, Serebryakova IA, Kuzinova YK, et al. Multimodal Method for Differentiating Various Clinical Forms of Basal Cell Carcinoma and Benign Neoplasms In Vivo. *Diagnostics*. 2024;14(2):202. doi:10.3390/diagnostics14020202

40. Sánchez-Ramos LL, Morales-Cruzado B, Pérez-Gutiérrez FG. Determination of tissue oxygen saturation by diffuse reflectance spectroscopy. *J Biomed Opt*. 2023;28(09). doi:10.1117/1.JBO.28.9.095002

41. Godavarty A, Leiva K, Amadi N, Klonoff DC, Armstrong DG. Diabetic Foot Ulcer Imaging: An Overview and Future Directions. *J Diabetes Sci Technol*. 2023;17(6):1662-1675. doi:10.1177/19322968231187660

42. Arista Romeu EJ, Escobedo G, Campos-Espinosa A, et al. Diffuse reflectance spectroscopy accurately discriminates early and advanced grades of fatty liver in mice. *J Biomed Opt*. 2018;23(11):1. doi:10.1117/1.jbo.23.11.115005

43. Chen CT, Tseng SH, Sung BH, Chen YY, Cheng HC. Noninvasive transcutaneous bilirubin measurement in adults using skin diffuse reflectance. *Biomed Opt Express*. 2023;14(10):5405. doi:10.1364/BOE.500833

44. Minakawa M, Wares MdA, Nakano K, et al. Measuring and imaging of transcutaneous bilirubin, hemoglobin, and melanin based on diffuse reflectance spectroscopy. *J Biomed Opt*. 2023;28(10). doi:10.1117/1.JBO.28.10.107001

45. Li CL, Fisher CJ, Burke R, Andersson-Engels S. Orthopedics-Related Applications of Ultrafast Laser and Its Recent Advances. *Applied Sciences*. 2022;12(8):3957. doi:10.3390/app12083957

46. Gunaratne GDR, Khan R, Fick D, Robertson B, Dahotre N, Ironside C. A review of the physiological and histological effects of laser osteotomy. *J Med Eng Technol*. 2017;41(1):1-12. doi:10.1080/03091902.2016.1199743

47. Sotsuka Y, Nishimoto S, Tsumano T, et al. The dawn of computer-assisted robotic osteotomy with ytterbium-doped fiber laser. *Lasers Med Sci*. 2014;29:1125-1129. doi:10.1007/s10103-013-1487-y

48. Stübinger S, Ghanaati S, Saldamli B, Kirkpatrick CJ, Sader R. Er:YAG Laser Osteotomy: Preliminary Clinical and Histological Results of a New Technique for Contact-Free Bone Surgery. *Eur Surg Res*. 2009;42:150-156. doi:10.1159/000197216

49. Asnaashari M, Zadsirjan S. Application of Laser in Oral Surgery. *J Lasers Med Sci*. 2014;5(3):97-107.

50. Parker S, Cronshaw M, Anagnostaki E, Mylona V, Lynch E, Grootveld M. Current Concepts of Laser–Oral Tissue Interaction. *Dent J (Basel)*. 2020;8(3):61. doi:10.3390/dj8030061

51. Davoudi A, Amrolahi M, Khaki H. Effects of laser therapy on patients who underwent rapid maxillary expansion; a systematic review. *Lasers Med Sci*. 2018;33:1387-1395. doi:10.1007/s10103-018-2545-2

52. Radcliff K, Vaccaro AR, Hilibrand A, Schroeder GD. Lasers in Spine Surgery. *Journal of the American Academy of Orthopaedic Surgeons*. 2019;27(17):621-632. doi:10.5435/JAAOS-D-18-00001

53. Ahn Y, Lee U. Use of lasers in minimally invasive spine surgery. *Expert Rev Med Devices*. 2018;15(6):423-433. doi:10.1080/17434440.2018.1483236

54. Kong X, Wakida NM, Yokomori K. Application of Laser Microirradiation in the Investigations of Cellular Responses to DNA Damage. *Frontiers in Phy*. 2021;8:1-8. doi:10.3389/fphy.2020.597866

55. Miller PR, Aggarwal R, Doraiswamy A, Lin YJ, Lee YS, Narayan RJ. Laser Micromachining for Biomedical Applications. *JOM*. 2009;61(9):35-40. doi:10.1007/s11837-009-0130-7

56. Krueger A. Ultrafast lasers in biophotonics. In: *Multiphoton Microscopy and Fluorescence Lifetime Imaging*. De Gruyter; 2018. doi:https://doi.org/10.1515/9783110429985-006

57. Tzanakakis EGC, Skoulas E, Pepelassi E, Koidis P, Tzoutzas IG. The Use of Lasers in Dental Materials: A Review. *Materials*. 2021;14(12):3370. doi:10.3390/ma14123370

58. Petrov T, Pecheva E, Walmsley AD, Dimov S. Femtosecond laser ablation of dentin and enamel for fast and more precise dental cavity preparation. *Materials Science & Engineering C*. 2018;90:433-438. doi:10.1016/j.msec.2018.04.070

59. Luengo MCL, Portillo M, Sánchez JM, et al. Evaluation of micromorphological changes in tooth enamel after mechanical and ultrafast laser preparation of surface cavities. *Lasers Med Sci*. 2013;28:267-273. doi:10.1007/s10103-012-1144-x

60. Chen H, Li H, Sun YC, Wang Y, Lü PJ. Femtosecond laser for cavity preparation in enamel and dentin: ablation efficiency related factors. *Sci Rep*. 2016;6:1-8. doi:10.1038/srep20950

61. Pantawane M V, Dahotre NB. Challenges and Advances in Osteotomy. *Annals of Bone and Joint Surgery*. 2019;2(1):1-4. doi:10.6084/m9.figshare.8216621

62. Troedhan A, Mahomund ZT, Wainwright M, Khamis MM. Cutting bone with drills, burs, lasers and piezotomes: A comprehensive systematic review and recommendations for the clinician. *International Journal of Oral and Craniofacial Science*. 2017;3(2):20-33. doi:10.17352/2455-4634.000028

63. Azadgoli B, Baker RY. Laser applications in surgery. *Ann Transl Med*. 2016;4(23):1-7. doi:10.21037/atm.2016.11.51

64. Khalkhal E, Rezaei-Tavirani M, Zali MR, Akbari Z. The evaluation of laser application in surgery: a review article. *J Lasers Med Sci*. 2019;10(Suppl 1):S104-S111. doi:10.15171/jlms.2019.S18

65. Hoy CL, Ferhanoğlu O, Yildirim M, et al. Clinical ultrafast laser surgery: Recent advances and future directions. *IEEE Journal on Selected Topics in Quantum Electronics*. 2014;20(2):7100814. doi:10.1109/JSTQE.2013.2287098

66. Bernal LMB, Canbaz F, Droneau A, Friederich NF, Cattin PC, Zam A. Optimizing deep bone ablation by means of a microsecond Er:YAG laser and a novel water microjet irrigation system. *Biomed Opt Express*. 2020;11(12):7253-7272. doi:10.1364/boe.408914

67. Nuss RC, Fabian RL, Sarkar R, Puliafito CA. Infrared laser bone ablation. *Lasers Surg Med*. 1988;8(4):381-391. doi:10.1002/lsm.1900080408

68. Lee CL, Roberts C, Litsky AS. Laser Ablation of Dyed Acrylic Bone Cement. *Lasers Surg Med*. 1997;20(3):280-289. doi:10.1002/(SICI)1096-9101(1997)20:3<280::AID-LSM7>3.0.CO;2-M

69. Ivanenko M, Werner M, Afilal S, Klasing M, Hering P. Ablation of hard bone tissue with pulsed CO2 lasers. *Medical Laser Application*. 2005;20:13-23. doi:10.1016/j.mla.2005.02.007

70. Carr CW, Radousky HB, Demos SG. Wavelength dependence of laser-induced damage: Determining the damage initiation mechanisms. *Phys Rev Lett*. 2003;91(12):1-4. doi:10.1103/PhysRevLett.91.127402

71. Kohli V, Elezzabi AY, Acker JP. Cell Nanosurgery Using Ultrashort (Femtosecond) Laser Pulses: Applications to Membrane Surgery and Cell Isolation. *Lasers Surg Med*. 2005;37(3):227-230. doi:10.1002/lsm.20220

72. Marion II JE, Kim BM. Medical applications of ultra-short pulse lasers. *Proc SPIE 3616, Commercial and Biomedical Applications of Ultrafast Lasers*. 1999;3616. doi:10.1117/12.351839

73. Vogel A, Venugopalan V. Mechanisms of Pulsed Laser Ablation of Biological Tissues. *Chem Rev*. 2003;103:577-644. doi:10.1021/cr010379n

74. Sheetz KE, Squier J. Ultrafast optics: Imaging and manipulating biological systems. *J Appl Phys*. 2009;105:051101. doi:10.1063/1.3081635

75. Cangueiro LT, Le Quang T, Vilar R. Laser surface modification of biological hard tissues. In: *Laser Surface Modification of Biomaterials: Techniques and Applications*. Elsevier Ltd; 2016:221-251. doi:10.1016/B978-0-08-100883-6.00008-3

76. Isobe K, Watanabe W, Itoh K. Ultrafast Laser Surgery. In: *Functional Imaging by Controlled Nonlinear Optical Phenomena*. ; 2013:660-688.

77. Jeong DC, Tsai PS, Kleinfeld D. Prospect for feedback guided surgery with ultra-short pulsed laser light. *Curr Opin Neurobiol*. 2012;22(1):24-33. doi:10.1016/j.conb.2011.10.020

78. Vogel A, Noack J, Hüttman G, Paltauf G. Mechanisms of femtosecond laser nanosurgery of cells and tissues. *Appl Phys B*. 2005;81:1015-1047. doi:10.1007/s00340-005-2036-6

79. Domke M, Wick S, Laible M, Rapp S, Huber HP, Sroka R. Ultrafast dynamics of hard tissue ablation using femtosecond-lasers. *J Biophotonics*. 2018;11(10):e201700373. doi:10.1002/jbio.201700373

80. Wieger V, Zoppel S, Wintner E. Ultrashort Pulse Laser Osteotomy. *Laser Phys*. 2007;17(4):438-442. doi:10.1134/s1054660x07040202

81. Armstrong WB, Neev JA, Da Silva LB, Rubenchik AM, Stuart BC. Ultrashort Pulse Laser Ossicular Ablation and Stapedotomy in Cadaveric Bone. *Lasers Surg Med*. 2002;30(3):216-220. doi:10.1002/lsm.10034

82. Strassl M, Wieger V, Brodoceanu D, Beer F, Moritz A, Wintner E. Ultra-short pulse laser ablation of biological hard tissue and biocompatibles. *Journal of Laser Micro/ Nanoengineering*. 2008;3(1):30-40. doi:10.2961/jlmn.2008.01.0007

83. Liu Y, Niemz M. Ablation of femural bone with femtosecond laser pulses—a feasibility study. *Lasers Med Sci*. 2007;22:171-174. doi:10.1007/s10103-006-0424-8

84. Girard B, Yu D, Armstrong MR, Wilson BC, Clokie CML, Miller RJD. Effects of femtosecond laser irradiation on osseous tissues. *Lasers Surg Med*. 2007;39(3):273-285. doi:10.1002/lsm.20466

85. Mccaughey RG, Sun H, Rothholtz VS, Juhasz T, Wong BJF. Femtosecond laser ablation of the stapes. *J Biomed Opt*. 2009;14(2):024040. doi:10.1117/1.3120490

86. Subramanian K, Andrus L, Pawlowski M, Wang Y, Tkaczyk T, Ben-Yakar A. Ultrafast laser surgery probe with a calcium fluoride miniaturized objective for bone ablation. *Biomed Opt Express*. 2021;12(8):4779. doi:10.1364/boe.426149

87. Zhang J, Guan K, Zhang Z, Guan Y. In vitro evaluation of ultrafast laser drilling large-size holes on sheepshank bone. *Opt Express*. 2020;28(17):25528. doi:10.1364/oe.396727

88. An R, Khadar GW, Wilk EI, et al. Ultrafast laser ablation and machining large-size structures on porcine bone. *J Biomed Opt*. 2013;18(7):070504. doi:10.1117/1.jbo.18.7.070504

89. Gemini L, Al-Bourgol S, Machinet G, Bakkali A, Fauçon M, Kling R. Ablation of bone tissue by femtosecond laser: A path to high-resolution bone surgery. *Materials*. 2021;14(9):1-13. doi:10.3390/ma14092429

90. Plötz C, Schelle F, Bourauel C, Frentzen M, Meister J. Ablation of porcine bone tissue with an ultrashort pulsed laser (USPL) system. *Lasers Med Sci*. 2014;30:977-983. doi:10.1007/s10103-014-1520-9

91. Kramer T, Remund S, Jäggi B, Schmid M, Neuenschwander B. Ablation dynamics – from absorption to heat accumulation/ultra-fast laser matter interaction. *Advanced Optical Technologies*. 2018;7(3):129-144. doi:10.1515/aot-2018-0010

92. Aljekhedab F, Zhang W, Haugen HK, Wohl GR, El-Desouki MM, Fang Q. Influence of environmental conditions in bovine bone ablation by ultrafast laser. *J Biophotonics*. 2019;12(6):1-10. doi:10.1002/jbio.201800293

93. Ashforth SA, Oosterbeek RN, Bodley OLC, Mohr C, Aguergaray C, Simpson MC. Femtosecond lasers for high-precision orthopedic surgery. *Lasers Med Sci*. 2020;35(6):1263-1270. doi:10.1007/s10103-019-02899-x

94. Emigh B, An R, Hsu EM, et al. Porcine cortical bone ablation by ultrashort pulsed laser irradiation. *J Biomed Opt*. 2012;17(2):028001. doi:10.1117/1.JBO.17.2.028001

95. Kim B min, Feit MD, Rubenchik AM, et al. Effects of high repetition rate and beam size on hard tissue damage due to subpicosecond laser pulses. *Appl Phys Lett*. 2000;76(26):4001-4003. doi:10.1063/1.1654764

96. Tulea C alexander, Caron J, Gehlich N, Lenenbach A, Noll R, Loosen P. Laser cutting of bone tissue under bulk water with a pulsed ps-laser at 532 nm. *J Biomed Opt*. 2015;20(10):105004. doi:10.1117/1.JBO.20.10.105007

97. Mannion PT, Magee J, Coyne E, O'Connor GM, Glynn TJ. The effect of damage accumulation behaviour on ablation thresholds and damage morphology in ultrafast laser micro-machining of common metals in air. *Appl Surf Sci*. 2004;233(1-4):275-287. doi:10.1016/j.apsusc.2004.03.229

98. Ben-yakar A, Byer RL, Byer RL. Femtosecond laser ablation properties of borosilicate glass. *J Appl Phys*. 2004;96(9):5316-5323. doi:10.1063/1.1787145

99. Liu JM. Simple technique for measurements of pulsed Gaussian-beam spot sizes. *Opt Lett*. 1982;7(5):196-198. doi:10.1364/OL.7.000196

100. Cangueiro LT, Vilar R, Botelho do Rego AM, Muralha VSF. Femtosecond laser ablation of bovine cortical bone. *J Biomed Opt*. 2012;17(12):125005. doi:10.1117/1.JBO.17.12.125005

101. Mortensen LJ, Alt C, Turcotte R, et al. Femtosecond laser bone ablation with a high repetition rate fiber laser source. *Biomed Opt Express*. 2015;6(1):32-42. doi:10.1364/boe.6.000032

102. Lo DD, Mackanos MA, Chung MT, et al. Femtosecond Plasma Mediated Laser Ablation Has Advantages Over Mechanical Osteotomy of Cranial Bone. *Lasers Surg Med*. 2012;44(10):805-814. doi:10.1002/lsm.22098

103. Nicolodelli G, de Fátima Zanirato Lizarelli R, Bagnato VS. Influence of effective number of pulses on the morphological structure of teeth and bovine femur after femtosecond laser ablation. *J Biomed Opt*. 2012;17(4):048001. doi:10.1117/1.JBO.17.4.048001

104. Nguyen J, Ferdman J, Zhao M, et al. Sub-Surface, Micrometer-Scale Incisions Produced in Rodent Cortex using Tightly-Focused Femtosecond Laser Pulses. *Lasers Surg Med*. 2011;43(5):382-391. doi:10.1002/lsm.21054

105. Jee Y, Becker MF, Walser RM. Laser-induced damage on single-crystal metal surfaces. *Journal of the Optical Society of America B*. 1988;5(3):648-659. doi:10.1364/JOSAB.5.000648

106. Lim YC, Altman KJ, Farson DF, Flores KM. Micropillar fabrication on bovine cortical bone by direct-write femtosecond laser ablation. *J Biomed Opt*. 2009;14(6):064021. doi:10.1117/1.3268444

107. Marjoribanks RS, Dille C, Schoenly JE, et al. Ablation and thermal effects in treatment of hard and soft materials and biotissues using ultrafast-laser pulse-train bursts. *Photonics Lasers Med*. 2012;1(3):155-169. doi:10.1515/plm-2012-0020

108. Rosenfeld A, Lorenz M, Stoian R, Ashkenasi D. Ultrashort-laser-pulse damage threshold of transparent materials and the role of incubation. *Applied Physics A*. 1999;69:S373–S376. doi:10.1007/s003399900237

109. Su E, Sun H, Juhasz T, Wong BJF. Preclinical investigations of articular cartilage ablation with femtosecond and pulsed infrared lasers as an alternative to microfracture surgery. *J Biomed Opt*. 2014;19(9):098001. doi:10.1117/1.jbo.19.9.098001

110. Livermore L, B PO. Laser-Induced Damage in Dielectrics with Nanosecond to Subpicosecond Pulses. *Phys Rev Lett*. 1995;74(12):2248-2251. doi:10.1103/PhysRevLett.74.2248

111. Lee YM, Tu RY, Chiang AC, Huang YC. Average-power mediated ultrafast laser osteotomy using a mode-locked Nd:YVO4 laser oscillator. *J Biomed Opt*. 2007;12(6):060505. doi:10.1117/1.2821149

112. Daskalova A, Bashir S, Husinsky W. Morphology of ablation craters generated by ultra-short laser pulses in dentin surfaces: AFM and ESEM evaluation. *Appl Surf Sci*. 2010;257(3):1119-1124. doi:10.1016/j.apsusc.2010.08.037

113. Kim B min, Feit MD, Rubenchik AM, Joslin EJ, Celliers PM, Da Silva LB. Influence of pulse duration on ultrashort laser pulse ablation of biological tissues. *J Biomed Opt*. 2001;6(3):332-338. doi:10.1117/1.1381561

114. Friedrich RE, Quade M, Jowett N, et al. Ablation precision and thermal effects of a picosecond infrared laser (PIRL) on roots of human teeth: A pilot study ex vivo. *In Vivo (Brooklyn)*. 2020;34(5):2325-2336. doi:10.21873/invivo.12045

115. Canteli D, Muñoz-García C, Morales M, et al. Thermal effects in the ablation of bovine cortical bone with pulsed laser sources. *Materials*. 2019;12(18). doi:10.3390/ma12182916

116. Gill RK, Smith ZJ, Lee C, Wachsmann-Hogiu S. The effects of laser repetition rate on femtosecond laser ablation of dry bone: A thermal and LIBS study. *J Biophotonics*. 2016;9(1-2):171-180. doi:10.1002/jbio.201500144

117. Stich T, Alagboso F, Křenek T, Kovářík T, Alt V, Docheva D. Implant-bone-interface: Reviewing the impact of titanium surface modifications on osteogenic processes in vitro and in vivo. *Bioeng Transl Med*. 2022;7:e10239. doi:10.1002/btm2.10239

118. Cunha W, Carvalho O, Henriques B, Silva FS, Özcan M, Souza JCM. Surface modification of zirconia dental implants by laser texturing. *Lasers Med Sci*. 2022;37:77-93. doi:10.1007/s10103-021-03475-y

119. Jones JR. Observing cell response to biomaterials. *Materials Today*. 2006;9(12):34-43. doi:10.1016/S1369-7021(06)71741-2

120. Shah FA, Thomsen P, Palmquist A. Osseointegration and current interpretations of the bone-implant interface. *Acta Biomater*. 2019;84:1-15. doi:10.1016/j.actbio.2018.11.018

121. Beauvais S, Drevelle O, Jann J, et al. Interactions between bone cells and biomaterials : An update. *Frontiers in Bioscience (Scholar Ed)*. 2016;8:227-263. doi:10.2741/s460

122. Calciolari E, Hamlet S, Ivanovski S, Donos N. Pro-osteogenic properties of hydrophilic and hydrophobic titanium surfaces: Crosstalk between signalling pathways in in vivo models. *J Periodontal Res*. 2018;53(4):598-609. doi:10.1111/jre.12550

123. Wang W, Caetano G, Ambler WS, et al. Enhancing the Hydrophilicity and Cell Attachment of 3D Printed PCL/Graphene Scaffolds for Bone Tissue Engineering. *Materials*. 2016;9(12):992. doi:10.3390/ma9120992

124. Deng Y, Liu X, Xu A, et al. Effect of surface roughness on osteogenesis in vitro and osseointegration in vivo of carbon fiber-reinforced polyetheretherketone–nanohydroxyapatite composite. *Int J Nanomedicine*. 2015;10(1):1425-1447. doi:10.2147/IJN.S75557

125. Simões IG, dos Reis AC, da Costa Valente ML. Analysis of the influence of surface treatment by high-power laser irradiation on the surface properties of titanium dental implants: A systematic review. *J Prosthet Dent*. Published online 2021:1-8. doi:10.1016/j.prosdent.2021.07.026

126. Han J, Zhang F, Van Meerbeek B, Vleugels J, Braem A, Castagne S. Laser surface texturing of zirconia-based ceramics for dental applications: A review. *Materials Science & Engineering C*. 2021;123:112034. doi:10.1016/j.msec.2021.112034

127. Cunha A, Oliveira V, Vilar R. *Ultrafast Laser Surface Texturing of Titanium Alloys*. Elsevier Ltd; 2016. doi:10.1016/B978-0-08-100883-6.00011-3

128. Capellato P, Riedel NA, Williams JD, Machado JPB, Popat KC, Claro APRA. Surface Modification on Ti-30Ta Alloy for Biomedical Application. *Engineering*. 2013;5(9):707-713. doi:10.4236/eng.2013.59084

129. Luo F, Wang L, Xiao Z, et al. Application of femtosecond laser microfabrication in the preparation of advanced bioactive titanium surfaces. *J Mater Chem B*. 2021;9(18):3912-3924. doi:10.1039/d1tb00231g

130. Muck M, Wolfsjäger B, Seibert K, et al. Femtosecond laser-processing of pre-anodized Ti-based bone implants for cell-repellent functionalization. *Nanomaterials*. 2021;11(5). doi:10.3390/nano11051342

131. Klos A, Sedao X, Itina TE, et al. Ultrafast Laser Processing of Nanostructured Patterns for the Control of Cell Adhesion and Migration on Titanium Alloy. *Nanomaterials*. 2020;10(5):1-18. doi:10.3390/nano10050864

132. Bush JR, Nayak BK, Nair LS, Gupta MC, Laurencin CT. Improved bio-implant using ultrafast laser induced self-assembled nanotexture in titanium. *J Biomed Mater Res B Appl Biomater*. 2011;97B(2):299-305. doi:10.1002/jbm.b.31815

133. Liu Y, Rui Z, Cheng W, et al. Characterization and evaluation of a femtosecond laser-induced osseointegration and an anti-inflammatory structure generated on a titanium alloy. *Regen Biomater*. 2021;8(2):1-14. doi:10.1093/rb/rbab006

134. Xie H, Zhang C, Wang R, et al. Femtosecond laser-induced periodic grooves and nanopore clusters make a synergistic effect on osteogenic differentiation. *Colloids Surf B Biointerfaces*. 2021;208:112021. doi:10.1016/j.colsurfb.2021.112021

135. Xie D, Xu C, Ye C, et al. Fabrication of Submicro-Nano Structures on Polyetheretherketone Surface by Femtosecond Laser for Exciting Cellular Responses of MC3T3-E1 Cells/Gingival Epithelial Cells. *Int J Nanomedicine*. 2021;16:3201-3216. doi:10.2147/IJN.S303411

136. Daskalova A, Lasgorceix M, Bliznakova I, et al. Ultra-fast laser surface texturing of β-tricalcium phosphate (β-TCP) ceramics for bone-tissue engineering applications. *J Phys Conf Ser*. 2020;1492(1):012059. doi:10.1088/1742-6596/1492/1/012059

137. Lasgorceix M, Ott C, Boilet L, et al. Micropatterning of beta tricalcium phosphate bioceramic surfaces, by femtosecond laser, for bone marrow stem cells behavior assessment. *Materials Science and Engineering C*. 2019;95(March 2018):371-380. doi:10.1016/j.msec.2018.03.004

138. Aivazi M, hossein Fathi M, Nejatidanesh F, et al. The evaluation of prepared microgroove pattern by femtosecond laser on alumina-zirconia nano-composite for endosseous dental implant application. *Lasers Med Sci*. 2016;31:1837-1843. doi:10.1007/s10103-016-2059-8

139. Sriramoju V, Alfano RR. In vivo studies of ultrafast near-infrared laser tissue bonding and wound healing. *J Biomed Opt*. 2015;20(10):108001. doi:10.1117/1.JBO.20.10.108001

140. Amini-Nik S, Kraemer D, Cowan ML, et al. Ultrafast mid-IR laser scalpel: Protein signals of the fundamental limits to minimally invasive surgery. *PLoS One*. 2010;5(9):e13053. doi:10.1371/journal.pone.0013053

141. Melvin JS, Karthikeyan T, Cope R, Fehring TK. Early Failures in Total Hip Arthroplasty — A Changing Paradigm. *J Arthroplasty*. 2014;29(6):1285-1288. doi:10.1016/j.arth.2013.12.024

142. Dobzyniak M, Fehring TK, Odum S. Early Failure in Total Hip Arthroplasty. *Clin Orthop Relat Res*. 2006;447:76-78. doi:10.1097/01.blo.0000203484.90711.52

143. Pflüger MJ, Frömel DE, Meurer A. Total Hip Arthroplasty Revision Surgery: Impact of Morbidity on Perioperative Outcomes. *J Arthroplasty*. 2021;36(2):676-681. doi:10.1016/j.arth.2020.08.005

144. Hooper J, Schwarzkopf R, Fernandez E, et al. Feasibility of single-use 3D-printed instruments for total knee arthroplasty. *Bone Joint J*. 2019;101-B(7 Supple C):115-120. doi:10.1302/0301-620X.101B7.BJJ-2018-1506.R1

145. Hasan S, van Hamersveld KT, Marang-van de Mheen PJ, Kaptein BL, Nelissen RGHH, Toksvig-Larsen S. Migration of a novel 3D-printed cementless versus a cemented total knee arthroplasty: two-year results of a randomized controlled trial using radiostereometric analysis. *Bone Joint J*. 2020;102-B(8):1016-1024. doi:10.1302/0301-620X.102B8.BJJ-2020-0054.R1

146. Mortini P, Gagliardi F, Boari N, Spina A, Bailo M, Franzin A. The Suprameatal Dural Flap for Superior Petrosal Vein Protection during the Retrosigmoid Intradural

Suprameatal Approach. *J Neurol Surg A Cent Eur Neurosurg*. 2014;75(1):53-57. doi:10.1055/s-0033-1342935

147. Neev J, Da Silva LB, Feit MD, Perry MD, Rubenchik AM, Stuart BC. Ultrashort Pulse Lasers for Hard Tissue Ablation. *IEEE Journal of Selected Topics in Quantum Electronics*. 1996;2(4):790-800. doi:10.1109/2944.577301

148. Ringer AJ, Bhamidipaty S V. Percutaneous Access to the Vertebral Bodies: A Video and Fluoroscopic Overview of Access Techniques for Trans-, Extra-, and Infrapedicular Approaches. *World Neurosurg*. 2013;80(3-4):428-435. doi:10.1016/j.wneu.2012.09.005

149. Liu X. A Novel Biportal Full Endoscopy Technique for Lumbar Lateral Recess Stenosis: Technical Report. *Clin Spine Surg*. 2018;32(2):51-56. doi:10.1097/BSD.0000000000000667

150. Kawamata T, Kamikawa S, Iseki H, Hori T. Flexible Endoscope-Assisted Endonasal Transsphenoidal Surgery for Pituitary Tumors. *Minimally Invasive Neurosurgery*. 2002;45(4):208-210. doi:10.1055/s-2002-36193

151. Welcome BM, Gilmer BB, Lang SD, Levitt M, Karch MM. Comparison of manual hand drill versus an electric dual-motor drill for bedside craniotomy. *Interdiscip Neurosurg*. 2021;23:100928. doi:10.1016/j.inat.2020.100928

152. Shin BJ, James AR, Njoku IU, Härtl R. Pedicle screw navigation: a systematic review and meta-analysis of perforation risk for computer-navigated versus freehand insertion. *Journal Neurosurgery: Spine*. 2012;17(2):113-122. doi:10.3171/2012.5.SPINE11399

153. Li Z, Yu G, Jiang S, Hu L, Li W. Robot-assisted laminectomy in spinal surgery: a systematic review. *Ann Transl Med*. 2021;9(8):1-12. doi:10.21037/atm-20-5270

154. Li CL, Fisher CJ, Komolibus K, et al. Extended-wavelength diffuse reflectance spectroscopy dataset of animal tissues for bone-related biomedical applications. *Sci Data*. 2024;11(1):136. doi:10.1038/s41597-024-02972-3

155. Shichman I, Roof M, Askew N, et al. Projections and Epidemiology of Primary Hip and Knee Arthroplasty in Medicare Patients to 2040-2060. *JB JS Open Access*. 2023;8(1):e22.00112. doi:10.2106/JBJS.OA.22.00112

156. Inacio MCS, Paxton EW, Graves SE, Namba RS, Nemes S. Projected increase in total knee arthroplasty in the United States e an alternative projection model. *Osteoarthritis Cartilage*. 2017;25(11):1797-1803. doi:10.1016/j.joca.2017.07.022

157. Heck VJ, Klug K, Prasse T, et al. Projections From Surgical Use Models in Germany Suggest a Rising Number of Spinal Fusions in Patients 75 Years and Older Will Challenge Healthcare Systems Worldwide. *Clin Orthop Relat Res*. 2023;481(8):1610-1619. doi:10.1097/CORR.0000000000002576

158. Moore ML, Singh R, Mcqueen K, et al. Workforce Trends in Spinal Surgery: Geographic Distribution and Primary Specialty Characteristics from 2012 to 2017. *World Neurosurg*. 2021;156:e392-e397. doi:10.1016/j.wneu.2021.09.073

159. Jha DK, Agrawal M, Singh Gosal J, et al. Manual Instruments as an Alternative to Drilling for Bony Exposure in Skull Base Surgery: Concept and Technique. *J Neurol Surg B Skull Base*. 2023;(EFirst). doi:10.1055/a-2031-3647

160. Hoerlesberger N, Glehr M, Amerstorfer F, Hauer G, Leithner A, Sadoghi P. Residents' Learning Curve of Total Knee Arthroplasty Based on Radiological Outcome Parameters: A Retrospective Comparative Study. *J Arthroplasty*. 2021;36(1):154-159. doi:10.1016/j.arth.2020.07.045

161. McCulloch R, Howgate D, Gibbs V, Palmer A, Taylor A, Kendrick B. Assessing the performance and learning curve of orthopaedic surgical trainees in primary total hip arthroplasty. *The Annals of The Royal College of Surgeons of England*. 2021;103(7):514-519. doi:10.1308/rcsann.2021.0016

162. Kimchi G, Orlev A, Hadanny A, Knoller N, Harel R. Minimally Invasive Spine Surgery: The Learning Curve of a Single Surgeon. *Global Spine J*. 2020;10(8):1022-1026. doi:10.1177/2192568219880872

163. Swamy A, Burström G, Spliethoff JW, et al. Diffuse reflectance spectroscopy, a potential optical sensing technology for the detection of cortical breaches during spinal screw placement. *J Biomed Opt*. 2019;24(1):017002. doi:10.1117/1.jbo.24.1.017002

164. Kosik I, Dallaire F, Pires L, Tran T, Leblond F, Wilson B. Preclinical evaluation of Raman spectroscopy for pedicular screw insertion surgical guidance in a porcine spine model. *J Biomed Opt*. 2023;28(5):057003. doi:10.1117/1.jbo.28.5.057003

165. Siasios ID, Pollina J, Khan A, Dimopoulos VG. Percutaneous screw placement in the lumbar spine with a modified guidance technique based on 3D CT navigation system. *Journal of Spine Surgery*. 2017;3(4):657-665. doi:10.21037/jss.2017.12.05

166. Slotkin EM, Patel PD, Suarez JC. Accuracy of Fluoroscopic Guided Acetabular Component Positioning During Direct Anterior Total Hip Arthroplasty. *J Arthroplasty*. 2015;30(9, Suppl. 1):102-106. doi:10.1016/j.arth.2015.03.046

167. Yoshiura T, Wada K, Kumagai K, et al. Surgical Rescue Technique for Incomplete Burr Hole Using a Small Bone Piece and the Craniotome. *World Neurosurg*. 2019;130:106-109. doi:10.1016/j.wneu.2019.06.080

168. Deng H, Puccio DJ, Anand SK, et al. Power Drill Craniostomy for Bedside Intracranial Access in Traumatic Brain Injury Patients. *Diagnostics*. 2023;13(14):2434. doi:10.3390/diagnostics13142434

169. Welcome BM, Gilmer BB, Lang SD, Levitt M, Karch MM. Comparison of manual hand drill versus an electric dual-motor drill for bedside craniotomy. *Interdiscip Neurosurg*. 2021;23:100928. doi:10.1016/j.inat.2020.100928

170. Fan X, Zhu Q, Tu P, Joskowicz L, Chen X. A review of advances in image-guided orthopedic surgery. *Phys Med Biol*. 2023;68(2):02TR01. doi:10.1088/1361-6560/acaae9

171. Jud L, Fotouhi J, Andronic O, et al. Applicability of augmented reality in orthopedic surgery – A systematic review. *BMC Musculoskelet Disord*. 2020;21(103):1-13. doi:10.1186/s12891-020-3110-2

172. Thomas NWD, Sinclair J. Image-Guided Neurosurgery: History and Current Clinical Applications. *J Med Imaging Radiat Sci*. 2015;46(3):331-342. doi:10.1016/j.jmir.2015.06.003

173. Blitz JP. Diffuse Reflectance Spectroscopy. In: Mirabella FM, ed. *Modern Techniques in Applied Molecular Spectroscopy*. New York: Wiley; 1998:185-219.

174. de Boer LL, Bydlon TM, van Duijnhoven F, et al. Towards the use of diffuse reflectance spectroscopy for real-time in vivo detection of breast cancer during surgery. *J Transl Med*. 2018;16(367):1-14. doi:10.1186/s12967-018-1747-5

175. Keller A, Bialecki P, Wilhelm TJ, Vetter MK. Diffuse reflectance spectroscopy of human liver tumor specimens - towards a tissue differentiating optical biopsy needle using light emitting diodes. *Biomed Opt Express*. 2018;9(3):1069-1081. doi:10.1364/boe.9.001069

176. Nazarian S, Gkouzionis I, Kawka M, et al. Real-time Tracking and Classification of Tumor and Nontumor Tissue in Upper Gastrointestinal Cancers Using Diffuse Reflectance Spectroscopy for Resection Margin Assessment. *JAMA Surg*. 2022;157(11):e223899. doi:10.1001/jamasurg.2022.3899

177. Geldof F, Dashtbozorg B, Hendriks BHW, Sterenborg HJCM, Ruers TJM. Layer thickness prediction and tissue classification in two-layered tissue structures using diffuse reflectance spectroscopy. *Sci Rep*. 2022;12(1):1698. doi:10.1038/s41598-022-05751-5

178. Nguyen MH, Zhang Y, Wang F, De La Garza Evia Linan J, Markey MK, Tunnell JW. Machine learning to extract physiological parameters from multispectral diffuse reflectance spectroscopy. *J Biomed Opt*. 2021;26(5):052912. doi:10.1117/1.JBO.26.5.052912

179. Dahlstrand U, Sheikh R, Ansson CD, Memarzadeh K, Reistad N, Malmsjö M. Extended-wavelength diffuse reflectance spectroscopy with a machine-learning method for in vivo tissue classification. *PLoS One*. 2019;14(10):e0223682. doi:10.1371/journal.pone.0223682

180. Fisher C, Harty J, Yee A, et al. Perspective on the integration of optical sensing into orthopedic surgical devices. *J Biomed Opt*. 2022;27(1):010601. doi:10.1117/1.jbo.27.1.010601

181. Zagzoog N, Zadeh G, Lin V, Yang VXD. Perspective review on applications of optics in skull base surgery. *Clin Neurol Neurosurg*. 2022;212:107085. doi:10.1016/j.clineuro.2021.107085

182. Gitajn IL, Slobogean GP, Henderson ER, et al. Perspective on optical imaging for functional assessment in musculoskeletal extremity trauma surgery. 2020;25(August):1-15. doi:10.1117/1.JBO.25.8.080601

183. Li CL, Fisher CJ, Komolibus K, Grygoryev K, Burke R, Andersson-Engels S. Wavelength selection using diffuse reflectance spectra and machine learning algorithms for tissue differentiation in orthopedic surgery. In: *Biophotonics Congress: Biomedical Optics 2022 (Translational, Microscopy, OCT, OTS, BRAIN)*. ; 2022:TS4B.6. doi:10.1364/translational.2022.ts4b.6

184. Duperron M, Grygoryev K, Nunan G, et al. Diffuse reflectance spectroscopy-enhanced drill for bone boundary detection. *Biomed Opt Express*. 2019;10(2):961-977. doi:10.1364/boe.10.000961

185. Grygoryev K, Komolibus K, Gunther J, et al. Cranial perforation using an optically-enhanced surgical drill. *IEEE Trans Biomed Eng*. 2020;67(12):3474–3482. doi:10.1109/TBME.2020.2987952

186. Li CL, Fisher CJ, Komolibus K, et al. Frameworks of wavelength selection in diffuse reflectance spectroscopy for tissue differentiation in orthopedic surgery. *J Biomed Opt*. 2023;28(12):121207. doi:10.1117/1.JBO.28.12.121207

187. Li CL. Biophotonics-Tyndall/PUB-FeatureSelectionDataset: Feature Selection Dataset - v1.0.0. Zenodo. doi:0.5281/zenodo.7554778

188. Li CL, Fisher CJ, Komolibus K, et al. Extended-wavelength diffuse reflectance spectroscopy dataset of animal tissues for bone-related biomedical applications. *figshare*. Published online 2024.

189. Kaneko H, Kono S, Nojima A, Kambayashi T. Transfer learning andwavelength selection method in NIR spectroscopy to predict glucose and lactate concentrations in culturemedia using VIP-Boruta. *Analytical Science Advances*. 2021;2(9-10):470-479. doi:10.1002/ansa.202000177

190. Kalatzis D, Spyratou E, Karnachoriti M, et al. Advanced Raman Spectroscopy Based on Transfer Learning by Using a Convolutional Neural Network for Personalized Colorectal Cancer Diagnosis. *Optics*. 2023;4(2):310-320. doi:10.3390/opt4020022

191. Sarin JK, Torniainen J, Prakash M, Rieppo L, Afara IO, Töyräs J. Dataset on equine cartilage near infrared spectra, composition, and functional properties. *Sci Data*. 2019;6(1):164. doi:10.1038/s41597-019-0170-y

192. Wilson RH, Nadeau KP, Jaworski FB, Tromberg BJ, Durkin AJ. Review of short-wave infrared spectroscopy and imaging methods for biological tissue characterization. *J Biomed Opt*. 2015;20(3):030901. doi:10.1117/1.JBO.20.3.030901

193. Gunaratne R, Goncalves J, Monteath I, et al. Wavelength weightings in machine learning for ovine joint tissue differentiation using diffuse reflectance spectroscopy (DRS). *Biomed Opt Express*. 2020;11(9):5122. doi:10.1364/boe.397593

194. Bergmann F, Foschum F, Marzel L, Kienle A. Ex Vivo Determination of Broadband Absorption and Effective Scattering Coefficients of Porcine Tissue. *Photonics*. 2021;8(9):365. doi:10.3390/photonics8090365

195. Bashkatov AN, Genina EA, Tuchin V V. Optical properties of skin, subcutaneous, and muscle tissues: A review. *J Innov Opt Health Sci*. 2011;4(1):9-38. doi:10.1142/S1793545811001319

196. Aerssens J, Boonen S, Lowet G, Dequeker J. *Interspecies Differences in Bone Composition, Density, and Quality: Potential Implications for in Vivo Bone Research**. Vol 139.; 1998. https://academic.oup.com/endo/article/139/2/663/2987138

197. Shapey J, Xie Y, Nabavi E, et al. Optical properties of human brain and tumour tissue: An ex vivo study spanning the visible range to beyond the second near-infrared window. *J Biophotonics*. 2022;15(4). doi:10.1002/jbio.202100072

198. Torricelli A, Pifferi A, Taroni P, Giambattistelli E, Cubeddu R. In vivo optical characterization of human tissues from 610 to 1010 nm by time-resolved reflectance spectroscopy. *Phys Med Biol*. 2001;46(8):2227-2237. doi:10.1088/0031-9155/46/8/313

199. Lüthje FL, Skovgaard K, Jensen HE, Kruse Jensen L. Pigs are useful for the molecular study of bone inflammation and regeneration in humans. *Lab Anim*. 2018;52(6):630-640. doi:10.1177/0023677218766391

200. Li CL, Fisher CJ, Komolibus K, et al. Frameworks of wavelength selection in diffuse reflectance spectroscopy for tissue differentiation in orthopedic surgery. *J Biomed Opt*. 2023;28(12). doi:10.1117/1.JBO.28.12.121207

201. Kagan R, Peters CL, Pelt CE, Anderson MB, Gililland JM. Complications and pitfalls of direct anterior approach total hip arthroplasty. *Ann Jt*. 2018;3(5):1-7. doi:10.21037/aoj.2018.04.05

202. Heo SM, Harris I, Naylor J, Lewin AM. Complications to 6 months following total hip or knee arthroplasty: observations from an Australian clinical outcomes registry. *BMC Musculoskelet Disord*. 2020;21(602):1-11. doi:10.1186/s12891-020-03612-8

203. Schwartz AM, Farley KX, Guild GN, Bradbury TL. Projections and Epidemiology of Revision Hip and Knee Arthroplasty in the United States to 2030. *Journal of Arthroplasty*. 2020;35(6):S79-S85. doi:10.1016/j.arth.2020.02.030

204. Grygoryev K, Komolibus K, Gunther J, et al. Cranial Perforation Using an Optically-Enhanced Surgical Drill. *IEEE Trans Biomed Eng*. 2020;67(12):3474-3482. doi:10.1109/TBME.2020.2987952

205. Duperron M, Grygoryev K, Nunan G, et al. Diffuse reflectance spectroscopy-enhanced drill for bone boundary detection. *Biomed Opt Express*. 2019;10(2):961. doi:10.1364/boe.10.000961

206. Govaers K, Meermans G, Stuyck J, Deprez P, Bortier H, Roels J. Endoscopy for cement removal in revision arthroplasty of the hip. *Journal of Bone and Joint Surgery*. 2006;88-A(SUPPL. 4):101-110.

207. Slotkin EM, Patel PD, Suarez JC. Accuracy of Fluoroscopic Guided Acetabular Component Positioning During Direct Anterior Total Hip Arthroplasty. *J Arthroplasty*. 2015;30(9, Suppl. 1):102-106. doi:10.1016/j.arth.2015.03.046

208. Sdao S, Orlandi D, Aliprandi A, et al. The role of ultrasonography in the assessment of peri-prosthetic hip complications. *J Ultrasound*. 2015;18(3):245-250. doi:10.1007/s40477-014-0107-4

209. Laffosse JM. Removal of well-fixed fixed femoral stems. *Orthopaedics and Traumatology: Surgery and Research*. 2016;102(1):S177-S187. doi:10.1016/j.otsr.2015.06.029

210. Masri BA, Mitchell PA, Duncan CP. Removal of solidly fixed implants during revision hip and knee arthroplasty. *J Am Acad Orthop Surg*. 2005;13(1):18-27. doi:10.5435/00124635-200501000-00004

211. Tovar-Bazaga M, Sáez-Martínez D, Auñón Á, López-Oliva F, Pardos-Mayo B, Calvo E. Surgical Technique of a Cement-On-Cement Removal System for Hip and Knee Arthroplasty Revision Surgery. *Arthroplast Today*. 2021;9:112-117. doi:10.1016/j.artd.2021.05.008

212. Cnudde PHJ, Kärrholm J, Rolfson O, Timperley AJ, Mohaddes M. Cement-in-cement revision of the femoral stem. *Bone Joint J*. 2017;99-B(4):27-32. doi:10.1302/0301-620X.99B4.BJJ-2016-1222.R1

213. Liddle A, Webb M, Clement N, et al. Ultrasonic cement removal in cement-in-cement revision total hip arthroplasty: What is the effect on the final cement-in-cement bond? *Bone Joint Res*. 2019;8(6):246-252. doi:10.1302/2046-3758.86.BJR-2018-0313.R1

214. Vaishya R, Chauhan M, Vaish A. Bone cement. *J Clin Orthop Trauma*. 2013;4(4):157-163. doi:10.1016/j.jcot.2013.11.005

215. Engelhardt A, Kanawade R, Knipfer C, Schmid M, Stelzle F, Adler W. Comparing classification methods for diffuse reflectance spectra to improve tissue specific laser surgery. *BMC Med Res Methodol*. 2014;14(1):1-15. doi:10.1186/1471-2288-14-91

216. Fanjul-Vélez F, Pampín-Suárez S, Arce-Diego JL. Application of Classification Algorithms to Diffuse Reflectance Spectroscopy Measurements for Ex Vivo Characterization of Biological Tissues. *Entropy*. 2020;22(7):736. doi:10.3390/e22070736

217. Nguyen MH, Zhang Y, Wang F, De La Garza Evia Linan J, Markey MK, Tunnell JW. Machine learning to extract physiological parameters from multispectral diffuse reflectance spectroscopy. *J Biomed Opt*. 2021;26(5):052912. doi:10.1117/1.jbo.26.5.052912

218. Sun Y, Dumont AP, Arefin MS, Patil CA. Model-based characterization platform of fiber optic extended-wavelength diffuse reflectance spectroscopy for identification of neurovascular bundles. *J Biomed Opt*. 2022;27(9):095002. doi:10.1117/1.jbo.27.9.095002

219. Fernandes L, Carvalho S, Carneiro I, et al. Diffuse reflectance and machine learning techniques to differentiate colorectal cancer ex vivo. *Chaos*. 2021;31(5):053118. doi:10.1063/5.0052088

220. Chan JY le, Mun S, Leow H, et al. Mitigating the multicollinearity problem and its machine learning approach : A review. *Mathematics*. 2022;10(8):1283. doi:https://doi.org/10.3390/math10081283

221. Silalahi DD, Midi H, Arasan J, Mustafa MS, Caliman JP. Robust Wavelength Selection Using Filter-Wrapper Method and Input Scaling on Near Infrared Spectral Data. *Sensors*. 2020;20(17):5001. doi:10.3390/s20175001

222. Baltussen EJM, Sterenborg HJCM, Ruers TJM, Dashtbozorg B. Optimizing algorithm development for tissue classification in colorectal cancer based on diffuse reflectance spectra. *Biomed Opt Express*. 2019;10(12):6096-6113. doi:10.1364/boe.10.006096

223. Jiang H, Xu W, Chen Q. Comparison of algorithms for wavelength variables selection from near-infrared (NIR) spectra for quantitative monitoring of yeast (Saccharomyces cerevisiae) cultivations. *Spectrochim Acta A Mol Biomol Spectrosc*. 2019;214(5):366-371. doi:10.1016/j.saa.2019.02.038

224. Remeseiro B, Bolon-canedo V. A review of feature selection methods in medical applications. *Comput Biol Med*. 2019;112:103375. doi:10.1016/j.compbiomed.2019.103375

225. Jović A, Brkić K, Bogunović N. A review of feature selection methods with applications. In: *2015 38th International Convention on Information and Communication Technology, Electronics and Microelectronics (MIPRO)*. ; 2015:1200-1205. doi:10.1109/MIPRO.2015.7160458

226. Peng Y, Wu Z, Jiang J. A novel feature selection approach for biomedical data classification. *J Biomed Inform*. 2010;43(1):15-23. doi:10.1016/j.jbi.2009.07.008

227. Bolón-Canedo V, Sánchez-Maroño N, Alonso-Betanzos A. A review of feature selection methods on synthetic data. *Knowl Inf Syst*. 2013;34:483-519. doi:10.1007/s10115-012-0487-8

228. Mamouei M, Budidha K, Baishya N, Qassem M, Kyriacou P. Comparison of wavelength selection methods for in-vitro estimation of lactate: a new unconstrained, genetic algorithm-based wavelength selection. *Sci Rep*. 2020;10(1):16905. doi:10.1038/s41598-020-73406-4

229. Fayyad U, Piatetsky-Shapiro G, Smyth P. Knowledge Discovery and Data Mining: Towards a Unifying Framework. In: *KDD-96 Proceedings*. ; 1996:82-88. doi:10.1511/1999.16.807

230. Oreski D, Novosel T. Comparison of Feature Selection Techniques in Knowledge Discovery Process. *TEM Journal*. 2014;3(4):285-290.

231. Liu H, Motoda H, Setiono R, Zhao Z. Feature Selection : An Ever Evolving Frontier in Data Mining. In: *Journal of Machine Learning Research: Workshop and Conference Proceedings 10: The Fourth Workshop on Feature Selection in Data Mining*. Vol 10. ; 2010:4-13.

232. Pedregosa F, Varoquaux G, Gramfort A, et al. Scikit-learn: Machine Learning in Python. *Journal of Machine Learning Research*. 2011;12:2825-2830. doi:10.48550/arXiv.1201.0490

233. Virtanen P, Gommers R, Oliphant TE, et al. SciPy 1.0: Fundamental Algorithms for Scientific Computing in Python. *Nat Methods*. 2020;17:261-272. doi:10.1038/s41592-019-0686-2

234. Lundberg SM, Erion G, Chen H, et al. From local explanations to global understanding with explainable AI for trees. *Nat Mach Intell*. 2020;2(1):56-67. doi:10.1038/s42256-019-0138-9

235. Lundberg SM, Lee SI. A Unified Approach to Interpreting Model Predictions. In: *31st Conference on Neural Information Processing Systems (NIPS 2017)*. ; 2017:4766-4775. doi:10.48550/arXiv.1705.07874

236. Krishnan SR, Seelamantula CS. On the selection of optimum Savitzky-Golay filters. In: *IEEE Transactions on Signal Processing*. Vol 61. IEEE; 2013:380-391. doi:10.1109/TSP.2012.2225055

237. Rinnan Å, Berg F Van den, Engelsen SB. Review of the most common pre-processing techniques for near-infrared spectra. *Trends in Analytical Chemistry*. 2009;28(10):1201-1222. doi:10.1016/j.trac.2009.07.007

238. Abdi H, Williams LJ. Principal component analysis. *Wiley Interdiscip Rev Comput Stat*. 2010;2(4):433-459. doi:10.1002/wics.101

239. Tharwat A, Gaber T, Ibrahim A, Hassanien AE. Linear discriminant analysis: A detailed tutorial. *AI Communications*. 2017;30(2):169-190. doi:10.3233/AIC-170729

240. Mehmood T, Liland KH, Snipen L, Sæbø S. A review of variable selection methods in Partial Least Squares Regression. *Chemometrics and Intelligent Laboratory Systems*. 2012;118:62-69. doi:10.1016/j.chemolab.2012.07.010

241. Lee LC, Liong CY, Jemain AA. Partial least squares-discriminant analysis (PLS-DA) for classification of high-dimensional (HD) data: A review of contemporary practice strategies and knowledge gaps. *Analyst*. 2018;143(15):3526-3539. doi:10.1039/c8an00599k

242. Bolón-Canedo V, Alonso-Betanzos A. Ensembles for feature selection: A review and future trends. *Information Fusion*. 2019;52:1-12. doi:10.1016/j.inffus.2018.11.008

243. Pechenizkiy M, Tsymbal A, Puuronen S. PCA-based feature transformation for classification: issues in medical diagnostics. *Proceedings 17th IEEE Symposium on Computer-Based Medical Systems*. 2004;17:535-540. doi:10.1109/cbms.2004.1311770

244. Bertsimas D, Tsitsiklis J. Simulated Annealing. *Statistical Science*. 1993;8(1):10-15. doi:10.1214/ss/1177011077

245. Leardl R, Norgaard L. Sequential application of backward interval partial least squares and genetic algorithms for the selection of relevant spectral regions. *J Chemom*. 2004;18(11):486-497. doi:10.1002/cem.893

246. Chong IG, Jun CH. Performance of some variable selection methods when multicollinearity is present. *Chemometrics and Intelligent Laboratory Systems*. 2005;78(1):103-112. doi:10.1016/j.chemolab.2004.12.011

247. Ding C, Peng H. Minimum redundancy feature selection from microarray gene expression data. *J Bioinform Comput Biol*. 2005;3(2):185–205. doi:10.1109/CSB.2003.1227396

248. Vergara JR, Estévez PA. A review of feature selection methods based on mutual information. *Neural Comput Appl*. 2014;24(1):175-186. doi:10.1007/s00521-013-1368-0

249. Robnik-Šikonja M, Kononenko I. Theoretical and Empirical Analysis of ReliefF and RReliefF. *Mach Learn*. 2003;53:23-69. doi:10.1023/A:1025667309714

250. Urbanowicz RJ, Meeker M, La Cava W, Olson RS, Moore JH. Relief-based feature selection: Introduction and review. *J Biomed Inform*. 2018;85:189-203. doi:10.1016/j.jbi.2018.07.014

251. Kursa MB, Jankowski A, Rudnicki WR. Boruta - A system for feature selection. *Fundam Inform*. 2010;101(4):271-285. doi:10.3233/FI-2010-288

252. Kursa MB, Rudnicki WR. Feature selection with the boruta package. *J Stat Softw*. 2010;36(11):1-13. doi:10.18637/jss.v036.i11

253. Ribeiro MT, Singh S, Guestrin C. "Why Should I Trust You?" Explaining the Predictions of Any Classifier. In: *Proceedings of the 22nd ACM SIGKDD International*

Conference on Knowledge Discovery and Data Mining. ; 2016:97-101. doi:10.18653/v1/n16-3020

254. Štrumbelj E, Kononenko I. Explaining prediction models and individual predictions with feature contributions. *Knowl Inf Syst*. 2014;41(3):647-665. doi:10.1007/s10115-013-0679-x

255. Shrikumar A, Greenside P, Kundaje A. Learning important features through propagating activation differences. In: *34th International Conference on Machine Learning, ICML 2017*. Vol 7. ; 2017:4844-4866. doi:10.48550/arXiv.1704.02685

256. Datta A, Sen S, Zick Y. Algorithmic Transparency via Quantitative Input Influence: Theory and Experiments with Learning Systems. In: *Proceedings - 2016 IEEE Symposium on Security and Privacy, SP 2016*. IEEE; 2016:598-617. doi:10.1109/SP.2016.42

257. Bach S, Binder A, Montavon G, Klauschen F, Müller KR, Samek W. On pixel-wise explanations for non-linear classifier decisions by layer-wise relevance propagation. *PLoS One*. 2015;10(7):e0130140. doi:10.1371/journal.pone.0130140

258. Lipovetsky S, Conklin M. Analysis of regression in game theory approach. *Appl Stoch Models Bus Ind*. 2001;17(4):319-330. doi:10.1002/asmb.446

259. Lundberg SM, Lee SI. A Unified Approach to Interpreting Model Predictions. In: *31st Conference on Neural Information Processing Systems (NIPS 2017)*. ; 2017:4766-4775. doi:10.48550/arXiv.1705.07874

260. Morán-Fernández L, Bolón-Canedo V, Alonso-Betanzos A. Centralized vs. distributed feature selection methods based on data complexity measures. *Knowl Based Syst*. 2017;117:27-45. doi:10.1016/j.knosys.2016.09.022

261. Zou H, Hastie T, Tibshirani R. Sparse principal component analysis. *Journal of Computational and Graphical Statistics*. 2006;15(2):265-286. doi:10.1198/106186006X113430

262. Donovan DJ, Moquin RR, Ecklund JM. Cranial Burr Holes and Emergency Craniotomy: Review of Indications and Technique. *Mil Med*. 2006;171(1):12-19. doi:https://doi.org/10.7205/MILMED.171.1.12

263. Chughtai KA, Nemer OP, Kessler AT, Bhatt AA. Post-operative complications of craniotomy and craniectomy. *Emerg Radiol*. 2019;26(1):99-107. doi:10.1007/s10140-018-1647-2

264. Gopalakrishnan MS, Shanbhag NC, Shukla DP, Konar SK, Bhat DI, Devi BI. Complications of decompressive craniectomy. *Front Neurol*. 2018;9(NOV). doi:10.3389/fneur.2018.00977

265. Caird JD, Choudhari KA. "Plunging" during burr hole craniostomy: A persistent problem amongst neurosurgeons in Britain and Ireland. *Br J Neurosurg*. 2003;17(6):509-512. doi:10.1080/02688690310001627722

266. Vogel TW, Dlouhy BJ, Howard MA. Don't take the plunge: Avoiding adverse events with cranial perforators: Clinical article. *J Neurosurg*. 2011;115(3):570-575. doi:10.3171/2011.3.JNS101310

267. Beniwal M, Shukla D. Management of perforator plunge in the transverse sinus. *Pediatr Neurosurg*. 2016;51(5):273-275. doi:10.1159/000445901

268. Grygoryev K, Komolibus K, Gunther J, et al. Cranial Perforation Using an Optically-Enhanced Surgical Drill. *IEEE Trans Biomed Eng*. 2020;67(12):3474-3482. doi:10.1109/TBME.2020.2987952

269. Li K, Wu Q, Feng S, et al. In situ detection of human glioma based on tissue optical properties using diffuse reflectance spectroscopy. *J Biophotonics*. 2023;16(11). doi:10.1002/jbio.202300195

270. Zhang Y, Moy AJ, Feng X, et al. Diffuse reflectance spectroscopy as a potential method for nonmelanoma skin cancer margin assessment. *Transl Biophotonics*. 2020;2(3). doi:10.1002/tbio.202000001

271. Fredriksson I, Larsson M, Strömberg T. Inverse Monte Carlo method in a multilayered tissue model for diffuse reflectance spectroscopy. *J Biomed Opt*. 2012;17(4):047004. doi:10.1117/1.jbo.17.4.047004

272. Rudraiah PS, Duadi H, Fixler D. Bottom layer absorption coefficients extraction from two-layer phantoms based on crossover point in diffuse reflectance. *J Biomed Opt*. 2021;26(11):117001. doi:10.1117/1.jbo.26.11.117001

273. Geldof F, Dashtbozorg B, Hendriks BHW, Sterenborg HJCM, Ruers TJM. Layer thickness prediction and tissue classification in two-layered tissue structures using diffuse reflectance spectroscopy. *Sci Rep*. 2022;12(1):1698. doi:10.1038/s41598-022-05751-5

274. Fang Q, Boas DA. Monte Carlo Simulation of Photon Migration in 3D Turbid Media Accelerated by Graphics Processing Units. *Opt Express*. 2009;17(22):20178. doi:10.1364/OE.17.020178

275. Kao TC, Sung KB. Quantifying tissue optical properties of human heads in vivo using continuous-wave near-infrared spectroscopy and subject-specific three-dimensional Monte Carlo models. *J Biomed Opt*. 2022;27(08). doi:10.1117/1.JBO.27.8.083021

276. Fang Q. Mesh-based Monte Carlo method using fast ray-tracing in Plücker coordinates. *Biomed Opt Express*. 2010;1(1):165. doi:10.1364/BOE.1.000165

277. Okada E, Firbank M, Schweiger M, Arridge SR, Cope M, Delpy DT. Theoretical and experimental investigation of near-infrared light propagation in a model of the adult head. *Appl Opt*. 1997;36(1):21. doi:10.1364/ao.36.000021

278. Strangman GE, Li Z, Zhang Q. Depth Sensitivity and Source-Detector Separations for Near Infrared Spectroscopy Based on the Colin27 Brain Template. *PLoS One*. 2013;8(8). doi:10.1371/journal.pone.0066319

279. Custo A, Wells III WM, Barnett AH, Hillman EMC, Boas DA. Effective scattering coefficient of the cerebral spinal fluid in adult head models for diffuse optical imaging. *Appl Opt*. 2006;45(19):4747. doi:10.1364/AO.45.004747

280. Menardi G, Torelli N. Training and assessing classification rules with imbalanced data. *Data Min Knowl Discov*. 2014;28(1):92-122. doi:10.1007/s10618-012-0295-5

281. Chawla N V, Bowyer KW, Hall LO, Kegelmeyer WP. SMOTE: Synthetic Minority Over-sampling Technique. *Journal of Artificial Intelligence Research*. 2002;16:321-357. doi:https://doi.org/10.48550/arXiv.1106.1813

282. Bosschaart N, Edelman GJ, Aalders MCG, Van Leeuwen TG, Faber DJ. A literature review and novel theoretical approach on the optical properties of whole blood. *Lasers Med Sci*. 2014;29(2):453-479. doi:10.1007/s10103-013-1446-7

283. Laffosse JM. Removal of well-fixed fixed femoral stems. *Orthopaedics and Traumatology: Surgery and Research*. 2016;102(1):S177-S187. doi:10.1016/j.otsr.2015.06.029

284. Masri BA, Mitchell PA, Duncan CP. Removal of solidly fixed implants during revision hip and knee arthroplasty. *J Am Acad Orthop Surg*. 2005;13(1):18-27. doi:10.5435/00124635-200501000-00004

285. Holt G, Hook S, Hubble M. Revision total hip arthroplasty: the femoral side using cemented implants. *Int Orthop*. 2011;35(2):267-273. doi:10.1007/s00264-010-1167-5

286. Köster G, Willert HG, Buchhorn GH. Endoscopy of the femoral canal in revision arthroplasty of the hip. A new method for improving the operative technique and analysis of implant failure. *Arch Orthop Trauma Surg*. 1999;119(5-6):245-252. doi:10.1007/s004020050403

287. Govaers K, Meermans G, Stuyck J, Deprez P, Bortier H, Roels J. Endoscopy for cement removal in revision arthroplasty of the hip. *Journal of Bone and Joint Surgery*. 2006;88-A(SUPPL. 4):101-110. doi:10.2106/JBJS.F.00699

288. Petersen H, Gliese A, Stober Y, et al. Picosecond Infrared Laser (PIRL) Application in Stapes Surgery—First Experience in Human Temporal Bones. *Otology and Neurotology*. 2018;39(4):e224-e230. doi:10.1097/MAO.0000000000001753

289. Woolman M, Gribble A, Bluemke E, et al. Optimized Mass Spectrometry Analysis Workflow with Polarimetric Guidance for ex vivo and in situ Sampling of Biological Tissues. *Sci Rep*. 2017;7(1):1-12. doi:10.1038/s41598-017-00272-y

290. Woolman M, Ferry I, Kuzan-Fischer CM, et al. Rapid determination of medulloblastoma subgroup affiliation with mass spectrometry using a handheld picosecond infrared laser desorption probe. *Chem Sci*. 2017;8(9):6508-6519. doi:10.1039/c7sc01974b

291. Woolman M, Kuzan-Fischer CM, Ferry I, et al. Picosecond Infrared Laser Desorption Mass Spectrometry Identifies Medulloblastoma Subgroups on Intrasurgical Timescales. *Cancer Res*. 2019;79(9):2426-2434. doi:10.1158/0008-5472.CAN-18-3411

292. Katz L, Kiyota T, Woolman M, et al. Metabolic Lipids in Melanoma Enable Rapid Determination of Actionable BRAF-V600E Mutation with Picosecond Infrared Laser Mass Spectrometry in 10 s. *Anal Chem*. Published online September 26, 2023. doi:10.1021/acs.analchem.3c02901

293. Woolman M, Kiyota T, Belgadi SA, et al. Lipidomic-Based Approach to 10 s Classification of Major Pediatric Brain Cancer Types with Picosecond Infrared Laser Mass Spectrometry. *Anal Chem*. 2024;96(3):1019-1028. doi:10.1021/acs.analchem.3c03156

294. Leeson AM, Alexander MR, Short RD, Briggs D, Hearn MJ. Secondary ion mass spectrometry of polymers: A ToF SIMS study of monodispersed PMMA standards. *Surface and Interface Analysis*. 1997;25(4):261-274. doi:10.1002/(SICI)1096-9918(199704)25:4<261::AID-SIA233>3.0.CO;2-K

295. Henss A, Rohnke M, Khassawna T El, et al. Applicability of ToF-SIMS for monitoring compositional changes in bone in a long-term animal model. *J R Soc Interface*. 2013;10(86). doi:10.1098/rsif.2013.0332

296. Malmberg P, Nygren H. Methods for the analysis of the composition of bone tissue, with a focus on imaging mass spectrometry (TOF-SIMS). *Proteomics*. 2008;8(18):3755-3762. doi:10.1002/pmic.200800198

297. van Huizen NA, Ijzermans JNM, Burgers PC, Luider TM. Collagen analysis with mass spectrometry. *Mass Spectrom Rev*. 2020;39(4):309-335. doi:10.1002/mas.21600

298. Tahallah N, Brunelle A, De La Porte S, Laprévote O. Lipid mapping in human dystrophic muscle by cluster-time-of-flight secondary ion mass spectrometry imaging. *J Lipid Res*. 2008;49(2):438-454. doi:10.1194/jlr.M700421-JLR200

299. Nauta SP, Poeze M, Heeren RMA, Porta Siegel T. Clinical use of mass spectrometry (imaging) for hard tissue analysis in abnormal fracture healing. *Clinical Chemistry and Laboratory Medicine (CCLM)*. 2020;58(6):897-913. doi:10.1515/cclm-2019-0857

300. Meyer JHF, Land R. Threshold Concepts and Troublesome Knowledge: linkages to ways of thinking and practising within the disciplines. *Occasional Report 4, ETL Project, Edinburgh*. Published online 2003:1-16. doi:10.1109/ICACCS.2013.6938754

301. Perkins D. Constructivism and troublesome knowledge. In: Meyer JHF, Land R, eds. *Overcoming Barriers to Student Understanding: Threshold Concepts and Troublesome Knowledge*. Routledge - Taylor & Francis Group; 2006:33-47. doi:10.4324/9780203966273

302. Sandrone S, Alavian KN. Threshold Concepts in Neuroscience: Identification Challenges, Educational Opportunities and Recommendations for Practice. *Front Educ (Lausanne)*. 2021;5(March):1-7. doi:10.3389/feduc.2020.540307